UNIVERSITY OF OKLAHOMA

GRADUATE COLLEGE

CORROSION BEHAVIOR OF TUBULARS IN SOUR GAS ENVIRONMENT

A DISSERTATION

SUBMITTED TO THE GRADUATE FACULTY

in partial fulfillment of the requirements for the

Degree of

DOCTOR OF PHILOSOPHY

By

RIDA M ELGADDAFI
Norman, Oklahoma
2017

CORROSION BEHAVIOR OF TUBULARS IN SOUR GAS ENVIRONMENT

A DISSERTATION APPROVED FOR THE
MEWBOURNE SCHOOL OF PETROLEUM AND GEOLOGICAL ENGINEERING

BY

_____
Dr. Ramadan Ahmed, Chair

_____
Dr. Subhash Shah

_____
Dr. Bor-Jier (Ben) Shiau

_____
Dr. Catalin Teodoriu

_____
Dr. Harold L. Stalford

ACKNOWLEDGEMENTS

I would first like to convey my unlimited gratitude to my advisor, Dr. Ramadan Ahmed, for his guidance and support throughout my research work. I would like to thank him for providing me a great opportunity to earn my PhD. I appreciate the way he encouraged me to keep working and thinking whenever I got frustrated. I also would like to thank Dr. Subhash N. Shah, Dr. Bor-Jier (Ben) Shiau, CatalinTeodoriu and Dr. Harold L. Stalford for their guidance and willingness to serve on my thesis committee. I also would like to thank Samuel Osisanya for his guidance.

Furthermore, I would like to thank Mr. Jeff McCaskill and Mr. Joe Flenniken for providing technical support during the experimental investigation.

I dedicate this work to my parents, my wife “Manal Egsouda” and all my family for their guidance and support. Thank you and God bless you all.

I also want to thank my aunt and her family for their care and support. Many thanks to all the professors and the staff of the Mewbourne School of Petroleum and Geological Engineering. I have appreciated every moment I have spent at the school. Thanks to God for blessing this work.

TABLE OF CONTENTS

LIST OF TABLES

LIST OF FIGURES

ABSTRACT

The existence of corrosive gases (CO_2 and H_2S) in oil wells under High-Pressure High-Temperature (HPHT) condition exacerbates the severity of tubular corrosion and increases the need for different corrosion mitigation methods. To avoid unnecessary cost of replacement or failure in these conditions, highly reliable materials and corrosion control strategies must be developed. Corrosion attacks components of a well from drilling to abandonment stage.

The principal aim of this study is to understand electrochemical and physical mechanisms associated with CO_2 and H_2S corrosion of carbon steel at HPHT condition. The research approach includes experimental, theoretical and modeling studies.

Based on the theoretical studies, different corrosion models are developed to predict corrosion of carbon steel in brine saturated with mixed gas containing CO_2 with or without H_2S. The models are developed considering different phenomena involved in the corrosion process such as dissolution of gases, homogenous chemical reactions, mass transfer process, and electrochemical reactions. The models accounts for the effects of environmental variables such as presence of H_2S, pressure, temperature; flow velocity, and material type. They use an improved solubility model to predict concentration of dissolved CO_2 and other species in brine solution. Extensive experimental study has been conducted to validate the models and better understand corrosion behavior of carbon steel. Two sets of experiments were conducted during the investigation: i) low-pressure tests; and ii) high-pressure corrosion experiments. Model

predictions show good agreement with experimental measurements indicating the validity of the assumptions made in the formulation of the models.

To carry out low-pressure tests, cylindrical specimens of common carbon steel (C1045) were prepared. The specimens were exposed to brine solution saturated with mixed gas containing carbon dioxide and nitrogen. Experiments were carried out in a 2-liter autoclave at 0.83 MPa varying temperature (26 – 80°C), salt concentration (1 and 2% NaCl), and CO_2 partial pressure ratio (0 – 100%). Two different corrosion-measuring methods were employed: weight loss method and Linear Polarization Resistance (LPR) technique, which is used to measure instantaneous corrosion rate. In the presence of CO_2, LPR measurements show sharp increase in the corrosion rate for the first ten hours, reaching maximum and then sharp decrease. Moreover, results reveal that temperature is the most influential factor affecting CO_2 corrosion. The maximum corrosion rate was observed at 43°C regardless of CO_2 concentration.

The high-pressure tests were aimed at investigating corrosion resistance of API carbon steels (T95, C110 and Q125) in sweet and sour environments. Specimens were cut from API casings and machined to serve as corrosion coupons and tensile strength test specimens. Water-jet cutting and milling machines were employed to manufacture the specimens with high precision and eliminate the occurrence of material defects during manufacturing. Corrosion tests were carried out by placing 2 or 3 specimens into a 2-liter autoclave, which was filled with 950 ml of 2% NaCl solution and 1050 ml mixed gas containing CO_2, H_2S and CH_4. Sodium chloride concentration is kept as high as 2%, which stays within the range of seawater salinity and simulating formation water in the oil field (Liu et al. 2014; Hassani et al. 2011). The CO_2 and CH_4 concentrations

were varied from 0 to 100%, while H_2S concentration was varied from 0 to 150 ppm. In pure CO_2 corrosion experiments, carbon dioxide displays supercritical behavior. The total pressure and test temperature were in the range of 20.68 – 62.05 MPa and 38 – 107°C, respectively. The maximum test temperature was limited to 107°C, because the corrosion rate was very low at high temperature and it was difficult to measured accurately due to limited change in specimen weight throughout the test duration (7 days).Corrosion resistance of T95 and Q125 API carbon steels was investigated under static and dynamic condition. Dynamic tests were conducted by creating a Couette flow between two concentric cylinders (outer stationary and inner rotating at a constant speed). Tests were performed varying rotational speed from 0 to1000 rpm. All experiments were carried out for one-week duration. Due to lack of electrodes that are certified for HPHT environment, weight loss method was the only technique viable to measure corrosion rate. After exposure, the specimen surface was examined using a digital microscope to inspect corrosion product and detect presence of localized corrosion. After scale examination and weight loss measurements, the specimen Load Carrying Capacity (LCC) was measured using tensile strength measuring apparatus. LCC measurement was obtained principally to assess localized corrosion, which degrades mechanical properties of a metal without significant weight loss. Experimental results show that temperature and flow velocity are highly influential parameters on sweet corrosion. Consistent with the corrosion rate measurements obtained from low-pressure tests, the maximum corrosion rate was observed at 38°C. Under the test conditions employed in this research, Q125 carbon steel exhibited the highest corrosion resistance. Therefore, it can be considered as the best option to serve

in aqueous CO_2-H_2S environment. C110 and Q125 specimens tested at H_2S concentration of 50 ppm showed considerable reduction in LCC indicating the occurrence of localized corrosion. Similar reduction in LCC was observed when T95 and Q125 carbon steels were exposed to brine saturated with mixed gas containing 50% CO_2 and 50% CH_4 at 71°C and high rotational speeds (greater than 300 rpm).

Chapter 1 : INTRODUCTION

1.1 Overview

Generally, corrosion is described as a destructive chemical/electrochemical attack of metal by its surrounding. Scientifically, corrosion is simultaneous transfer of mass and electric charge across a metal-solution interface. It occurs usually due to an electrochemical process between the metal surface and its surrounding environment. There are many physical phenomena by which corrosion can be classified including mechanisms of corrosion reaction and level of applied stress. Thus, often corrosion is categorized into three main types: i) general corrosion (uniform corrosion) ii) localized corrosion; and iii) stress-cracking corrosion (SCC). The localized corrosion comprises crevice corrosion and pitting. The occurrence of pitting corrosion commonly associated with fluid velocity and low temperature. In addition to the mechanisms, the surrounding composition has a prominent effect in determining corrosion categories. For instance, the existence of carbon dioxide and/or hydrogen sulfide in the environment can be another criterion for classifying the corrosion type. As a result, corrosion occurring in oil and gas field is classified as sweet corrosion (fluid system not containing H_2S) or sour corrosion (fluid system containing H_2S).

Carbon dioxide related corrosion is one of the major challenges in the industry. Vast oil and gas resources are from formations that are under HPHT corrosive condition. The failure of tubulars due to CO_2 corrosion is becoming a major issue in the application of various modern production enhancement technologies such as enhanced

oil recovery (EOR). Moreover, Carbon Capture and Storage (CCS) technology has been innovated as one of the most effective method to reduce CO_2 emission and global warming.

The internal corrosion of tubulars due to CO_2 and H_2S was initially discovered in the 1940s. For last six decades, extensive experimental and theoretical studies were carried out to understand corrosion of metallic materials in CO_2-containing environment. However, most of these studies were limited to relatively low-pressure low-temperature condition, simulating conditions that are in shallow wells and oil pipelines.

CO_2 corrosion is highly dependent on the material composition and environmental conditions. Moreover, the existence of CO_2 with other impurities such as H_2S, CO, SO_2, and O_2 in production stream results in severe corrosion of well casing and production tubing (Yevtushenko et al., 2013).

There are several physical phenomena and chemical reactions involved in CO_2 corrosion process, which determine corrosion kinetics. CO_2 corrosion process includes dissolution of acidic gases in aqueous solutions, homogenous chemical reactions, mass transport process, and electrochemical reactions occurring at the metal surface. Under favorable condition (high temperature and pH), corrosion forms a barrier (scale) between electrolyte and steel surface. The scale becomes additional factor that influences the corrosion process. The slowest step in corrosion process is the one ultimately controls the corrosion rate. The main factors such as CO_2 partial pressure, temperature, salt content, and flow velocity determine the kinetics of each step involved

in CO_2 corrosion process in which they can either accelerate or retard these steps and alter the controlling step. For instance, presence of flow velocity enhances mass transport and changes the corrosion mechanism to reaction controlled. The CO_2 corrosion mechanism at low-pressure and low-temperature condition was widely investigated for the past few years. However, limited studies have been carried out to study the CO_2 corrosion mechanism at HPHT conditions. Moreover, the presence of impurities such as hydrogen sulfide makes the corrosion mechanism more complex. CO_2-H_2S corrosion mechanism is still not fully understood.

Two different methodologies (empirical and theoretical) are often used to model corrosion process of carbon steel exposed to corrosive environment containing CO_2 or CO_2-H_2S gas. The first approach is an empirical or semi-empirical, which is mainly based on intensive data gathered from corrosion test. Empirical models are aimed at predicting corrosion rate for specific condition and their application is limited. Recently, limited theoretical (mechanistic) models have been developed to predict CO_2 corrosion process taking into consideration of corrosion mechanisms. Presence of H_2S with CO_2 complicates corrosion mechanism and makes the corrosion modeling very difficult.

Wellbore integrity issue in deep-water wells has become the most complex subject for the well completion and production designers. Poor wellbore integrity increases non-productive time and subsequently the project cost. Failure of oil and gas tubular due to CO_2 corrosion can lead ultimately to environmental calamity. According

to Simmons (2008), the total annual cost of corrosion in the oil and gas industry is estimated to be $1.372 billion.

1.2 Statement of the Problem

It is well known that corrosion attack occurs at every stage of a well, from drilling to abandonment. Corrosion can degrade drillstring, production pipelines, casing and any other down-hole equipment. Well casing is mainly installed to support the wellbore and prevent leakage of formation fluid to the environment or other formations. The main concern is uniform corrosion occurring on internal and external surfaces of well tubulars. In many oil and gas fields, hydrocarbon production is accompanied with formation water containing corrosive gases (CO_2 and H_2S).

In CO_2 sequestration and EOR techniques, carbon dioxide is injected into a well under supercritical conditions exposing the interior pipe wall to the aggressive environment. Casing degradation occurs once it is installed and exposed to formation fluid. In deep-water reservoirs, maintaining the wellbore integrity is more challenging. The tubular materials are serving not only in corrosive environment but also under HPHT condition. Casing failure can lead to pollution of groundwater resources and cause environmental hazard. Therefore, it is critical to have better understanding for sweet and sour corrosion and effectively mitigate corrosion related issues to reduce associated costs and environmental impact of oil and gas operations.

1.3 Objectives

The main objective of this study is to better understand physical and electrochemical processes involved in sour and sweet corrosion of carbon steel in HPHT environment. This study is carried out to investigate the impacts of pressure, temperature, water chemistry, CO_2 and H_2S concentration, flow status and material type on corrosion behavior of carbon steel. Hence, this study is aimed at:

- Understating corrosion mechanism of tubulars under HPHT CO_2 and CO_2-H_2S containing environment.
- Developing corrosion models to describe CO_2 and CO_2-H_2S corrosion processes.
- Experimental studying corrosion behavior of carbon steel in brine saturated with acidic gases to determine the effects of pressure, temperature and gas composition.
- Determining presence of localized and intergranular corrosion under borehole condition.

1.4 Methodology and Scope of Study

To accomplish the study objectives outlined in Section 1.3, first extensive literature survey has been conducted to understand sour and sweet corrosion mechanisms and determine factors that influence corrosion resistance of metals in harsh environment. Then, comprehensive theoretical study has been performed to develop mathematical descriptions of all the process involved in the sweet and sour corrosion and determine

the role of environmental variables on each process. Subsequently, existing corrosion models have been thoroughly investigated to identify their weakness and shortcomings. New enhanced models have been developed based on the existing ones. The models are capable of making predictions for corrosion occurring at HPHT conditions. The models utilize an improved solubility model that predicts concentrations of corrosive species and solution pH.

To formulate the corrosion models, first gas-liquid equilibria of CO_2-water system is studied. The gas phase is assumed to have CH_4 and acid gases such as H_2S and CO_2. Based on this, an improved solubility model is developed to predict concentrations of CO_2, H_2S, and CH_4 in brine (NaCl solution) for wide ranges of pressure, temperature and ionic strength. Moreover, the solubility model is used to estimate the equilibrium hydrogen ion concentration in the bulk solution and subsequently solution pH. The solubility model predictions are used as input data for the corrosion models.

Different corrosion models are developed in this study. First, electrochemical-based CO_2 corrosion model is developed to predict corrosion rate in brine saturated with mixed gas containing CO_2 but not H_2S. Afterward, the model is upgraded to account for the presence of hydrogen sulfide, which considerably influences the corrosion process. In both models, mass transport process and electrochemical reaction rate are described using the Fick's first law and the Butler–Volmer equation, respectively. To validate the models, corrosion tests were carried out using various grades of carbon

steels. Furthermore, to identify the occurrence of localized corrosion and intergranular attack, mechanical properties of test specimen were measured.

The scope of this study includes experimental investigations. Hence, corrosion experiments were conducted under low-pressure and high-pressure conditions. Two types of test setup were developed to investigate mainly uniform corrosion of carbon steels varying environmental conditions.

Weight loss and LPR methods were utilized to assess corrosion behavior of carbon steel under low-pressure condition. LPR measurements were compared with weight loss (WL) data to ensure the accuracy of the measurement. The effect of temperature, gas phase CO_2 concentration and salt content on CO_2 corrosion was assessed. The total pressure was maintained constant at 0.83 MPa.

High-pressure corrosion experiments were carried out using HPHT test facility. Weight loss technique was used to measure corrosion rate. Tests were performed to investigate the impacts of total pressure, CO_2 and H_2S concentrations, temperature, type of steel, and flow velocity on the corrosion process. Moreover, tensile strength of each specimen was measured to evaluate the impact of corrosion on mechanical properties of the materials.

Chapter 2 : LITERATURE SURVEY

2.1 Gas Solubility Studies

To develop accurate corrosion models, a reliable thermodynamic model, which predicts properties of a brine-mixed-gas system, is necessary. Solubility of acidic gases in pure water and brine is needed to estimate the amount of dissolved gas and determine concentrations of ionic species. In the past few years, solubility of gases (CO_2, H_2S, CH_4, and N_2) has been experimentally and theoretically studied considering a wide range of temperature, pressure, and ionic strength.

Several experimental studies (Takenouchi and Kennedy 1964; Todheide and Franck 1963; Pitzer et al. 1984; Winkler 1906; Selleck et al. 1952; Ben-Naim and Yaacobi 1974; Blount and Price 1982; Price 1979; O'Sullivan and Smith 1970) conducted to measure the solubility of acidic and sour gases in pure water and aqueous NaCl solutions. Tests were performed mostly using single gas-phase at low-pressure and/or low-temperature conditions. Measurements were very scattered and did not display clear trend with pressure and temperature variations. Other studies were carried out to formulate improved models. However, most of the models (Li and Ngheim 1986; Harvey and Prausnitz 1989; Zuo and Guo 1991) have uncertainty of 10 to 20% at high salt concentration and high-pressure (greater than 100 MPa). Recently, Duan and sun (2003) proposed an improved model, which predicts the amount dissolved CO_2 for wide range of temperature (up to 260°C), pressure (up to 200 MPa) and ionic strength

(up to 4 m). The uncertainty of the CO_2 solubility prediction is reduced (maximum 7% at high-pressure and high-temperature).

In addition to empirical models, mathematical and semi-empirical solubility models (Carroll and Mather 1989; Barta and Bradley1985; Suleimenov and Krupp 1994) were also developed to predict dissolved amount of H_2S in pure and salty water. These models are limited to low-pressure applications (less than 3 MPa). Recently, Duan et al. (2007) developed an accurate thermodynamic model for predicting CO_2 and H_2S solubility in brines. The model is established based on a specific particle interaction theory of liquids and a highly accurate equation of state of real gases. Predictions of the model demonstrated good agreement with available measurements for wide range of pressure (up to 20 MPa). Following a similar approach, CH_4 and N_2 thermodynamic models (Duan and Mao 2006; Sun et al. 2001) were developed to predict solubility of these gases in pure water and brine for wide range of pressure, temperature and ionic strength. Although recent models (Duan and Sun 2003; Duan et al. 2007; Duan and Mao 2006; Sun et al. 2001) provide accurate prediction for pure CO_2, H_2S, N_2 and CH_4 solubility, they don't account for water content and impurities present in real gas mixtures. These limitations make the models inadequate for oil and gas applications.

Valtz et al. (2004), Chapoy et al. (2005), Choi and Nesic (2009) proposed improved thermodynamic models for predicting mutual solubilities of pure CO_2 and CH_4 in equilibrium with pure water at vapor-liquid region. However, the effects of salt content and gas composition was not considered, which makes their application limited

in corrosion modeling. More recently, a new thermodynamic model (Zirrahi et al. 2012) has been formulated to predict mutual solubilities of CO_2, H_2S, CH_4, and their mixture in brine under subsurface disposal conditions. The model predictions showed a reasonable agreement with experimental data and predictions of existing models of pure gases.

2.2. CO_2 and CO_2-H_2S Corrosion Studies

Numerous studies (de Waard and Lotz 1993; de Waard and Milliams 1975b; de Waard et al. 1995, 1991; Dugstad et al. 1994; Jangama and Srinivasan 1997; Olsen et al. 2005; Pots et al. 2002) were carried out on CO_2 and CO_2-H_2S corrosion investigating the role of different environmental parameters and material characteristics. Other studies (Smith et al. 1993; Smith and Pacheco 2006; Woollam et al. 2011; Kvarekval et al. 2002; Kvarekval et al. 2003) investigated the contribution of protective scale on corrosion. However, mostly these studies were limited to low-pressure low-temperature applications. In general, there are two major approaches to study the corrosion behavior of carbon steel: mechanistic modeling and experimental approach.

2.2.1. Modeling Studies

I. CO_2 Corrosion

CO_2 corrosion models are often classified into three major groups: i) empirical and semi-empirical models, ii) elementary mechanistic models, and iii) comprehensive mechanistic models. A number of empirical and semi-empirical models (de Waard and Lotz 1993; de Waard and Milliams 1975b; de Waard et al. 1995, 1991; Dugstad et al.

1994; Jangama and Srinivasan 1997; Olsen et al. 2005; Pots et al. 2002) were developed in the past few decades to estimate the corrosion rate. de Waard and Milliams (1975b) developed a corrosion model assuming linear relationship between pH and corrosion current density, which occurs when charge transfer rate of anodic and cathodic currents are equalized at the equilibrium potential (i.e. corrosion potential).

$$\log i_{corr} = -\mathrm{A.pH} + \mathrm{B} \tag{2.1}$$

where A and B are constants determined from experimental measurements. After examining the values of A and B for different cases, de Waard and Milliams (1975b) proposed the direct reduction of carbonic acid as a mechanism for cathodic reaction. Based on this assumption, they were able to establish simple correlation for predicting CO_2 corrosion rate as a function of temperature and CO_2 partial pressure. This model was the first attempt in modeling CO_2 corrosion. However, the effects of solution pH, flow and slow CO_2 hydration reaction on the cathodic reaction were not considered. Later, a number of studies (de Waard and Lotz 1993; de Waard and Milliams 1975a; 1975b; de Waard et al. 1995; 1991) were conducted in effort to enhance the original model (de Waard and Milliams 1975b) by introducing additional empirical correction factors to account for the influence of pH, flow, corrosion scale, and steel microstructure on corrosion rate.

To improve accuracy of empirical and semi-empirical models, elementary mechanistic models were developed. These types of models are formulated based on simple theoretical equations, which describe physicochemical phenomena occurring

during corrosion process. However, for the sake of simplicity, the phenomena involved in CO_2 corrosion such as chemical reactions, mass transfer and charge transfer are described in simplified and decoupled form. Early elementary mechanistic models (Gray et al. 1989; 1990) considered direct reduction of carbonic acid as the main cathodic reaction mechanism. As a result, model applications are limited to pH value of 4. The model employs simplified and decoupled equations for mass transfer rate calculation, and mass transfer and CO_2 chemical reaction limitations. In addition, the mixed potential theory is applied to determine equilibrium potential (corrosion potential), and subsequently the corrosion current density and corrosion rate. It is worth mentioning that the flow-sensitivity of CO_2 corrosion is not considered in this model. In their second model (Gray et al. 1990), limitation of the model has been extended to work in more alkaline environment (pH 6-10) and higher test temperature. Moreover, new electrochemical reactions at the metal surface and bicarbonate ion reduction have been incorporated into the total cathodic and carbonic acid reduction reactions. To obtained corrosion rate value, a similar approach as in their previous model is employed. Even though solution pH between 4 and 6 and high temperature are commonly known as favorite conditions for the formation of corrosion scale, the effect of scale is not considered in the model formulation.

Few years later, slightly different CO_2 corrosion modeling approach (Dayalan 1995) presented assuming steady state condition to determine the corrosion current density. In other word, it means that electrochemical reactions are simultaneously occurring at the metal surface and the sum of all the cathodic reactions is equal to that

of the anodic iron dissolution reactions. It also implies that mass transfer rate of all species are equal to their reduction or oxidation reaction rates. In this model, the reduction of hydrogen ions, carbonic acid and bicarbonate represent the total cathodic reduction mechanism, which distinguishes this model from the previous model (Grey et al. 1990). The system of equations is implicitly solved in order to estimate surface concentration of species and ultimately corrosion rate. It should be noted that Dayalan's model does not account for the influence of temperature, fluid velocity, CO_2 hydration, as well as corrosion scale. Due to the significant influence of these environmental conditions on CO_2 corrosion process, Dayalan's model has been extended to account for $FeCO_3$ layer formation and fluid velocity (Dayalan et al. 1998).

Following similar approach, Nesic et al. (1996a) developed a productive mechanistic model. The model assumes that the cathodic reaction consists of reduction of hydrogen ion, carbonic acid and bicarbonate, and water. In addition, the model accounts for the presence of oxygen. Mass transport process of corrosive species is differently modeled by assuming independent diffusion process and using well-established correlation for mass transfer coefficient, which accounts for system hydrodynamics. Some physicochemical parameters in this model are calibrated by comparing linear sweep voltammetry and weight loss measurements. The model predicts individual theoretical polarization curve (E vs. i) for each species. By using this curve, for small over-potentials, linear polarization resistance can be also determined.

Flow regime and type (single-phase or multiphase) can have substantial effect

on CO_2 corrosion. During oil and gas production and transportation, different flow regimes can develop, which may facilitate or limit the corrosion process (Sun and Jepson 1992; Chen et al. 2000). A mechanistic model (Wang et al. 2002) has been formulated to predict CO_2 corrosion in multiphase fluid. The model is applicable for horizontal pipe flow of multiphase fluid with formation of slugs. In the model formulation, hydrogen ion reduction was considered as the most dominant cathodic reaction. The model is applicable at low solution pH.

Despite the acceptance and wide use of elementary mechanistic models in the corrosion-engineering field, these models still have fundamental weakness in their simplification of physicochemical theory of corrosion phenomena. One of these weaknesses is that the diffusion process of species is separately modeled assuming a homogenous chemical reaction and no ionic interaction between the species inside the electrolyte layer.

To overcome the shortcomings of elementary mechanistic model, a number of mathematical/mechanistic models (Turgoose et al. 1992; Pots 1995; Nesic et al. 2001; Nordsveen et al. 2003), have been developed considering conservation of mass in the diffusion layer (Nernst-Planck equation). Turgoose et al. (1992) proposed the first mathematical model adopting the general approach of the Nernst-Planck equation. The model is based on mass transfer and homogenous reaction equilibria of carbonate species in the diffusion layer. The model considers total cathodic current consists of proton and carbonic acid reduction. However, the charge transfer kinetics of electro-active species is neglected. The model predicts concentration profiles of corrosive

species in the electrolyte. In addition, the current response at mass transfer limit condition can be predicted.

A more advanced mechanistic CO_2 corrosion model is developed by Pots (1995). In this model, mass transfer process and homogenous chemical reactions are coupled and described by Nernst-Planck equation (diffusion equation). This equation accounts for the effect of flow condition wherein convective mass transfer is calculated using empirical correlation for the eddy diffusivity while the charge transfer rates are assumed to follow the Tafel equation. Pots recognized the significant impact of homogenous reaction on the current response. Based on model predictions, he concluded that eliminating the direct reduction of H_2CO_3 in the total cathodic current calculation does not have significant effect on corrosion rate prediction.

Based on theoretical analysis and laboratory investigations, recent studies (Nesic et al. 2001; Nordsveen et al. 2003) developed comprehensive mechanistic models for predicting CO_2 corrosion accounting for the formation of protective iron carbonate ($FeCO_3$) film. The positive side of these models is that they distinctly described relevant phenomena (homogenous chemical reaction, electrochemical reactions and mass transport process) involved in CO_2 corrosion process. Nernst-Planck equation is employed to describe mass transfer of species from and toward the metal surface, including diffusion through the porous corrosion scale. The transport of species is attributed to three components: diffusion, convection and migration process. The turbulent convection is described via turbulent diffusivity concept. For the electrochemical reaction, kinetics of charge transfer is described using Tafel equation.

However, the current densities of corrosive species in the Tafel equation are computed differently from the approach presented in the preceding models (Turgoose et al. 1992; Pots 1995) wherein the exchange current densities of reduction reactions are calculated as a function of surface concentration of the involved species instead of the bulk concentration. Therefore, the mass transfer limitation effect is implicitly considered via calculating the surface species used in charge transfer expression. Both models (Nesic et al. 2001; Nordsveen et al. 2003) do not account for the growth of corrosion scale ($FeCO_3$) with time and change of the scale porosity. The models specify the thickness and porosity of the layer.

II. CO_2-H_2S Corrosion Studies

Historically, Anderko and Young (1999) proposed the first comprehensive mathematical model for predicting the corrosion rate of carbon steel exposed to CO_2 coexisting with H_2S saturated brine. The model is formulated by inclusive modeling of thermodynamic properties and electrochemical reactions. First, a thermodynamic model is used to determine activities of species, which participate in the corrosion process. Then, an electrochemical model is utilized to predict the reaction rates of partial cathodic and anodic processes occurring at the steel surface. Consistent with previous CO_2 corrosion model (Nesic et al. 1996), the cathodic reaction consists of reduction of hydrogen ions (H^+), carbonic acid (H_2CO_3), and water whereas the anodic reaction is represented by oxidation of iron. The influence of H_2S content on CO_2 corrosion is modeled by adding new reduction reaction to the cathodic portion, which is identified as direct hydrogen sulfide (H_2S) reduction. The model formulation accounts

for the formation of corrosion scale, which consists of both iron carbonate ($FeCO_3$) and iron sulfide (FeS) layers. Depending on temperature and water chemistry, the formation of corrosion scale affects corrosion rate. The model predictions displayed acceptable agreement with available experimental date at relatively low pressure (0.1 MPa) and wide range of temperature (up to 60°C) and for pH ranging from 4 to 6. Later, Anderko and Young (2002) improved the original model to predict corrosion rate of alloy steel containing 13% Cr. Additionally, the improvement of the model includes method for determining the active-passive transition and the effect of solution species on the passivity. The applicability of the model has been extended for predicting CO_2 corrosion rate under harsh conditions including: CO_2 partial pressure of up to 3 MPa, temperature of up to 200°C, and H_2S concentration of up to 300 ppm.

More recently, Nesic et al. (2008) developed a mechanistic model for CO_2-H_2S corrosion in multiphase flow. The model is adopted from the previous studies (Nordsveen et al. 2003; Nesic et al. 2003; Nesic and Lee 2003), which were developed for predicting CO_2 corrosion in the presence of iron carbonate scale. The original model foundation incorporates various physical processes including kinetics of electrochemical and chemical reactions, transient transport of species through turbulent boundary and porous surface scales, kinetics of scales growth and dynamics of multiphase flow. The new model provides better predictions than original model at high and low temperature and high salinity (up to 25% wt NaCl). However, the novelty of the model (Nesic et al. 2008) is that it incorporates the effects of H_2S on carbon dioxide corrosion and kinetics of iron sulfide (mackniwate layer) growth by solid-state

reaction. The model predictions are extensively compared with reliable experimental database from the oil field and showed satisfactory agreement.

A mass transfer-based mechanistic model has been developed to predict sour uniform corrosion of steel (Sun and Nesic 2009). The model is an advanced version of earlier H_2S corrosion model (Sun and Nesic 2007), which is tuned using experimental measurements and observations that reveal formation (precipitation) of two layers of mackinawite on steel surface, which is considered in the model. Formation of mackinawite layer indicates that H_2S controls the corrosion process. Consequently, the corrosion process is considered to be under mass-transfer control rather than electrochemical or chemical kinetics control. Model predictions are validated with available corrosion measurements and they display satisfactory agreement at low CO_2 and H_2S concentrations and moderate temperature. On the other hand, iron sulfide transformation and its precipitation are not considered in the model formulation. Even though the model can be employed to predict CO_2-H_2S corrosion, it does not provide good prediction for CO_2 corrosion of carbon steel.

It is well known that organic acid and oxygen have considerable influence on sour corrosion by accelerating the iron dissolution process. Therefore, their impact on metallic degradation cannot be ignored. Nesic et al. (2009) suggested a mechanistic model for predicting CO_2-H_2S corrosion behavior of carbon steel combined with organic acid and/or O_2. The unique characteristic of this model is that, the participation of CO_2 and H_2S in the formation of corrosion scale (iron carbonates and iron sulfide layers) is considered. Additionally, two distinct approaches are adopted in modeling

total corrosion rate prediction. First, the contribution of corrosive agent (carbon dioxide and organic acid) to the total corrosion rate is separately modeled considering electrochemical process. Then, contribution of H_2S is separately modeled considering mass transfer process occurring in the mackinawite layer. The total corrosion rate is obtained by adding contributions of each individual corrosive agent. The model predictions show satisfactory agreement with experimental data obtained under different test conditions (up to temperature of 120°C; fluid velocity of up to 20 m/s; and pH range of 3 - 7). The model has been validated for total pressure of up 3 MPa.

A recent mechanistic model for sour corrosion is developed by Fardisi et al. (2012). In this study, carbon dioxide is assumed to cause corrosion but not interfere with scale formation process, which is controlled by H_2S. The scale acts as a barrier between electro-active species and metal surface. The model neglects the contribution of H_2S electrochemical reaction to the corrosion process. It includes the transient chemical reactions, transport of active species, and electrochemical reactions at the metal surface. The Tafel and diffusion equations are utilized to describe charge transfer and mass transfer rates, respectively. Due to the difficulty of modeling the effect of corrosion scale (that forms in CO_2-H_2S environments) on the corrosion process, the study proposed decoupling of the scale growth from corrosion rate modeling. The model predictions exhibited satisfactory agreement with experimental measurements obtained under different test conditions. The model limitation was not specified in their work. However, the model was validated up 3 MPa and 80°C.

The most recent study (Zheng et al. 2015) developed electrochemical-based model to predict H_2S-CO_2 corrosion. The model is an extension of the existing H_2S corrosion model (Zheng et al. 2014), which was upgraded to incorporate the influence of CO_2. Charge transfer rates, mass transfer rates and CO_2 hydration reaction rate are determined according to Nesic et al. (1996). The cathodic reaction portion of the electrochemical reaction consists of four direct reductions: i) hydrogen ions, ii) hydrogen sulfide, iii) carbonic acid, and V) water reduction. The model (Zheng et al. 2015) accounts for the effects of H_2S partial pressure, solution pH, temperature, and flow velocity. However, the impact of corrosion scale (possibly formed in CO_2-H_2S environment) is not considered. As a result, model predictions demonstrate good agreement with experimental data obtained from short time exposure and under low-temperature and low-pH conditions, which are unfavorably for the formation of corrosion scale.

2.2.2. Experimental Studies

Very influential factors that have significant role in determining CO_2 corrosion are displayed in Fig. 2.1. Each element of these factors has individual effect and they can interact each other in many ways to affect the corrosion process. The exact effects of many of these factors are still unknown.

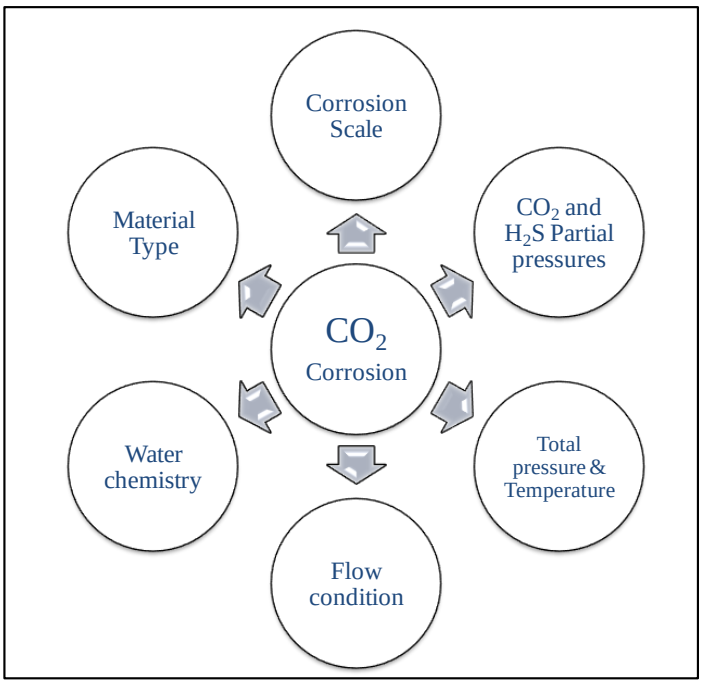

Figure 2.1 Parameters effecting CO_2 corrosion

I. Effect of CO_2 and H_2S Concentration

CO_2 partial pressure is one of the influential parameters affecting corrosion of carbon steel. In addition, the effect of CO_2 partial pressure is indirectly related to other environmental parameters such as temperature, solution pH and ionic concentration, which have substantial effect on the precipitation and formation of corrosion scale.

In scale-free conditions (low temperature and low pH), increase in CO_2 partial pressure increases corrosion rate (Wang et al. 2004; Choi et al. 2013; Nesic et al. 2003). With increased in CO_2 partial pressure, the dissolved amount of CO_2 increases and subsequently H_2CO_3 content, results in accelerated cathodic reaction and corrosion process. Generally, corrosion rate increases with CO_2 partial pressure. The relationship

can be described using a power function with exponent ranging from 0.5 to 0.8 (Dugstad et al. 1994; Videm and Dugstad 1989a). However, other conditions allow formation of protective scale (commonly at high temperature and high pH), increasing CO_2 partial pressure (P_{CO2}) may facilitate the formation of scale, which results in reduction of corrosion rate (Nesic et al. 2002; Nesic 2007; Schmitt and Hörstemeier 2006). Hence, increasing CO_2 partial pressure may also cause decline in corrosion rate (Sun and Nesic 2004; Seiersten 2001). Seiersten (2001) observed reduction in corrosion rate even in presence of porous non-protective corrosion scale. The reduction possibly occurs due to the change in water chemistry, particularly at low solution pH. Videm and Dugstad (1989b) and Moiseeva (2002) reported similar trend of corrosion rate decline with P_{CO2}. They attributed the reduction to the increase in ferrous concentration approaching super-saturation and causing retardation of the cathodic process due to the hydrogen evolution process.

Figure 2.2 displays the influence of CO_2 partial pressure on average corrosion rate of 110S steel in CO_2-H_2S containing environment (Wen-fei et al. 2012). During the corrosion tests, temperature and H_2S partial pressure were maintained at 130°C and 9 MPa, respectively. As revealed from the plot, the increase in CO_2 partial pressure from 2 to 8 MPa resulted in consistent increase in the corrosion rate. However, the corrosion rate slightly declined as the CO_2 partial pressure was elevated from 8 to 10 MPa. Bich and Goerz (1996) investigated corrosion mechanisms in sour gas gathering systems with a significant concentration of CO_2. The study has been carried out to investigate

leaks occurring in flow lines. Results reveal that CO_2 partial pressure is the main factor that determines the corrosion rate.

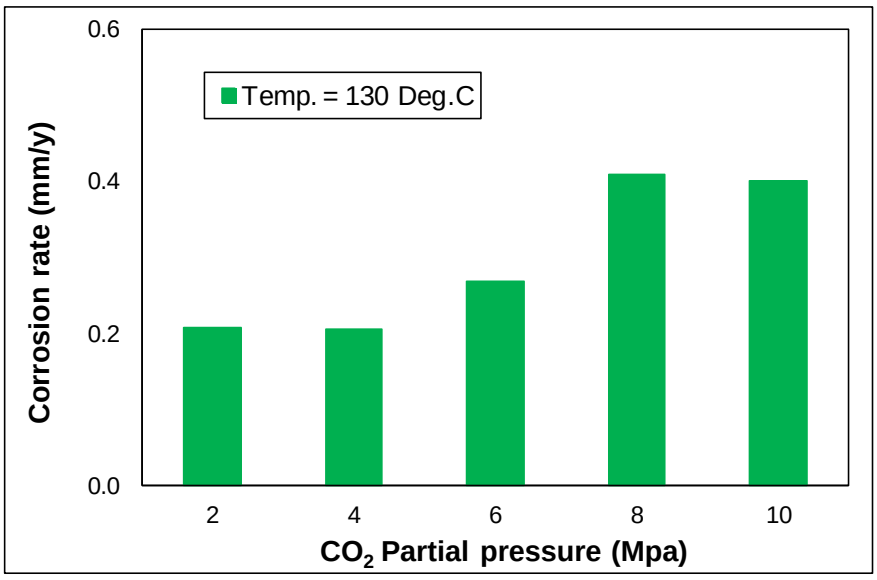

Figure 2.2 Average corrosion rate of 110S steel vs. P_{CO2} and P_{H2S}= 9 MPa (data from Wen-fei et al. 2012)

Although the effect of H_2S concentration on corrosion behavior of carbon steels has been widely studied in CO_2-H_2S environment, its role in corrosion process is still not fully understood. For instance, it has been observed (Videm et al. 1996 and Mishra et al. 1992) that, the existence of significant amount of H_2S in brine solution with or without CO_2 either accelerates or inhabits the corrosion rate of steel. Videm et al. (1996) and Mishra et al. (1992) reported two contradictory corrosion rate measurements regarding the effect of H_2S concentration. While the former reported increase in corrosion rate with addition of very small amounts (less than 30 ppm) of H_2S in CO_2-containing brine, the latter observed inhibitive effect of small amount of H_2S on CO_2 corrosion of steel.

Numerous studies (Nordsveen et al. 2003; Nesic et al. 2001; 2003; Brown and Nesic 2005; Das and Khanna 2004a; Brown et al. 2004; Sun et al. 2006; Camacho et al. 2008; Abelev et al. 2009; Solehudin et al. 2011) were carried out to study the influence of H_2S on CO_2 corrosion at low pH. There is a general agreement that presence of small amount of H_2S (~10 ppm) significantly reduces CO_2 corrosion rate. However, this trend reverses and corrosion rate increases at high H_2S concentrations (above 10 ppm). In addition, the trend of corrosion rate with H_2S concentration is related to test material and solution pH. In accordance with previous studies (retardation factor), H_2S concentration inhibited the corrosion of 1018 carbon steel at 100 ppm of hydrogen sulfide (Choi et al. 2011b). The inhibition occurred because of formation of thin corrosion scale (FeS), which partially or completely covered the steel surface and ultimately diminished anodic dissolution reaction. Generally, it has been indicated that corrosion rate at high H_2S concentration is low compared to H_2S free condition (sweet corrosion).

Consistent with previous observations, a corrosion study (Valdes and Case 1998) conducted in CO_2 and H_2S containing environment showed critical H_2S concentration that indicates the transition between the two effects of H_2S (acceleration and inhibition of CO_2 corrosion) and provides the maximum corrosion rate. In order to determine the critical value, experiments were carried out by exposing A-516 carbon steel to brine solution (5% NaCl) at different temperatures (50 to 150°C) and H_2S concentrations (0 to 40 ppm). As shown from Fig. 2.3, test results show that the maximum corrosion rate at 10 ppm of H_2S. Moreover, the critical concentration was

found to be independent of temperature, despite the reduction of the corrosion rate with temperature. It was also observed that the effect of temperature on corrosion rate was more pronounced than that of H_2S concentration.

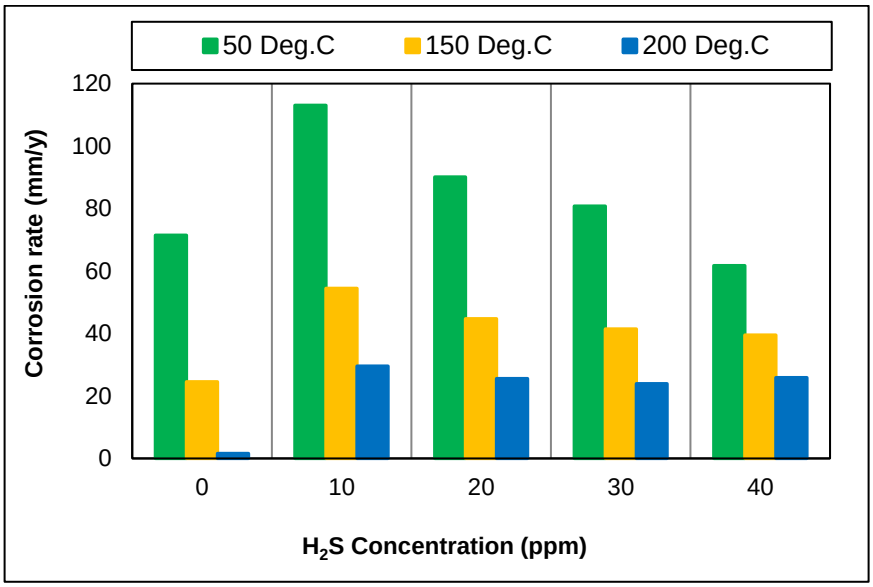

Figure 2.3 Corrosion rate of A516 steel vs. H_2S concentration at different temperatures and P_{CO2}= 3.10 MPa (data from Valdes and Case 1998)

Wen-fei et al. (2012) conducted corrosion experiments at slightly high-pressure and high-temperature to study of the influence of P_{H2S} on corrosion of carbon steel. P_{H2S} was varied from 3 to 12 MPa; whereas, P_{CO2} and temperature were kept constant at 6 MPa and 130°C, respectively. Figure 2.4 displays corrosion rate measurements as a function of P_{H2S}. Accordingly, minor reduction in corrosion rate was observed when H_2S partial pressure in the gas phase was elevated from 3 to 9 MPa. When P_{H2S} was more than 9 MPa, the corrosion rate sharply increased with P_{H2S}. As reported by Yin et al. (2008), increase in H_2S concentration resulted in both acceleration and inhibition of CO_2 corrosion.

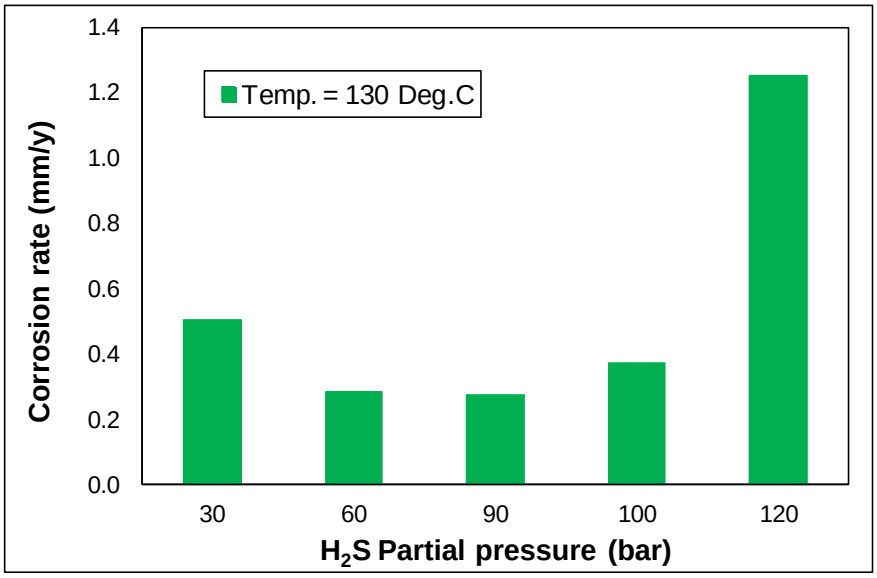

Figure 2.4 Average corrosion rate of 110S steel vs. P_{H2S} (data from Wen-fei et al. 2012)

To get a better understanding of the influence of small amount of hydrogen sulfide on CO_2 corrosion, Videm and Kvarekval (1995) conducted corrosion tests varying partial pressure of H_2S (14 to 60 Pa) and temperature (70 and 80°C) while maintaining CO_2 partial pressure at 70 kPa. In contrast with previous findings, the presence of H_2S accelerated the corrosion in the entire range of H_2S concentration. Additionally, H_2S influence on CO_2 corrosion diminished at high pH.

Partial Pressure Fraction (PPF = P_{H2S}/P_{CO2}) is considered as an adequate parameter for determining corrosion initiation condition in the presence of CO_2 and H_2S (Kermani et al. 2004). The PPF has strong influence on corrosion rate of carbon steel regardless of NaCl concentration (Agrawalet al. 2004). The PPF and other surrounding parameters are used in determining the nature and composition of corrosion scale. Jingen et al. (2011) reported corrosion rate measurements of N80 steel at temperature of

90°C and different PPF. The presence of small amount of H_2S in a CO_2 saturated brine remarkably retarded CO_2 corrosion. To determine the role of PPF on H_2S-CO_2 corrosion, Zhang et al. (2009b) carried out corrosion experiments at a constant PPF of 1.7 and various H_2S partial pressures (0.15 to 2 MPa). Corrosion rate increased with total pressure at constant temperature (60°C) and PPF. Moreover, H_2S predominantly controlled the corrosion process forming mackinawite-dominated scale.

II. Effect of Temperature

In corrosive gas containing environment, temperature is considered one of the key factors determining the corrosion phenomena. In general, temperature plays a significant role in the CO_2 corrosion process. On one hand, temperature has a substantial influence on the CO_2 thermodynamic properties, mass transport and electrochemical reactions. For instance, the dissolved amount of CO_2 in brine is much higher at low temperature and subsequently carbonic acid formation, which results in low pH and more corrosive environment. However, higher temperature can cause a decrease in CO_2 solubility and simultaneously increases reaction rates and transport of species, hence results in a higher corrosion rate. Furthermore, temperature interferes with the formation of corrosion scale. Due to the high solubility of iron carbonate at low temperature (below 60°C), non-protective layer is normally formed on the steel surface. This type of corrosion scale demonstrates porous and loose characteristics, leading to increased corrosion rates. The increased temperature accelerates the kinetics of corrosion product precipitation and forms more compact, dense corrosion scale, resulting in decrease in corrosion rate. In absence of H_2S, corrosion products mainly

consisting of iron carbonate ($FeCO_3$) precipitate and deposit on the metal surface when corrosion product concentration reaches its solubility limit. Johnson and Tomson (1991) reported that the rate of ferrous carbonate precipitation is extremely temperature sensitive. The severity of corrosion of carbon steel is more intense at low temperature regardless of hydrogen sulfide presence (Valdes and Case 1998).

A number of studies (Cui et al. 2006; Li et al. 2013a; Xiang et al. 2013; Huang et al. 2014; Yin et al. 2009; Dugstad 1995; Das 2014) to investigate the effect of temperature on CO_2 corrosion. Cui et al. (2006) conducted corrosion tests by exposing three different carbon steels (P110, N80, and J55) to brine saturated with supercritical carbon dioxide. Corrosion measurements were obtained using weight loss method at constant CO_2 partial pressure (8.274 MPa) and varying temperature (60 to 150°C). The results showed considerable decrease in corrosion rate with temperature. The decline in the corrosion rate is attributed to the formation of corrosion scale, which was mainly composed of $FeCO_3$ and $CaCO_3$. Moreover, it was found that the corrosion scale is more stable at low temperature than elevated. Li et al. (2013a) observed similar trend of CO_2 corrosion rate with temperature, although the corrosion tests were conducted at low CO_2 partial pressures (0.15 and 4 MPa).

Another study (Xiang et al. 2013) showed both exacerbation and inhibition of CO_2 corrosion of carbon steel (X70) with temperature under dynamic condition. In the study, test temperature was varied from 25 to 93°C while CO_2 partial pressure was maintained at 10 MPa. The corrosion rate was gradually increased with temperature and subsequently declined as temperature elevated above 93°C (Fig. 2.5). The

maximum corrosion rate was observed at 75°C. The first trend change in corrosion rate with temperature is attributed to increase in mass transport and electrochemical reaction rates as temperature increases. In addition, the corrosion product layer becomes more compact at higher temperature and prevents further corrosion. A recent study (Huang et al. 2014) showed reduction of CO_2 corrosion with temperature at high temperature (100 to 250°C) due to the formation of protective iron magnetite (Fe_3O_4) scale.

According to the previous studies (Yin et al. 2009; Li et al. 2013a; Dugstad 1995; Das 2014), the critical temperature in which the maximum corrosion rate is attained is not constant; it varies with other test parameters such as CO_2 concentration, pressure, salt concentration and solution pH. For instance, Yin et al. (2009) and Li et al. (2013a) reported the critical temperature around 43°C. Other studies (Ikeda et al. 1984, 1985; Dugstad 1995; Das 2014), which were conducted at low CO_2 partial pressure, observed the maximum corrosion rate between 70 and 100°C.

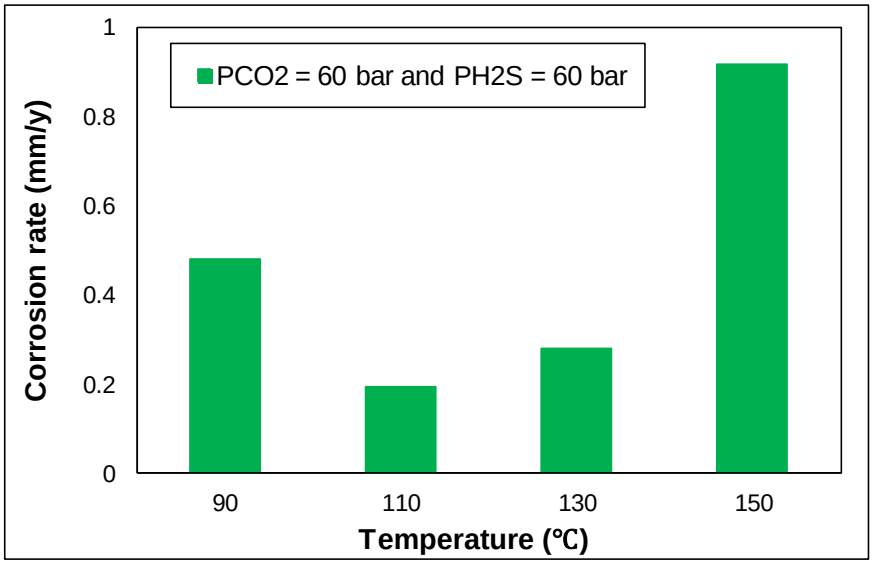

Figure 2.5 Corrosion rate of 110S steel vs. temperature, P_{CO2} = 6 MPa and P_{H2S} = 6 MPa (data from Wen-fei et al., 2012)

In CO_2-H_2S saturated environments, limited corrosion studies were performed to investigate the influence of temperature on the corrosion behavior of carbon steel. Reported corrosion rate measurements show conflicting trend with temperature. For instance, Ikeda et al. (1985) carried out corrosion test varying H_2S content and temperature (50 to 150°C). At H_2S partial pressure of 0.0103 KPa, corrosion rate increased with temperature reaching to its maximum value at 100°C and subsequently decreased. This observation has been found inconsistent with a previous study (Yin et al. 2008). In the most recent study (Wen-fei et al. 2012), at low temperature (below 110°C) corrosion rate decreased with temperature and increased above 110°C (Fig. 2.5). The minimum corrosion rate was observed at 110°C, which is slightly different from that reported by Ikeda et al. (1985).

Das and Khanna (2004b) carried out corrosion experiments to study the influence of temperature on CO_2 corrosion varying partial pressure of H_2S, pH and type of carbon steel. All tested material demonstrated similar corrosion rate trend with temperature. At low temperature, corrosion rate increased with temperature; afterward, it declined. The maximum corrosion rate was observed at 90°C regardless of other parameters. This is slightly different from the values reported by other studies (Ikeda et al. 1985; Yin et al. 2008). The increase in corrosion rate with temperature is in accordance with the measurements reported by Solehudin et al. (2011).

III. Effect of Flow Velocity

Since corrosion is defined as degradation process occurring at the metal surface, fluid velocity can either inhibit or accelerate corrosion. Fluid flow can decrease corrosion by

removing iron carbide scale that creates a galvanic effect and promotes crevice or pitting corrosion. In CO_2 containing environment, the most common effect of fluid flow is to enhance the corrosion process. In general, single-phase flow accelerates corrosion through two different mechanisms: i) enhancing mass transfer, which is more pronounced in a film-free condition, and ii) impeding the formation or removing corrosion protective scale. Chen et al. (1992) developed a trend of corrosion rate with fluid velocity (Fig. 2.6).

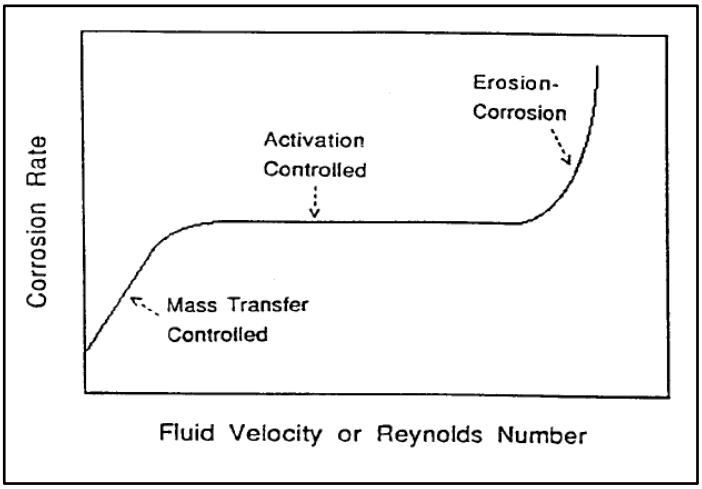

Figure 2.6 Variation of corrosion rate with flow velocity (Chen et al. 1992)

In scale unfavorable environment (low temperature and pH), the core effect of fluid velocity (turbulence) is to enhance transport of active species (cathodic species) toward the steel surface, leading to increased corrosion rate (Zhang et al. 2012). Simultaneously, the diffusion of dissolved iron (iron ions, Fe^{2+}) away from the steel surface increases with fluid velocity resulting in reduced super-saturation and precipitation rate of corrosion scale. Both effects participate in producing less protective corrosion product layer being formed at high velocities. Corrosion is

accelerated by means of flow fluid when it is mainly under mass transport control. When the charge transfer reaction becomes the rate-controlling step, increase in flow velocity has no effect on corrosion rate and it reaches steady state.

In scale-forming environment, fluid flow can affect the corrosion rate by interfering with deposition or erosion processes of the scale. First, the flow impedes the precipitation of corrosion products by enhancing the species (Fe^{2+} and CO_3^{2-}) transport away from the metal surface, leading to formation of porous and non-protective iron carbonate layer. At high velocity, the hydrodynamic wall stress plays an importance role by mechanically removing a portion of the protective scale. Partial removal of corrosion scale often leads to increased risk of localized attack. Ruzic (2005) concluded that the removal of ferrous carbonate scale in the dynamic fluid flow is attributed to coupled mechanism; chemical dissolution and mechanical removal.

Generally, two flow systems, rotating cylinder electrode and flow loop tester are utilized to study flow sensitivity of CO_2 corrosion and impact of wall shear stress on the scale formation process. Denpo and Ogawa (1993) carried out an experimental study to investigate the influence of fluid flow on corrosion resistance of N80 carbon steel and 13 Cr stainless steel in CO_2-containing environment (up to partial pressure of 4 MPa). The study was performed at 80°C by varying fluid velocity from 2 to 17 m/s during flow loop test and 0.1 to 1 m/s in a rotating electrode system. Corrosion rate of N80 carbon steel consistently increased with fluid velocity while that of 13 Cr stainless steel increased with fluid velocity and gradually stabilized at 3 m/s. In addition, no

protective corrosion scale was noted on the specimen surface under these test conditions, which possibly explains the strong velocity sensitivity of CO_2 corrosion.

Nesic et al. (1995) have carried out similar work using a flow loop. The corrosion tests were conducted under unfavorable condition for scale formation (low CO_2 partial pressure, low temperature, and pH < 4). The flow velocity in the flow loop was varied from 1 to 10 m/s. The test results showed considerable increase in corrosion rate with fluid velocity (Fig. 2.7). Predominately, the increase in corrosion rate is attributed to the enhancement of mass transport mechanisms due to turbulence and fluid movement. Moreover, in accordance with schematic of Chen et al. (1992), under these test conditions, mass transport is rate-controlling step (Fig. 2.6).

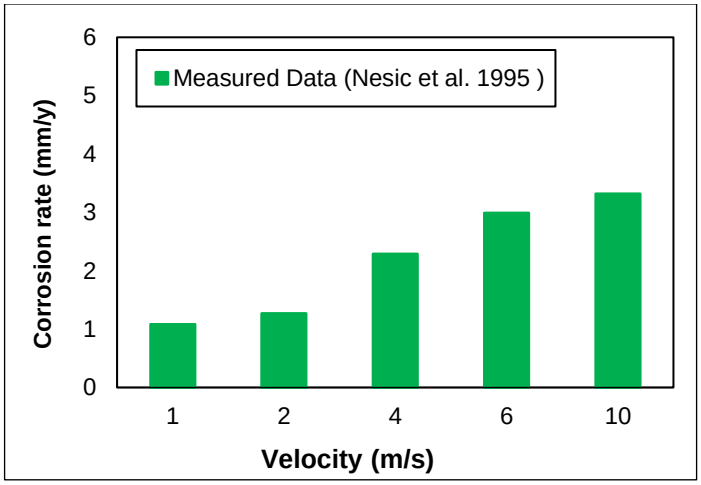

Figure 2.7 Measured corrosion rates versus fluid velocity in the absence of iron carbonate scale

The impact of fluid velocity on uniform corrosion of carbon steel is related to other environmental parameters such as CO_2 pressure, temperature, and solution pH. Dugstad et al. (1994) investigated flow sensitivity of CO_2 corrosion varying fluid velocity (0.1 to 13 m/s). Corrosion experiments were carried out varying CO_2 partial

pressure (0.05 – 2.1 MPa) and temperature (20 – 90°C). During the test, pH value was adjusted to be in the range of 4 to 6. Experimental results displayed high sensitivity of CO_2 corrosion rate to fluid flow at low pH while the rate became less sensitive at high pH. The change in corrosion rate is attributed to reduced proton concentration and dominance of carbonic acid reduction at a high pH. It is evident that corrosion mechanism at high pH was more under charge transfer control than mass transfer control. In test temperature range, the impact of flow on CO_2 corrosion was more apparent at high temperature. The change in CO_2 corrosion rate with fluid velocity under various temperatures was interrelated to formation of iron carbide scale on specimen surface (Dugstad et al. 1994). For instance, a decrease in corrosion rate was noticed at low temperature (20 – 40°C) due removal of iron carbide scale by the fluid which resulted in less galvanic effect. On the other hand, removing iron carbide due to liquid flow tends to increase the corrosion rate at higher temperature by exposing the steel surface to the corrosive environment.

CO_2 corrosion is under dynamic condition is sensitive to CO_2 partial pressure. High-pressure flow loop apparatus was used to investigate the influence of fluid flow on the corrosion rate of X-65 carbon steel (Wang et al. 2004) at various CO_2 partial pressures. The study was carried out at relatively low fluid velocity (0.2 – 2 m/s) and varying CO_2 partial pressure (0.3 to 2 MPa) at pH value of 5 and temperature of 60°C. Corrosion process was studied using electrochemical and weight loss techniques. The variation in the corrosion rate with flow velocity at three different CO_2 partial pressures is presented in Fig. 2.8.

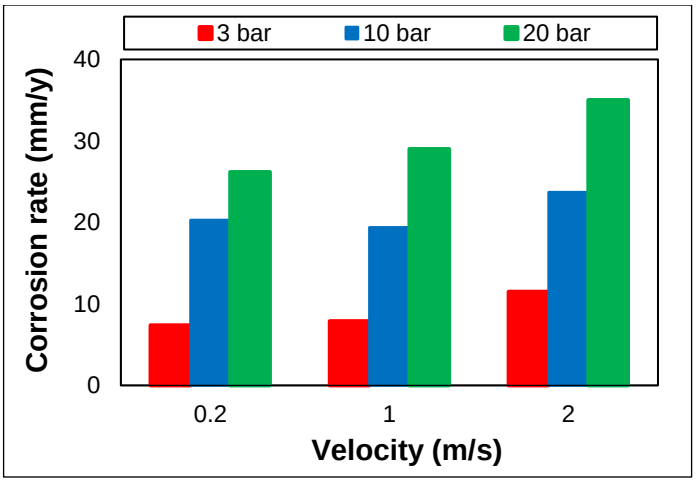

Figure 2.8 Corrosion rate vs. velocity at 60°C, pH = 5, for different P_{CO2} (data from Wang et al. 2004)

The test results displayed good agreement with previous data (Denpo and Ogawa 1993) in which the impact of velocity on corrosion rate became more pronounced with increase in CO_2 partial pressure. Greater change in corrosion rate was detected with fluid velocity at high CO_2 partial pressure (2 MPa) than at low CO_2 partial pressure. Possible explanation for this is that more protons are generated at high CO_2 partial pressure, resulting in mass transport rate-controlling regime (Nesic et al. 1996). According to their Potentio-dynamic measurements, flow velocity has minor effect on the anodic dissolution reaction. This observation indicates a charge transfer control of iron dissolution reaction.

Recently, Mohamed Nor et al. (2011b) investigated flow-sensitive of CO_2 corrosion varying CO_2 partial pressures (1-7 MPa), temperatures (25-50°C) and solution pH (3-5) using both high-pressure high-temperature rotating electrode autoclave and pipe flow loop system. Both weight loss and electrochemical techniques were used to

evaluate the effect of flow on corrosion rate and its mechanism. Flow sensitivity of CO_2 corrosion was measured using LPR technique (Fig. 2.9). Slight sensitivity of corrosion rate to rotational speed was generally observed at all test conditions. They attributed the slight sensitivity to corrosion control mechanisms. At high CO_2 partial pressure (greater than 1 MPa), the corrosion rate is more likely controlled by chemical reaction process (CO_2 hydration which is very slow process) than mass transport process of corrosive species (hydrogen and carbonic acid ions). It is evident that temperature has a substantial and dominant impact on corrosion rate. However, corrosion rate at each temperature became flow insensitive at high rotational speed (Fig. 2.9a). These results are in agreement with previous studies (Dugstad et al. 1994; Wang et al. 2004). Under all test conditions, the anodic reaction was apparently found to be less sensitive to flow conditions, indicating charge transfer control mechanism (Wang et al. 2004; Nesic et al. 1996). Iron carbide scale was detected on the steel surface under all test conditions, which probably explains the increment in the corrosion rate due to its non-protective character as well as galvanic effect.

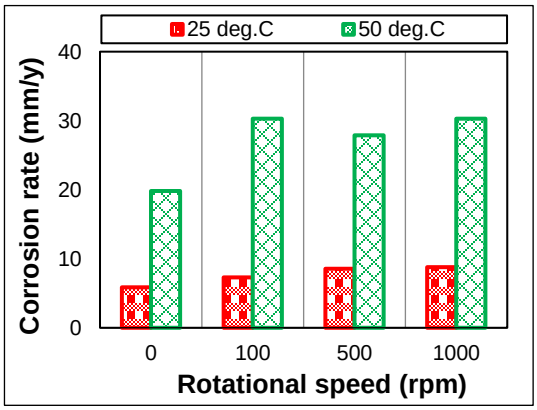

(a)

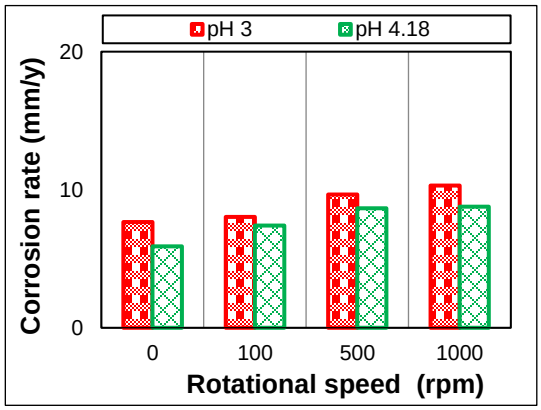

(b)

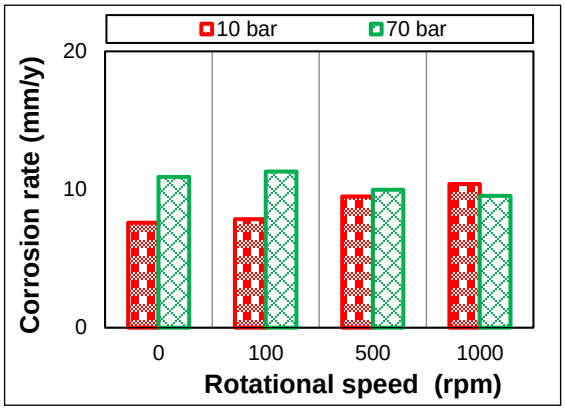

(C)

Figure 2.9 Effect of rotational speed on CO_2 corrosion at various environmental parameters: a) temperature variation; b) pH variation; and c) CO_2 partial pressure variation (Data from Mohamed Nor et al. 2011b)

To study the effect of flow velocity on CO_2-H_2S corrosion of carbon steel, Omer et al. (2005) carried out a series of flow loop experiments. Corrosion tests were performed varying pressure, temperature and velocity (1 to 5 m/s). Test outcomes revealed remarkable increase in the corrosion rate with flow velocity. Additionally, extraordinary type of corrosion (pitting corrosion) associated with uniform corrosion was observed at high flow velocity (5 m/s). The occurrence of pitting corrosion is possibly due to partial removal of corrosion scale.

Unsteady slug flow can also lead to considerable fluctuations in wall shear stress, which removes protective scale or protective inhibitor films on metal surface. As illustrated above, most of the corrosion studies assessed the flow-sensitivity of CO_2 corrosion in Couette and Poiseuille flows. In pipe flow, velocity varies from zero to its maximum value at the center; therefore, using wall shear stress is more reasonable than the velocity. Chong et al. (2014) investigated the influence of wall shear stress on CO_2-H_2S corrosion for wide range of CO_2 partial pressure (345 – 1378 KPa) and temperature

(25 – 120°C). Specimens were mounted on corrosion resistance holder and an impeller was used to agitate test solution and produce appropriate wall shear stress (1 to 27 Pa) on the specimens. The shear stress is estimated using the Wichterie's method. The results showed uniform sour corrosion of carbon steel accelerated with wall shear stress (Fig. 2.10). The wall shear stress became less effective and approximate steady corrosion rate was observed at H_2S partial pressure of 1378 KPa and 120°C (Fig. 2.10b). The increase in corrosion rate is attributed to: i) increasing wall shear stress enhances mass transfer rate of corrosive species to/away from the steel surface; and ii) higher wall shear stress could impact the integrity and protectiveness of the corrosion scale. Under similar test conditions, their findings have been consistent with results of previous studies (Omar et al. 2005; Nesic 2007; Sun et al. 2010).

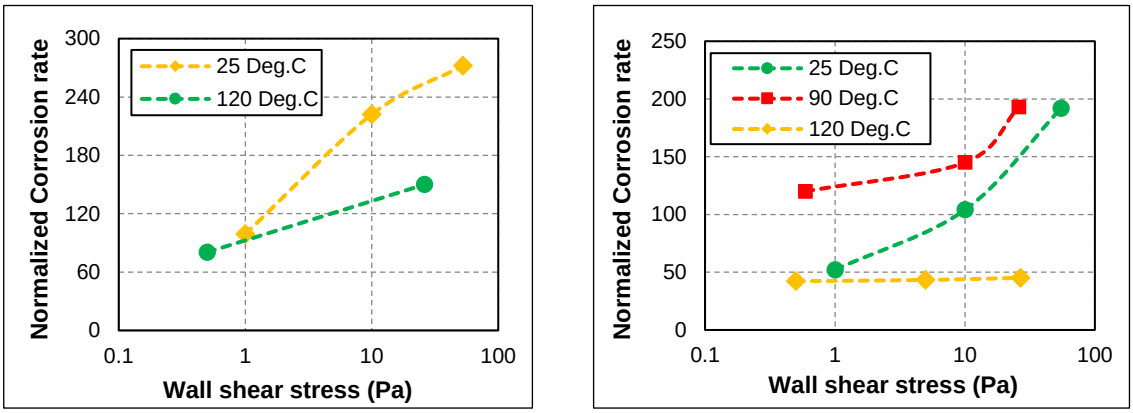

Figure 2.10 Normalized corrosion rate vs. wall shear stress at various temperatures: a) P_{H2S} = 345 KPa, and b) P_{H2S} = 1378 MPa (data from Chong et al. 2014)

IV. Effect of Salt Concentration

Salt concentration is another parameter affecting CO_2 corrosion. Formation water generally contains dissolved salts at high concentration, particularly sodium and calcium salts. Typical chloride concentration in produced brine during oil and gas production is around 50,000 mg/L (Hudak and Wachal 2001), which is highly corrosive to metals. The salt can significantly affect CO_2 corrosion process in many ways. First, high salt content reduces dissolved amount of CO_2 and homogenous chemical reaction, resulting in low carbonic acid concentration and pH. In addition, increasing salt concentration can change viscosity and density of the fluid, which consequently affects mass transport process. Fosbøl et al. (2009) discussed the effect of high ionic strength on diffusion process during CO_2 corrosion and the importance of including this effect in mechanistic models. At relative low temperature, an increase in salt concentration retards the electrochemical reaction occurring at metal surface (Fang et al. 2006). Moreover, salt interferes in the formation of iron carbonate scale, wherein high ionic strength increases the solubility limit of $FeCO_3$ and retards its precipitation and growth (Silva et al. 2002; Sun et al. 2009a). Addis et al. (2008) suggested that NaCl content could inhibit corrosion rate by forming adsorbed chloride ion film on steel surface, resulting in low corrosion rate.

Limited experimental studies have been carried out to assess the impact of salt concentration on CO_2 corrosion behavior. Some of these studies (Sun et al. 2003; Ma et al. 2003) focused on the effect of chloride ion concentration on localized corrosion. The results from both studies show acceleration of localized corrosion due to chloride.

In contrast, Jiang and Nesic (2009) found that chloride concentration between 1 to 20% by weight has no remarkable effect on localized corrosion. Their results are in agreement with observation made by Chen et al. (2002) and sun et al. (2003). Other corrosion studies (Qu, 2011; Schmitt 1984; Han et al. 2011; Nesic et al. 2008; Fang 2006; Fang et al. 2010) also showed conflicting results. For instance, Qu (2011) reported increase in corrosion rate with NaCl content while several studies (Schmitt 1984; Han et al. 2011; Nesic et al. 2008; Fang, 2006; Fang et al. 2010; Hassani et al. 2011) demonstrated a reduction in corrosion rate with salt concentration, which is attributed to the decline in corrosion rate due to effect of salt content on thermodynamic properties and influence of ionic strength on the solubility limit of $FeCO_3$.

A recent study (Liu et al. 2014) showed a different trend of corrosion rate with salt concentration. At low salt content, corrosion increased reaching its maximum value at 30 g/L of Cl^- concentration and subsequently decreased with the concentration. It is evident that CO_2 corrosion is a mixed-control process with increasing Cl^- content. Fang et al. (2006) observed gradual change in corrosion mechanism from mixed-charge transfer (limiting current) control to pure-charge transfer control with increasing salt concentration. Salt concentration shows pronounced influence not only in CO_2 saturated solution but also in CO_2-free environment.

V. Effect of Solution pH

Solution pH is classified as one of the influential factors affecting corrosion of metal in corrosive environment. It indicates the amount of H^+ ion present in the environment. Proton ion is one of the active species in cathodic reaction and highly influential in the

electrochemical process. Experimental measurements and model predictions have demonstrated critical influence of pH on formation of corrosion scale and subsequently the corrosion rate (Nesic et al. 2003). pH displays both direct and indirect effects on corrosion. pH has direct influence on corrosion because it reduces concentration of H^+. However, major influence of pH is the indirect effect, which arises from its remarkable contribution in the formation of protective scale (ferrous carbonate). Solubility of iron carbonate normally decreases at higher pH creating favorable condition for super-saturation, ultimately leading to faster precipitation, and formation of protective film, which in turn diminishes the corrosion rate.

In H_2S containing environment, pH is a key factor in determining corrosion mechanism and kinetics. For instance, at low pH (less than 2), the solubility limit of FeS is relatively high; thus, iron sulfide does not precipitate on steel surface. However, at intermediate pH values ($3 < pH < 5$), iron sulfide (FeS) becomes less soluble, resulting in the formation of protective film and reduced corrosion rate. Brown et al. (2004) carried out corrosion tests to assess the influence of solution pH on corrosion behavior of AISI 1018 steel in CO_2-H_2S containing environment. The test specimens were exposed to 1% NaCl brine solution at 60°C and 0.79 MPa. The maximum H_2S concentration was 100 ppm. Varying pH of the system from 4 to 6.6 resulted in remarkable variation in corrosion rate (Fig. 2.11).

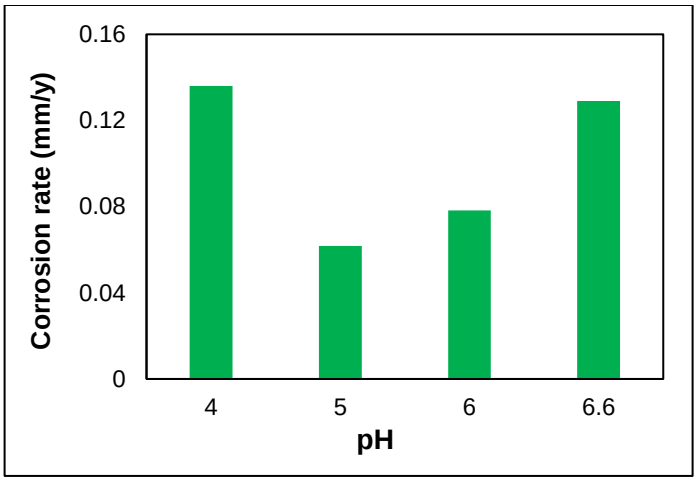

Figure 2.11 Corrosion rate vs. pH, P_{CO2} = 0.79 MPa, Vsl = 1m/s and 100 ppm H_2S in the gas phase (Data from Brown et al. 2004)

VI. Effect of Material Type

Since corrosion is generally defined as interaction between metal surface and environment, the severity of CO_2 corrosion depends on environmental conditions as well as the type of steel. The effect of material type on CO_2 corrosion arises from both chemical composition and microstructure of the metal. Often steel is categorized as mild steel or low-alloy steel when its chemical composition contains 2 to 3% of carbon by weight. Low-alloy steel or carbon steel is widely used in the oil and gas industry because it is not expensive. However, carbon steel is susceptible for corrosion. Thus, chemical composition of carbon steel is altered to enhance its corrosion resistance and mechanical properties. Alloying elements such as carbon, chromium, nickel, and copper are normally added to improve corrosion resistance. The added alloying element may potentially improve corrosion resistance; however, it can have a negative effect. For instance, carbon is added to enhance mechanical properties of steel. However, it reduces corrosion resistance of steel (Gulbrandsen E et al.1998; Al-Hassan

et al. 1998). The reason is that carbon element dissolves and reacts with iron forming iron carbide, which exhibits a galvanic effect and accelerates corrosion.

The most widely used alloying element is chromium, which typically added with different concentration to low alloy steel. The maximum concentration of Cr content in carbon steel is limited to 13% by weight. Chromium is added to low-alloy carbon steels in order to improve their sweet and sour corrosion resistance. The mechanism by which the Cr element could improve sweet corrosion resistance of carbon steel is by altering the structure and chemical composition of corrosion scale. In other word, Cr content improves the protectiveness and persistence of the corrosion scale. Several studies (Sun et al. 2016; Kermani et al. 2001; Liu et al. 2009; Hu et al. 2011; Chen et al. 2005a; Hassani et al. 2014) noted better performance of Cr-alloyed steel in CO_2 and CO_2-H_2S containing environment as compare to the regular low-alloy carbon steels. In most of these studies, the reduction in corrosion rate is attributed to the formation of two-layer corrosion scale, which is commonly consisted of $FeCO_3$ (middle layer) and mixture of $FeCO_3$, Cr $(OH)_3$ and Cr_2O_3 (inner layer). However, although Cr-alloyed steels exhibited (Yevtushenko et al. 2014; Pfennig and Kranzmann 2012) a high uniform corrosion resistance, they could not prevent occurrence of localized corrosion at elevated temperature (60°C).

In CO_2-H_2S environment, the reaction mechanism of Cr-alloyed steels is more complex and distinct from pure CO_2 environment. Limited corrosion tests (Sun et al. 2016; Liu et al. 2015; Suk Seo et al. 2015; Yin et al. 2012) were carried out to compare performance of Cr-rich and regular carbon steels in sour gas environment. Recent

studies (Liu et al. 2016 and Hassani et al. 2014) conducted at elevated pressure and temperature showed better corrosion resistance of Cr-alloyed steel in sour environment as compare to low-alloyed carbon steel. Surface analysis of the specimens indicated the formation of a dense Cr-containing corrosion scale, which blocked ion movement, resulting in lower corrosion rate. On the other hand, results reported by Sun et al. (2016) showed that 5Cr-P110 displayed the highest uniform corrosion in comparison with 3Cr-P110 and P110 steels in CO_2-H_2S environment. Other alloying element such as nickel and copper are added to improve toughness and strength of carbon steel. The addition of nickel to Cr-alloyed carbon steel has negligible effect on the corrosion process (Kimura et al. 1994).

The other characteristic of material type is the microstructure of alloyed steels, which depends on the chemical composition and heat treatment. Carbon steel has many microstructures including ferrite, pearlite, martensite, and austenite (Mohammed Nor 2013). Typical carbon steel normally exhibits ferrite-pearlitic microstructure. Similar to the chemical composition, microstructure influences sweet corrosion via forming iron carbide (Fe_3C) layer, which is electrochemically active. It accelerates corrosion by creating galvanic coupling between covered and uncovered portion of the metal. Very limited studies investigated or discussed the influence of microstructure on sweet corrosion. Rihan (2013) studied corrosion resistance of two low-carbon steels (X60 and X52) in CO_2 containing environment. The test was carried out at atmospheric pressure and 50°C. X52 demonstrated better corrosion resistance by showing lower corrosion rate in comparison with X60 carbon steel.

VII. Effect of Corrosion Product

Corrosion scale is the main factor affecting the corrosion rate. The scale functions as a diffusion barrier for the species involved in the corrosion process by covering up metal surface from further Fe^{+2} dissolution resulting in hindered corrosion, particularly as dense and less porous scale is formed. Better understanding of the kinetics of iron carbonate and iron sulfide scale formation assists in predicting and controlling CO_2-H_2S corrosion of carbon steel. The corrosion film characteristics, which are highly influenced by the surrounding conditions (CO_2 and H_2S concentrations, temperature, and solution pH and flow condition), strongly affect the corrosion process. Moreover, composition of corrosive solution is one of the factors that determine the type of corrosion scale formed on steel surface. The growth and stability of scale relies primarily on the kinetics of the corrosion process, which is affected by the environment. Generally, there are two different mechanisms (precipitation and direct reaction) by which the corrosion scale could be formed.

In H_2S corrosion process, various types of iron sulfide scales (amorphous ferrous sulfide, mackinawite, cubic ferrous sulfide, smythite, greigite, pyrrhotite, troilite, and pyrite) can form on the metal surface. Mackinawite is the most prevalent iron sulfide that forms on steel surface at low H_2S concentrations and low temperatures (Smith et al. 1993). As the H_2S concentration increases, mackinawite layer dissolves and subsequently precipitated, forming other types of iron sulfides such as pyrrohitte and pyrite. The transformation from one type to the other and its mechanism depends on the environmental conditions. In CO_2 and H_2S mixed system, corrosion scale can be

mixed, $FeCO_3$, FeS_x or occasionally Fe_3O_4 (Smith and Pacheco 2006). Smith and Pacheco (2006) proposed corrosion product formation diagram (Fig. 2.12) showing the boundary between different types of corrosion products. As displayed from the figure, two dominant operational parameters, temperature and H_2S concentration, determine type of corrosion scale. Moreover, they concluded that pyrrhotite is more thermodynamically stable than mackinawite because formation kinetics of pyrrhotite is slower than that of mackinawite.

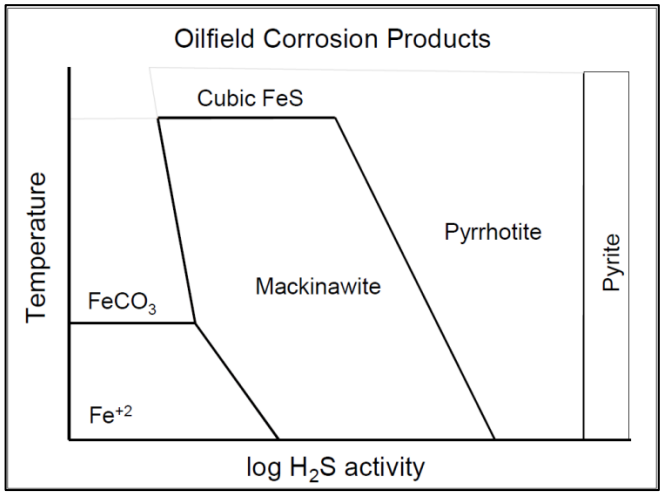

Figure 2.12 Corrosion product formation diagram (Smith and Pacheco 2006)

Smith and Wright (1994) developed a model to predict the minimum H_2S partial pressure that is necessary for mackinawite to form on steel surface in sour environment. The model requires pH and operating temperature to be identified as input data. In CO_2-H_2S environment, pressure ratio (P_{CO2}/P_{H2S}) plays an important role in determining the type of corrosion scale formed on steel surface. Dunlop et al. (1983) proposed critical value of 500 for the pressure ratio (Fig. 2.13). When pressure ratio is above 500, iron carbonates layer ($FeCO_3$) forms on steel surface and dominates the CO_2-H_2S

corrosion process. The critical pressure ratio is assumed constant and independent of temperature. However, recent study (Woollam et al. 2011) revealed that the value of the critical pressure ratio is not constant and it varies with temperature and iron ion (Fe^{2+}) concentration. This variation in critical pressure ratio results in changing the nature and composition of corrosion scale. The comparison between the two studies is presented in Fig. 2.13.

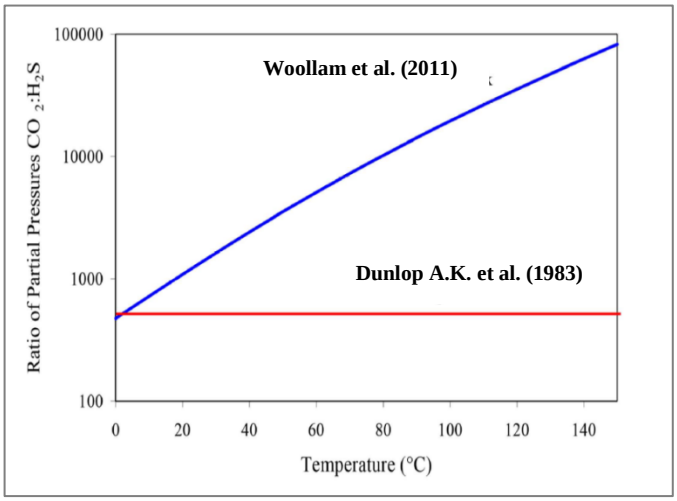

Figure 2.13 Siderite-Mackinawite boundary for varying temperatures vs. ratio of partial pressure of CO_2/H_2S

In presence of acidic gases (CO_2 and H_2S), it is relatively difficult to determine the dominant acid gas that controls corrosion process and governs the formation of corrosion scale. Masamura et al. (1987) provided the best key factor for identifying corrosion mechanism. They proposed critical pressure ratio of 200 to identify the corrosion mechanism of carbon steel in CO_2-H_2S environment. CO_2 is dominating and governing the corrosion process when P_{CO2}/P_{H2S} is above 200. However, when P_{CO2}/P_{H2S} is below 200, stability of corrosion scale (FeS and $FeCO_3$) plays major role in determining corrosion rate. The use of pressure ratio to determine the nature of

corrosion scale is supported by other investigations (Kvarekval et al. 2002; Kvarekval et al. 2003). Pots et al. (2002) utilized the pressure ratio and considered three different corrosion domains based on dominance of corrosion mechanism as affected by dominating acid gas. The corrosion types are classified (Table 2.1) and described using different regimes (Fig. 2.14).

Table 2.1 Corrosion regimes in CO_2-H_2S environment

P_{CO2}/P_{H2S}	Dominant acid gas	Type of corrosion product
Less than 20	Dominant H_2S	Any type of iron sulfide (FeS)
20< CO_2/H_2S<500	Mixed CO_2/H_2S corrosion dominance	Mixture of $FeCO_3$ and FeS
Above 500	Dominant CO_2	Iron carbonate ($FeCO_3$)

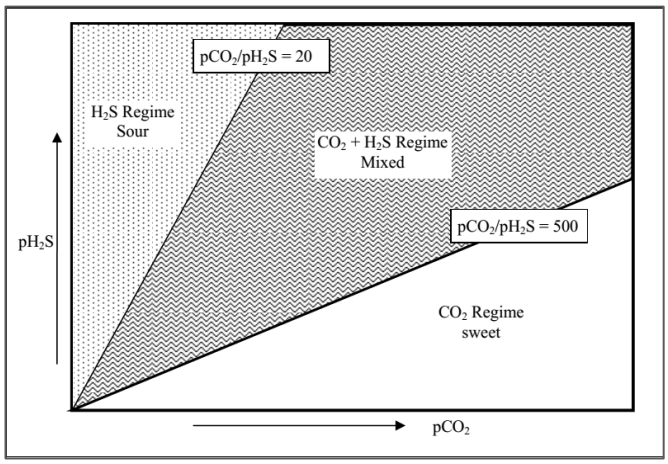

Figure 2.14 Corrosion regimes in CO_2/H_2S corrosion defined by Pots et al. (2002)

2.3 Effect of CO_2 Corrosion on Mechanical Properties

Generally, uniform corrosion has significant effect on the metallic strength. However, presence of carbon dioxide tends to accelerate corrosion and thus deteriorate the metal

through a considerable material loss or occurrence of pitting corrosion. Limited studies (Ranji and Zakeri, 2010; Chen and Garbatov Soares 2012; Chen et al. 2005b) have been conducted to investigate the effect of corrosion on mechanical properties of carbon steel and other metallic alloys under atmospheric conditions. Some of these studies (Ranji and Zakeri 2010; Garbatov et al. 2014) reported degradation of mechanical properties after exposure to corrosive environment.

Chapter 3 : THEORETICAL STUDY

3.1 CO_2 Corrosion Mechanism

Corrosion process is complex and diverse. As a result, a number of corrosion mechanisms exist to describe the process. Generally, corrosion mechanism is described as actual atomic, molecular or ionic transport process that occurs at the interface of a material and its surrounding. These processes commonly involve more than one step and the slowest step controls the rate of the overall reaction.

In corrosion process, mass transport from the interface to the environment mostly involves electrochemical, chemical, and physical processes. Since electrochemical corrosion involves the release of ions to the environment and movement of electrons within the material, this process can occur only if the environment can contain ions and the material allows flow of electrons. One of the most important processes in the electrochemical mechanism is that the atom at the steel surface dissolves into the solution as metal ion and leaves a valence electron behind, creating a negative charge on the metal surface (Fig. 3.1). Subsequently, the electron is consumed by a corrosive species in the solution. The ions of the metal move into the solution and reacts with available anions (S^- and/or CO_3^{2-}) in the solution forming corrosion scale by precipitation. Modeling CO_2 corrosion phenomena requires understanding of the mechanism of CO_2 corrosion. In this chapter, the fundamental mechanisms underlying CO_2 corrosion such as: homogenous chemical reaction in the

bulk solution, mass transport process, and electrochemical corrosion of metal and alloys are discussed.

3.1.1 Homogenous Chemical Reaction

At the gas-liquid interface of a mixture of brine and mixed gas containing CO_2, a considerable amount of carbon dioxide dissolves into brine. The carbon dioxide dissolution equation and its corresponding equilibrium constant are expressed as follows:

$$CO_{2(g)} \rightarrow CO_{2(aq)} \qquad K_{sol,CO_2} = \frac{P_{CO_2}}{C_{CO_2}} \tag{3.1}$$

where K_{sol,CO_2} is solubility constant of CO_2 which is temperature and salinity dependent, P_{CO_2} is partial pressure of CO_2, and C_{CO_2} is carbon dioxide concentration in the liquid phase. When other gases present in the gas phase, additional dissolution reaction equations are needed to describe the solubility of the gases. In this study, gas mixture of CO_2, CH_4 and H_2S is used. For the sake of simplicity, methane is considered insoluble compared to other gases. H_2S is highly soluble aqueous solution. Dissolution reaction and solubility constant equations of hydrogen sulfide are expressed as:

$$H_2S_{(g)} \rightarrow H_2S_{(aq)} \qquad K_{sol,H_2S} = \frac{P_{H_2S}}{C_{H_2S}} \tag{3.2}$$

where K_{sol,H_2S} is solubility constant of H_2S which varies with temperature and salinity. P_{H_2S} is partial pressure of H_2S and C_{H_2S} is concentration of dissolved hydrogen sulfide.

In most of previous corrosion studies, concentrations of CO_2 and H_2S in aqueous phase are obtained by applying Henry's law, which is valid for relative low pressure and low temperature. However, at pressure greater than 1 MPa, Henry's law overestimates concentrations of carbon dioxide and hydrogen sulfide. Since this work is intended to predict corrosion behavior of carbon steel at high-pressure high-temperature condition, an accurate solubility model is needed to predict accurately dissolved amount of corrosive gases under a wide range of pressure, temperature, and ionic strength. After dissolving in the liquid phase, CO_2 hydrates to form carbonic acid. Thus:

$$CO_{2(aq)} + H_2O \rightarrow H_2CO_{3(aq)} \qquad K_{hy} = \frac{C_{H_2CO_3}}{C_{CO_2}} \tag{3.3}$$

Carbonic acid (H_2CO_3) is a weak acid and it subsequently dissociates through two steps of reactions (first and second dissociation) to produce hydrogen, bicarbonate, and carbonate ions in the solution. Dissociation equations and their corresponding equilibrium constants are described as:

$$H_2CO_{3(aq)} \rightarrow H^+ + HCO_3^- \qquad K_{1,CO_2} = \frac{c_{b,HCO_3^-} \times c_{b,H^+}}{c_{b,H_2CO_3}} \tag{3.4}$$

$$HCO_3^- \rightarrow H^+ + CO_3^{2-} \qquad K_{2,CO_2} = \frac{c_{b,CO_3^{2-}} \times c_{b,H^+}}{c_{b,HCO_3^-}} \tag{3.5}$$

where K_{1,CO_2} and K_{2,CO_2} are first and second dissociation constants of carbon dioxide, respectively. To properly calculate concentrations of H^+ and OH^-, water dissociation reaction should be considered in the analysis. Thus:

$$H_2O \rightarrow OH^- + H^+ \qquad K_w = c_{b,OH^-} \times c_{b,H^+} \tag{3.6}$$

where K_w is water dissociation constant. When hydrogen sulfide presents in the system, additional two dissociation reactions need to be included in the analysis. Aqueous hydrogen sulfide dissociation reaction and their corresponding equilibrium constants are given:

$$H_2S_{(aq)} \rightarrow H^+ + HS^- \qquad K_{1,H_2S} = \frac{c_{b,HS^-} \times c_{b,H^+}}{c_{b,H_2S_{(aq)}}} \tag{3.7}$$

$$HS^- \rightarrow H^+ + S^{2-} \qquad K_{2,H_2S} = \frac{c_{b,S^{2-}} \times c_{b,H^+}}{c_{b,HS^-}} \tag{3.8}$$

K_{1,H_2S} and K_{2,H_2S} are the first and second dissociation of hydrogen sulfide, respectively. Since the value of K_{2,H_2S} is very small, the second dissociation reaction of $H_2S_{(aq)}$ is neglected in this study. All the equilibrium constants of the reactions are corrected for the effect of temperature and ionic strength. Concentrations of CO_2 and H_2S and other corrosive species ($C_{H_2CO_3}, C_{HCO_3^-}, C_{CO_3^{2-}}, C_{H^+}, C_{HS^-}, C_{OH^-}$) in the bulk solution are computed using a solubility model presented in Section 3.2.

3.1.2 Mass Transport Process

Due to electrochemical and chemical reactions, different species (H_2CO_3, $H_2S_{(aq)}$, HS^-, HCO_3^- Fe^{2+}, H^+, CO_3^{2-} and S^-) are produced or consumed on exposed steel surface. As a result, concentration gradients are created between bulk solution and steel surface, which leads to molecular diffusion of the species towards and away from the surface as

demonstrated in Fig. 3.1. In general, the mass transport of corrosive species consists of three mechanisms: i) molecular diffusion; ii) convective diffusion, which occurs in dynamic system; and iii) migration process, which happens due to electrical field. When the diffusion processes are much faster than the electrochemical processes, species concentration gradient at the steel surface is very small. On the other hand, when the diffusion processes is slower than the electrochemical processes, the concentration of the active species near the metal surface becomes very different from the bulk solution. The rate of electrochemical process depends on the species concentration at the surface. Therefore, there exists a two-way coupling between the electrochemical process and other processes occurring in the adjacent solution layer (i.e. diffusion in the boundary layer). In this study, steady state condition is assumed, in which transport rate of species is equivalent to their reduction or oxidation rate at the steel surface. The electro-active species that diffuse toward/away from metal surface in CO_2 and CO_2-H_2S systems are classified as:

I. Reactant species that move from bulk solution to steel surface

$$H^{+}_{(Bulk)} \rightarrow H^{+}_{(Surface)} \tag{3.9}$$

$$H_2CO_{3(Bulk)} \rightarrow H_2CO_{3(Surface)} \tag{3.10}$$

$$HCO^{-}_{3(bulk)} \rightarrow HCO^{-}_{3(Surface)} \tag{3.11}$$

$$H_2S_{(aq)(Bulk)} \rightarrow H_2S_{(aq)(surface)} \tag{3.12}$$

$$HS^{-}_{(Bulk)} \rightarrow HS^{-}_{(surface)} \tag{3.13}$$

II. Product species that move from steel surface to bulk solution

$$Fe^{2+}_{(surface)} \rightarrow Fe^{2+}_{(Bulk)} \quad (3.14)$$

$$CO^{2-}_{3(Surface)} \rightarrow CO^{2-}_{3(Bulk)} \quad (3.15)$$

$$S^{2-}_{(Surface)} \rightarrow S^{2-}_{(Bulk)} \quad (3.16)$$

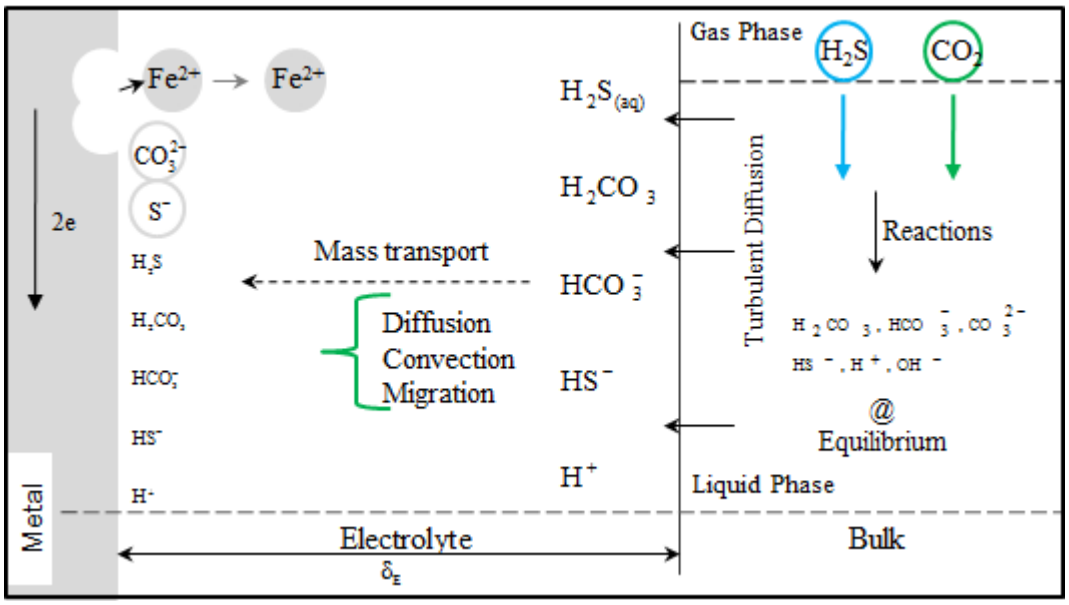

Figure 3.1 Corrosion process occurring in corrosive environment

Under dynamic condition, corrosive fluid moves with respect to the metal surface such as turbulent flow in the oil production pipelines. Therefore, the influence of convective diffusion on the transport process should be considered as an accelerating factor. Turbulent eddies can usually penetrate into the boundary layer and significantly enhance species transport. Compared to fast electrochemical reactions, mass transfer of H^+ occurs at considerably slower rate; and therefore, the rate of overall reaction will be limited by the mass transfer process (i.e. how fast the species can move through the

mass transfer layer and any solid corrosion product layer). The electro-migration mechanism, which is generated due to potential gradient is very small compared to other mass transport mechanisms, therefore, its impact is neglected.

3.1.3 Electrochemical Reactions

Due to presence of structural discontinuity and defects in metallic materials, anodic and cathodic reactions occur on a corroded surface as a coupled process. In CO_2 aqueous system, the dissolution of iron (oxidation reaction) in brine solution is described as the anodic reaction (dissolution). For modeling purpose, the most commonly used anodic reaction is the one proposed by Bockris et al. (1961). Thus:

$$Fe + OH^- \longrightarrow FeOH + e^- \tag{3.17}$$

$$FeOH \xrightarrow{RD} FeOH^+ + OH^- \tag{3.17a}$$

$$FeOH^+ \longrightarrow Fe^{2+} + OH^- \tag{3.17b}$$

The reaction rate in Eqn. (3.17) can be retarded either by shortage of oxidizing species on the cathodic side or accumulation of iron ions near the metal surface. In CO_2 aqueous system and pH > 4, the exchange current density of iron dissolution is assumed to be more affected by the surface coverage of OH^- than solution pH (Bockris et al. 1961). However, recent study (Nesic et al. 1996) measurements reveal that iron dissolution reaction is not significantly affected by OH^- concentration at pH above 4, although it is affected by the presence of CO_2 (Davies and Burstein 1980 and Videm

1993). Therefore, the electrochemical dissolution of iron is expressed as (Nordsveen et al. 2001):

$$Fe \longrightarrow Fe^{2+} + 2e^{-} \tag{3.18}$$

According to previous studies (Nesic et al. 1996; Kahyarian et al. 2015), cathodic reaction is pH-dependent. In strong acids, in which the H_2CO_3 fully dissociated, CO_2 accelerates corrosion of carbon steel primarily by hydrogen evolution (reduction) reaction. The hydrogen reduction reaction is described according to the following equation:

$$2H^{+} + 2e^{-} \rightarrow H_2 \tag{3.19}$$

The rate of iron dissolution in Eqn. (3.18) depends on the amount of H^+ moved from the bulk to the metal surface. The hydrogen evolution is an important and most dominant reaction in the total cathodic reduction when pH is less than 4. However, when pH is between 4 and 6, the direct reduction of carbonic acid becomes influential in addition to the hydrogen ions reduction (Nesic et al. 1996; Nordsveen et al., 2001):

$$2H_2CO_3 + 2e^{-} \rightarrow H_2 + 2HCO_3^{-} \tag{3.20}$$

The direct carbonic acid reduction is controlled by a slow chemical step, carbon dioxide hydration reaction (Eqn. 3.3). Carbonic acid increases CO_2 corrosion rate by accelerating the cathodic reaction in two different mechanisms (Tran et al. 2015). First, the direct reduction mechanism occurs when the adsorbed H_2CO_3 molecules are

consumed at the steel surface (Eqn. 3.19). This mechanism was originally suggested by deWaard and Milliams (1975). Alternative approach is that carbonic acid works as a source of hydrogen ions through the dissociation reaction (Eqn. 3.4), which promotes hydrogen ion reduction as dominated cathodic reaction. This mechanism is referred as buffering effect. In a less corrosive environment (pH > 5), additional cathodic reaction known as direct bicarbonate reduction becomes important (Gray et al. 1990):

$$2\,HCO_3^- + 2\,e^- \rightarrow H_2 + 2\,CO_3^{2-} \tag{3.21}$$

When H_2S is added to CO_2 aqueous system, the electrolyte solution contains increased number of ions (H^+, H_2CO_3, HCO_3^-, CO_3^{2-} H_2S, HS and S^{2-}) due to hydration and dissociation reactions. Therefore, the electrochemical reactions occurring at steel surface in sour environment are relatively complex process. In addition to the reduction reactions (Eqns. 3.18 to 3.20) that are considered in CO_2 corrosion process, two supplementary reactions (Eqns. 3.22 and 3.23) are involved in the total cathodic reaction. These reactions are defined as direct reduction of aqueous H_2S and HS^-.

$$2\,H_2S + 2\,e^- \rightarrow H_2 + 2\,HS^- \tag{3.22}$$

$$2\,HS^- + 2\,e^- \rightarrow H_2 + 2\,S^- \tag{3.23}$$

The direct reduction of aqueous H_2S has been proposed (Zheng et al. 2015; Zheng et al. 2014) recently for modeling H_2S and CO_2-H_2S corrosion. In addition, buffering mechanism is proposed by Kittel et al. (2013) to account for contribution of H_2S through its dissociation reactions (Eqn. 3.8) as an additional source of protons at the

corroding surface. As a result, in CO_2-H_2S corrosion environment, the cathodic process is described using five formulas that show the reduction reactions occurring at the cathode (Zhang et al. 2012). The reactions involved in the cathodic process are test condition-dependent (i.e. CO_2 and H_2S partial pressure and pH-dependent). On the other hand, the anodic dissolution strongly depends on H_2S concentration (Zheng et al. 2014). Therefore, the exchange current density is expected to be more influenced by HS^- than OH^-. In this study, the impact of HS^- on iron dissolution rate is taken in to consideration as suggested by recent studies (Zheng et al. 2013; Zheng et al. 2015).

3.2 Solubility Model for Gas Mixture at HPHT

Solubility of acidic gases has a strong impact on corrosion process. Therefore, accurate prediction of dissolved amount of CO_2, H_2S and other corrosive species (ions produced from dissociation reaction) helps to improve performance of corrosion model. In this study, an improved solubility model is developed based on existing models (Duan et al. 2007; Duan and Sun 2003; Mao and Duan 2006; Duan and Mao 2006; Zirrahi et al. 2012). The model is specially formulated to predict solubility of common acidic gases in brine under HPHT condition. Afterward, the model is coupled with another systematic model for estimating concentration of the ions resulting from dissociation reactions of aqueous CO_2 and H_2S. Therefore, the first step is development of a comprehensive model to predict dissolved amount of gas mixture in brine. It is noteworthy that existing models are developed for predicting solubility of single corrosive gas in the brine. In this study, a mixed gas system containing CO_2, H_2S and CH_4 is considered.

Under equilibrium condition, a number of homogenous chemical reactions occur in aqueous CO_2-H_2S system including CO_2 and H_2S dissolution in brine, which are described in Eqns. (3.1 and 3.2). The dissolved amount of CO_2 and H_2S can be computed by adopting similar approach that was presented in the previous models (Duan et al. 2007; Duan and Sun 2003). The approach is assuming the chemical potential balance between the gas and liquid phases. The chemical potential for component (*i*) can be described in terms of fugacity in the vapor phase and activity in the liquid phase.

$$\mu_i^V(T,P,y) = \mu_i^{V(0)}(T) + RT\ln y_i P + RT\ln\varphi_i(T,P,y) \tag{3.24}$$

$$\mu_i^l(T,P,y) = \mu_i^{l(0)}(T,P) + RT\ln m_i P + RT\ln\gamma_i(T,P,m) \tag{3.25}$$

where subscript *i* refers to the components presenting in the gas phase such as carbon dioxide, hydrogen sulfide, and methane. It is assumed that, both equations (Eqns. 3.24 and 3.25) are equalized for each component at equilibrium condition. After rearrangement, mole fraction of dissolved gases in the liquid can be expressed as:

- Molality of Carbon dioxide

$$\ln m_{CO_2} = \ln(y_{CO2}\times\varphi_{CO_2}\times P) - \frac{\mu_{CO_2}^{l(0)}}{RT} - \ln\gamma_{CO_2} \tag{3.26}$$

- Molality of Hydrogen sulfide

$$\ln m_{H_2S} = \ln(y_{H_2S} \times \varphi_{H_2S} \times P) - \frac{\mu_{H_2S}^{l(0)}}{RT} - \ln \gamma_{H_2S} \tag{3.27}$$

- Molality of Methane

$$\ln m_{CH_4} = \ln(y_{CH_4} \times \varphi_{CH_4} \times P) - \frac{\mu_{CH_4}^{l(0)}}{RT} - \ln \gamma_{CH_4} \tag{3.28}$$

where y_{CO_2}, y_{H_2S}, y_{CH_4} are mole fraction of CO_2, H_2S, and CH_4 in the gas phase after normalization. φ_{CO_2}, φ_{H_2S}, and φ_{CH_4} are the fugacity coefficient of carbon dioxide, hydrogen sulfide and methane. P is total pressure in (bar). $\frac{\mu_i^{l(0)}}{RT}$ term is defined as interaction parameter and it is different for each species, referred as Par (T, P). The parameter (Par) is a function of pressure and temperature. It is calculated using empirical models (Duan et al. 2003; 2006; 2007). A detailed calculation procedure for the parameter is presented elsewhere (Elgaddafi 2016a). Equations from 3.26 to 3.28 give the dissolved amount of CO_2, H_2S and CH_4 as a function of their gas phase properties and their activities in the liquid phase. Under particular condition, some amount of water evaporates and stays in the gas phase; therefore, the exact gas composition is more complex. Since the amount of water vapor is unknown, an iterative numerical procedure is commonly used to determine the exact composition of the gas phase. In this study, semi-empirical equation developed by Duan and Mao (2006) is utilized to estimate mole fraction of water vapor as:

$$\mathrm{y_{H_2O}} = \frac{\mathrm{x_{H_2O}}.\mathrm{P_{H_2O}^S}}{\varphi_{\mathrm{H_2O}}.\mathrm{P}} \exp\left(\frac{\nu'_{\mathrm{H_2O}}\left(\mathrm{P} - \mathrm{P_{H_2O}^S}\right)}{\mathrm{RT}}\right) \tag{3.29}$$

where X_{H_2O} is mole fraction of water in liquid phase, which is approximately 1 for CO_2-H_2S system. $P^S_{H_2O}$ and $\upsilon^{'}_{H_2O}$ are water saturation pressure and molar volume of liquid, respectively. φ_{H_2S} is fugacity coefficient of water in gas phase, which is obtained from an empirical model presented in Elgaddafi et al. (2016a). After mole fraction of water vapor is determined, mole fractions of other gas components are computed applying the material balance equation, and then the gas phase mole fractions are utilized in the solubility calculation.

The parameters needed to apply the solubility equations (Eqns. 3.26-3.28) are calculated as follows. The activity coefficients for aqueous CO_2, H_2S, CH_4, γ_i , are calculated using models suggested by Duan and Sun (2003), Duan and Mao (2006), and Duan et al. (2007), respectively. The general formula for the activity coefficient, which is applicable for a three-component system, is given by:

$$\ln \gamma_i = \sum_c 2\lambda_{i-c} m_c + \sum_a 2\lambda_{i-a} m_a + \sum_c \sum_a \zeta_{i-c-a} m_c m_a \tag{3.30}$$

where subscript of m_c and m_a denotes anions and cations molality, respectively, λ_{i-a} and, ζ_{i-c-a} are the second and third order interaction parameters, respectively. The parameters are calculated with appropriate T-P coefficients, as presented elsewhere (Elgaddafi et al. 2016a). Subscripts a and c denote anion and cation, respectively. In the vapor phase, fugacity coefficients of CO_2, H_2S, and CH_4 (Eqns. 3.26-3.28) are calculated based on the Peng-Robinson equation of state (PR-EOS). Details of the fugacity coefficient calculation are presented in Elgaddafi et al. (2016a). The

intermolecular attraction and repulsion terms of a mixture (a_{mix} and b_{mix}) are calculated using mixing rules. In order to estimate bulk concentrations of carbon dioxide and hydrogen sulfide in brine solution, a system of equations presented in Section 3.2 is utilized.

After dissolution of carbon dioxide and hydrogen sulfide in the liquid phase, numbers of homogenous chemical reactions take place in the brine including CO_2 hydration and dissociation reaction producing corrosive environment. Hydration and dissociation reaction equations are presented in Section 3.1.1 with their corresponding equilibrium constants. Using these equations, a system of equations with a number of unknown ionic concentrations $C_{H_2CO_3}, C_{HCO_3^-}, C_{CO_3^{2-}}, C_{H^+}, C_{HS^-}, C_{OH^-}$ is generated. To predict the unknown ionic concentrations, a new model consisting of non-linear system of equations is developed and coupled with the solubility model. However, there are six unknowns and four equations. Two additional equations are needed to complete the model. Therefore, electro-neutrality and material balance equations are utilized. In aqueous CO_2-H_2S system, electro-neutrality can be described using the following formula:

$$C_{H^+} = C_{OH^-} + C_{HCO_3^-} + 2C_{CO_3^{2-}} + C_{HS^-} \tag{3.31}$$

Carbon in the system is preserved during corrosion process. Hence, carbon material balance in the system can be expressed as:

$$C_{CO_2} = C_{H_2CO_3} + C_{HCO_3^-} + C_{CO_3^{2-}} \tag{3.32}$$

Once Eqns. (3.31) and (3.32) incorporated into the system of equations, the model equations (six non-linear equations) require numerical procedure to predict the bulk concentration of each species. To solve the system of equations numerically, a computer program is developed using Mathlab. The program predicts bulk concentration of species in aqueous solution as a function of temperature and pressure. Predictions of the model (concentration of species) are used in corrosion models presented in Chapter 4.

3.3 Solution pH Prediction

The calculation approach of pH is traditionally derived from the electro-neutrality equation as illustrated in Eqn. (3.31). Once the proton ion concentration (H^+) is determined, the pH is simply calculated from hydrogen activity in liquid as:

$$pH_1 = -\log\left[C_{H^+}\right] \tag{3.33}$$

In Eqn. (3.33), the effect of ionic interaction in the solution is ignored. However, other studies (Plennevaux et al. 2013; Spitzer et al. 2011) defined pH value according to the International Union of Pure and Applied Chemistry (IUPAC) recommendation, which is a negative logarithm of the relative activity of the hydrogen ion (a_{H^+}):

$$pH_2 = -\log\left[a_{H^+}\right] = -\log[\gamma_{H^+} \times C_{H^+}] \tag{3.34}$$

where C_{H^+} is the hydrogen ion concentration and γ_{H^+} is the activity coefficient. The activity coefficient of H^+ in the liquid phase is calculated by applying the Pitzer's model (Pitzer et al. 1984). Thus:

$$\ln \gamma_{H^+} = -\left|z_{H^+} z_{Cl^-}\right| . A_\phi \left[\frac{I^{0.5}}{1+b.I^{0.5}} + \frac{2}{b} \ln\left(1+b.I^{0.5}\right) \right] + m \frac{\nu_{H^+}.\nu_{Cl^-}}{\nu} \left\{ 2\beta^{(0)}_{H^+Cl^-} + \frac{2\beta^{(1)}_{H^+Cl^-}}{\alpha^2 I} \left[1 - \left(\alpha\ I^{0.5} - \frac{\alpha^2 I}{2} \right) e^{-\alpha^2 I} \right] \right\} \quad (3.35)$$
$$+ \frac{3m^2}{2} \left[\frac{2\left(\nu_{H^+}.\nu_{Cl^-}\right)^{3/2}}{\nu} C^{\phi}_{H^+Cl^-} \right]$$

To determine H^+ activity coefficient, Eqn. (3.35) is applied to HCl solution containing ν_{H^+} and ν_{Cl^-} ions of charge of z_{H^+} and z_{Cl^-}, where b is a factor related to ion size and its value is 1.2 $kg^{0.5}/mol^{0.5}$, *m* is molality of the electrolyte, and *I* is the ionic strength:

$$I = \frac{1}{2} \sum_i m_i . z_i^2 \quad (3.36)$$

$\beta^{(0)}_{H^+Cl^-}$, $\beta^{(1)}_{H^+Cl^-}$, and $C^{\phi}_{H^+Cl^-}$ are the Pairwise and Triplet ion-interaction parameters of Pitzer's equation (Eqn. 3.36). These ion-interaction parameters are called Par (ρ, P, T) and obtained from the equation proposed by Holmes et al. (1987) as a function of pressure, temperature and solution density:

$$Par(\rho, P, T) = q_1 + q_2 \ln(\rho / \rho_R) + q_3 \left(\rho - \rho_R\right) / \rho^* + q_4 \left(T - T_R\right) / T^* + q_5 \left(P - P_R\right) / P^* \quad (3.37)$$

where q's are adjustable parameters which are given in Table 3.1, ρ is the density of the brine, ρ^* is 1 kg/m^3, T^* is 1 K, P^* is 1 MPa. T_R, P_R, and ρ_R are the reference temperature, pressure, and density, respectively and their values are presented in Table

3.1. It should be noted that the ion-interaction parameters obtained from Table 3.1 are valid for a wide range of temperature (273 - 523 K) and molality (0-16 m).

Table 3.1 Constant values of the Pairwise and Triplet parameters

Parameter constant	$\beta^{(0)}_{H^+Cl^-}$	$\beta^{(1)}_{H^+Cl^-}$	$C^{\phi}_{H^+Cl^-}$
q1	0.17579	0.2924	2.070×10^{-3}
q2	-0.07079	16.753	-
q3	-	-18.271×10^{-3}	-
q4	-3.9004×10^{-4}	-	-3.9390×10^{-5}
q5	1.07800×10^{-4}	-2.95×10^{-4}	-
T_R = 298.15 K, P_R = 0.101325 MPa, and ρ_R = 997.062 kg/m^3			

In Eqn. (3.35), A_ϕ is Debye-Huckel parameter for osmotic coefficient and it is normally given by (Pitzer et al. 1984):

$$A_\phi = \frac{1}{3}\left(\frac{2\pi N_A d_w}{1000}\right)^{0.5}\left(\frac{e^2}{DkT}\right)^{3/2} \tag{3.38}$$

For simplicity, a temperature-dependent expression proposed by Steiger et al. (2008) is utilized to predict A_ϕ as:

$$A_\phi = -0.817653 - 0.8685276/(T-222) + 1.9251\times10^4/T^2 + 0.5251284\times10^{-2}T - 7.149397\times10^{-6}T^2 + 9.3385\times10^{-12}T^4 \tag{3.39}$$

Equation (3.39) is validated with data available in the literature (Pitzer et al. 1984) at various pressures and temperature. The results showed that Debye-Huckel parameter is pressure-independent.

Chapter 4 : CORROSION MODEL

Accurate prediction of corrosion is one of important elements of engineering design. Modeling corrosion requires essentially a comprehensive knowledge of corrosion mechanisms as well as thermodynamic properties of corrosive gases. In this study, two mechanistic corrosion models are developed to predict CO_2 and CO_2-H_2S corrosion. First, electrochemical-based CO_2 corrosion model is established to predict corrosion rate of carbon steel in film-free conditions. Afterward, the model has been upgraded to incorporate the presence of H_2S combined with CO_2 (sour corrosion model). The second model is an improved version of an existing model Nesic et al. (2009), which predicts CO_2-H_2S corrosion assuming mass transport as a rate-controlling step. The model is improved by accounting for non-ideal water chemistry. In this chapter, formulations of these models are presented.

4.1 Electrochemical Based Corrosion (EBC) Models

4.1.1 CO_2 Corrosion Model

The most accepted CO_2 corrosion mechanism consists of cathodic (reduction of H^+, H_2CO_3 and HCO_3^-) and anodic (iron dissolution, Fe^{2+}) reactions. The mechanism involves five steps: i) dissolution of corrosive gases into liquid phase; ii) chemical reactions in the bulk solution; iii) corrosive species mass transport from the bulk to the steel surface; iv) electrochemical reaction at the steel surface; and v) transportation of corrosion products to the bulk solution. These steps are shown in Fig. 3.1. The EBC model has been developed for CO_2 corrosion considering these five steps, and ignoring

contribution of the protective scale. The model is designed to perform in stagnant and dynamic corrosion environments. The corrosion process is described mathematically considering the following steps:

I. Dissolution of Corrosive Gases into Liquid Phase

CO_2 and H_2S gases are highly soluble in brine solutions. The physical and mathematical description of gas solubility model used in EBC model is presented in Section 3.2.

II. Electrochemical Process

The electrochemical reactions are characterized by anodic and cathodic currents. The current densities developed due to the electrochemical reactions (Eqns. 3.18 – 3.21). They are computed using the Butlere-Volmer equations:

- Anodic reaction rate (iron dissolution):

$$i_a = 2FK_{e,Fe^{2+}} c_{s,Fe^{2+}} \exp\left[\frac{(2-\beta)\times F\times(E_{corr}-E_{Fe^{2+}})}{R\times T}\right] \quad (4.1)$$

- Cathodic reaction rate (reduction of H^+, H_2CO_3 and HCO_3^-):

$$i_{c,i} = 2FK_{e,i} c_{s,i} \exp\left[\frac{-\beta\times F\times(E_{corr}-E_i)}{R\times T}\right] \quad (4.2)$$

where the subscript i represents the components of H^+, H_2CO_3 or HCO_3^-. F is Faraday's constant, which is 96,500 C/mol. $K_{e,Fe^{2+}}$ and $K_{e,i}$ are standard electrochemical reaction rate constants of anodic and cathodic reactions, respectively. These constants are temperature-dependent parameters and their values are related to bulk species concentrations at reference condition (Kahyarian et al. 2015). $K_{e,Fe^{2+}}$ is related to the exchange current density of iron dissolution reaction, which is a unique property for each type of carbon steel (Nesic et al. 1996). Therefore, suitable values of $K_{e,Fe^{2+}}$ are selected for tested material to calibrate the model. The electrochemical reaction rate constants are provided in Table 4.1. The rate constants for cathodic reactions are obtained from previous studies (Dayalan et al. 1998; Wang et al. 2002). β is a transfer coefficient, which is 0.5 for most of the reactions (Dayalan et al. 1995; Wang et al. 2002). R is the universal gas constant, which is 8.314 J/mol.K, and T is absolute temperature (K). The equilibrium potentials of hydrogen and iron ions (E_{H^+} and $E_{Fe^{2+}}$) are expressed using the Nernst equation as:

$$E_{H^+} = E^0_{H^+} + \frac{RT}{nF} \ln\left[\frac{(c_{s,H^+})^2}{c_{s,H_2}}\right] \tag{4.3}$$

$$E_{Fe^{2+}} = E^0_{Fe^{2+}} + \frac{RT}{nF} \ln\left[c_{s,Fe^{2+}}\right] \tag{4.4}$$

$E^0_{H^+}$ and $E^0_{Fe^{2+}}$ are the standard potentials of hydrogen and iron ions, respectively. The standard potential values for oxidation and reduction reactions (Eqns. 3.18 – 3.21) are

obtained from previous studies (Wang et al. 2002; Sompalli 1996). In Eqns. (4.3 and 4.4), C_{s,H_2} and $C_{s,Fe^{2+}}$ are surface concentration of hydrogen molecule and iron ions in mol/m^3.

Table 4.1 Standard electrochemical reaction rate constants for different tested materials

Test environment	CO_2 saturated brine		CO_2-H_2S saturated brine
	38°C	71°C	38°C
$K_{e,Fe^{2+}}$ T95 carbon steel (m/s)	2.56×10^{-4}	9.0×10^{-12}	2.59×10^{-5}
$K_{e,Fe^{2+}}$ C110 carbon steel (m/s)	N/A	N/A	1.5×10^{-6}
$K_{e,Fe^{2+}}$ Q125 carbon steel (m/s)	9.0×10^{-7}	7.0×10^{-11}	9.0×10^{-7}

III. Mass Transport Process

Due to electrochemical reactions occurring at metal surface, species concentration gradients are formed, which are normal to the steel surface. The fluxes of the electro-active species forward and away from the steel surface are attributed to the existence of different mechanisms. Under dynamic condition, the species mass transport mechanism consists of molecular diffusion, convective diffusion and migration process. The migration related mass transfer of species is negligible compared to the diffusive and convective mass transfers. In this study, mass transfer rates of reactants (H_2CO_3, HCO_3^- and H^+) and products (Fe^{2+} and CO_3^{-2}) involved in electrochemical reaction (Eqns. 3.9 – 3.16) are defined by adopting existing model (Yabuki, 2011):

$$\text{Mass transfer rate of products} = K_{mt}\left(c_{s,P} - c_{b,P}\right) \tag{4.5}$$

$$\text{Mass transfer rate of reactants} = K_{mt}\left(c_{b,R} - c_{s,R}\right) \tag{4.6}$$

where K_{mt} symbolizes the mass transfer coefficient of corrosive species. $c_{s,P}$, $c_{b,P}$, $c_{s,R}$, and $c_{b,R}$ are surface and bulk concentrations of products and reactants, respectively. The bulk concentrations of corrosive species are obtained from the solubility model (Chapter 3). The mass transfer coefficient for all species is required for calculating mass transport rates. For steady state and quiescent (i.e. stagnant fluid) condition, K_{mt} is approximately 1×10^{-4} m/s for all species (Sun and Nešić 2009). In scale-free CO_2 corrosion process, fluid flow promotes mass transport process and ultimately increases the corrosion rate. To simulate effect of single-phase flow on mass transport, the hydrodynamic parameters (Reynolds number and Schmidt number) are coupled with mass transport parameter (Sherwood number). For a rotating cylinder, the mass transfer parameter of species *i* in turbulent single-phase flow, is estimated using the Eisenberg's correlation (1954):

$$Sh = \frac{k_{m,i} L}{D_i} = 0.079 \times \mathrm{Re}^{0.7} \times Sc^{0.36} \tag{4.7}$$

where $K_{m,i}$ is the mass transfer coefficient of species *i* involved in corrosion process (m/s), L is the characteristic length (m), and D_i is the diffusion coefficient of species *i* (m^2/s). Re is the Reynolds number [$\rho U d_c / \mu$], and Sc is the Schmidt number [ν / D_i], ρ is solution density (kg/m^3), U is the mean fluid velocity, d_c is diameter of the cylinder, μ is solution viscosity, ν is the kinematic viscosity. Once the mass transfer coefficients for all electrochemical species are calculated, the mass transfer flux of the species moving through the electrolyte can be determined. When temperature changes,

the mass transfer coefficient needs to be adjusted by correcting the diffusivity of the species. Some parameters such as diffusion coefficient, density and viscosity of brine appeared in Eqn. (3.7) are also corrected for temperature variation. The effect of temperature on the diffusion coefficient (D_i) can be predicted using the Stokes-Einstein equation:

$$D_i = D_{i\_ref} \times \frac{T}{T_{ref}} \times \frac{\mu_{ref}}{\mu} \tag{4.8}$$

D_{i_ref} is the diffusion coefficient of species *i* at standard temperature (20°C). The diffusion coefficient values of the species involved in corrosion process are obtained from previous studies (Nordsveen et al. 2003). T and T_{ref} are test and reference temperature in K. μ and μ_{ref} are water viscosity at test and reference temperatures, respectively. Density (kg/m^3) and viscosity (kg/m.s) of brines are estimated using the following correlations (Nesic et al. 1996):

$$\rho = 1{,}152 - 0.5116 \times T \tag{4.9}$$

$$\mu = \mu_{ref} \times 10^{\frac{1.3272(20-t_c)-0.001053(20-t_c)^2}{T+105}} \tag{4.10}$$

A. Model Assumption

As mentioned earlier, five physico-chemical process steps are involved in CO_2 corrosion process, which are mathematically described using fundamental equations. These steps are included in the model formulations. Under steady state condition, the following assumption can be made to establish the model:

I. The sum of cathodic reaction currents must be equal to the sum of anodic reaction currents.

$$i_{H^+} + i_{H_2CO_3} + i_{HCO_3^-} = i_{Fe^{2+}} = i_{corr} \tag{4.11}$$

II. The sum of mass transfer rates must be equal to the sum of electrochemical reaction rates.

For anodic reaction

$$i_{Fe^{2+}} = 2FK_{mt,Fe^{2+}}\left(c_{s,Fe^{2+}} - c_{b,Fe^{2+}}\right) \tag{4.12}$$

For cathodic reaction

$$\begin{aligned} i_{H^+} + i_{H_2CO_3} + i_{HCO_3^-} &= FK_{mt,H^+}\left(c_{b,H^+} - c_{s,H^+}\right) + FK_{mt,H_2CO_3}\left(c_{b,H_2CO_3} - c_{s,H_2CO_3}\right) \\ &+ FK_{mt,HCO_3^-}\left(c_{b,HCO_3^-} - c_{s,HCO_3^-}\right) \end{aligned} \tag{4.13}$$

III. Under steady state condition, mass balance of carbonate species can be expressed as:

$$FK_{mt,H_2CO_3}\left(c_{b,H_2CO_3} - c_{s,H_2CO_3}\right) + FK_{mt,HCO_3^-}\left(c_{b,HCO_3^-} - c_{s,HCO_3^-}\right) = FK_{mt,CO_3^{2-}}\left(c_{s,CO_3^{2-}} - c_{b,CO_3^{2-}}\right) \tag{4.14}$$

IV. The first and second dissociations of carbonic acid and water dissociation occur at the steel surface. Equilibrium constants of these reactions are given in Eqns. (3.4), (3.5) and (3.6).

B. Model Solution and Implementation

Applying these assumptions, a system of seven nonlinear equations (Eqns. 3.4 – 3.6 and 4.11– 4.14) with seven unknowns is developed. The unknowns are concentrations of iron ion and corrosive species ($Fe^{2+}, H^{+}, H_2CO_3, HCO_3^{-}, CO_3^{2-}, OH^{-}$), and corrosion potential (E_{corr}). The unknowns are obtained by solving the system of equations numerically using Newton-Raphson method. The corrosion current density (i_{corr}), which is equal to total cathodic or anodic current density, can be determined from the solution. Corrosion rate is proportional to the current density (Wang et al. 2002). Thus:

$$CR(mm/y) = 1.16 \times i_{corr} \tag{4.15}$$

After formulation, the model is implemented into a computer code to solve the system of equations numerically and determine corrosion rate. The model incorporates solubility, pH and gas compressibility calculation procedures to determine bulk concentrations of the corrosive species, compressibility factor and fugacity coefficients. Input variables for the model are: gas composition, total pressure, temperature, salt concentration, type of steel, and flow velocity. The initial concentration of iron ion is assumed 1.0×10^{-10} mol/m^3. The steps of the corrosion rate are described by the flowchart shown in Fig. 4.1.

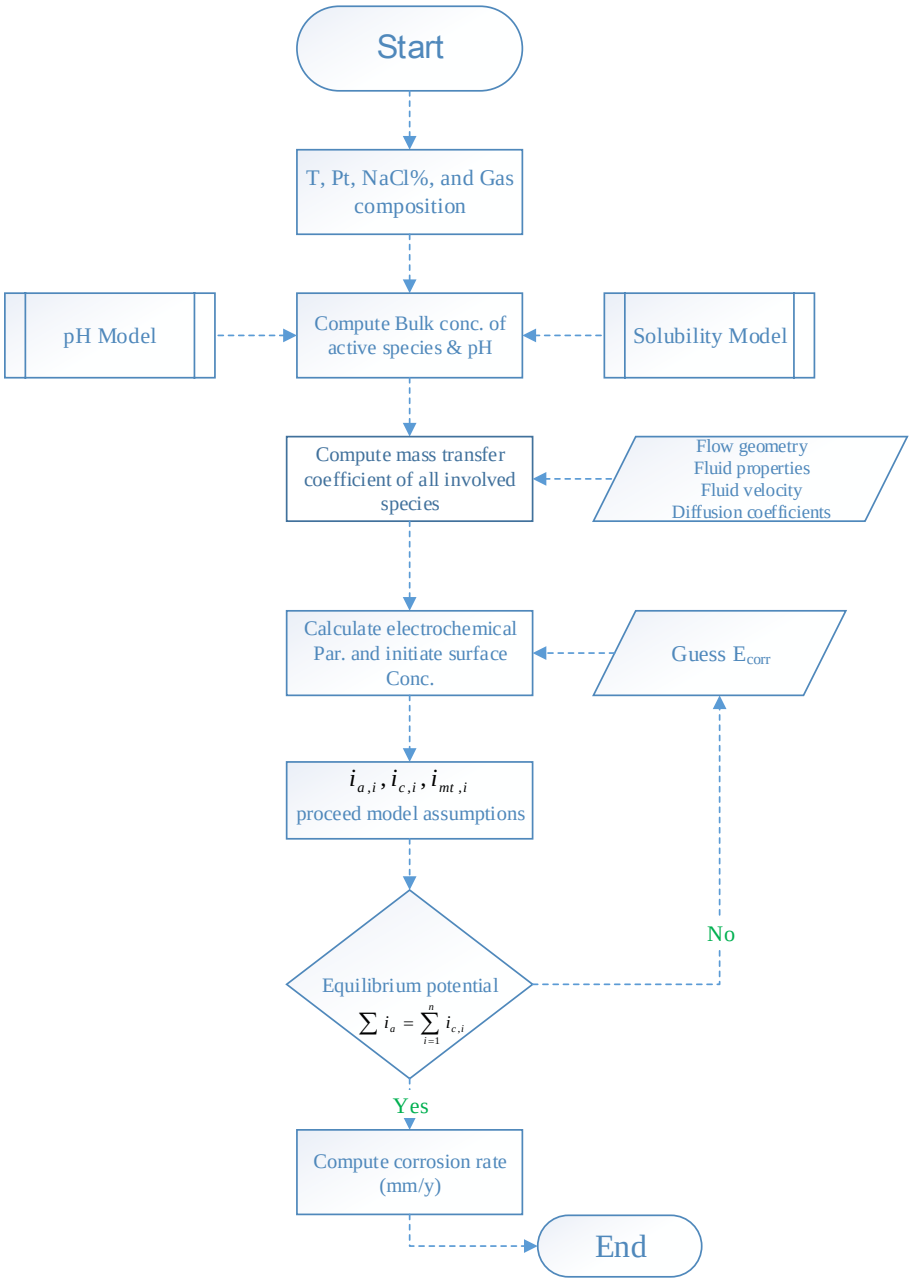

Figure 4.1 Computational flowchart for electrochemical-based corrosion model

4.1.2 CO_2-H_2S Corrosion Model

CO_2 corrosion model developed in this study is extended to account for the presence of H_2S in combination with CO_2. In conditions that are unfavorable for the formation of corrosion scale (i.e. scale unfavorable), adding hydrogen sulfide to a CO_2 containing

environment effects physico-chemical processes involved in the CO_2 corrosion process. H_2S quickly dissolves in brine forming weak acid whereas CO_2 takes slower steps to form carbonic acid and associated corrosive species. As a result, H_2S often leads the corrosion process.

The impact of H_2S or any other impurities on thermodynamic properties of CO_2 is discussed in Chapter 3. According to previous corrosion experiments (Zheng et al. 2013; 2014; 2015; Zhang et al. 2012), the presence of H_2S has significant influence on the electrochemical reactions at the metal surface, in which the anodic reaction becomes more depended on the HS^- surface concentration. Hence, two additional reduction reactions are added to the total cathodic reaction (H_2S direct reduction and HS^- reduction).

In the CO_2-H_2S system, the rate of iron dissolution is calculated using Eqn. (4.1) after it is corrected for the effect of HS^- ions surface concentration, as it proposed by (Zheng et al. 2014). The rate of direct reduction of H_2S and HS^- is obtained using Eqn. (4.2). The electrochemical parameters, which are shown in Eqns. (4.1 and 4.2) related to H_2S. The standard potentials in Eqns. (3.22 and 3.23) are determined as suggested by previous studies (Wang et al. 2002; Tanaka and Tamamushi, 1961, Foroulis, 1980). The electrochemical rate constant of the anodic reaction is material characteristic and it is not affected by the environment. Therefore, the value of $K_{e,Fe^{2+}}$ is kept constant whereas that of K_{e,H_2S} and K_{e,HS^-} are calculated following the method presented by Zheng et al. (2013). The mass transport rate of reactants (H_2S and HS^-) and products (

S^{2-}) species are similarly described by Eqns. (4.5 – 4.6), in which the mass transfer coefficients are determined from Eqn. (4.8). In addition, the model assumptions are slightly changed due to the presence of hydrogen sulfide.

A. Model Assumption

I. The sum of cathodic reaction current densities must be equal to the sum of anodic reaction current densities. Thus:

$$i_{H^+} + i_{H_2CO_3} + i_{HCO_3^-} + i_{H_2S} + i_{HS^-} = i_{Fe^{2+}} = i_{corr} \tag{4.16}$$

where i_{corr} is the corrosion current density.

II. The sum of mass transfer rates must be equal to the sum of electrochemical reaction rates. Therefore, the anodic reaction current density can be related to mass transfer rate of iron ions. Thus:

$$i_{Fe^{2+}} = 2FK_{mt,Fe^{2+}}\left(c_{s,Fe^{2+}} - c_{b,Fe^{2+}}\right) \tag{4.17}$$

Similarly, for cathodic reaction, the total current density can be related to total mass transfer rate of corrosive species as:

$$\begin{aligned} i_{H^+} + i_{H_2CO_3} + i_{HCO_3^-} + i_{H_2S} + i_{HS^-} &= FK_{mt,H^+}\left(c_{b,H^+} - c_{s,H^+}\right) + FK_{mt,H_2CO_3}\left(c_{b,H_2CO_3} - c_{s,H_2CO_3}\right) \\ &+ FK_{mt,HCO_3^-}\left(c_{b,HCO_3^-} - c_{s,HCO_3^-}\right) + FK_{mt,H_2S}\left(c_{b,H_2S} - c_{s,H_2S}\right) + FK_{mt,HS^-}\left(c_{b,HS^-} - c_{s,HS^-}\right) \end{aligned} \tag{4.18}$$

III. Masses of carbonate and aqueous hydrogen sulfide species are conserved. Thus:

$$FK_{mt,H_2CO_3}\left(c_{b,H_2CO_3}-c_{s,H_2CO_3}\right)+FK_{mt,HCO_3^-}\left(c_{b,HCO_3^-}-c_{s,HCO_3^-}\right)=FK_{mt,CO_3^{2-}}\left(c_{s,CO_3^{2-}}-c_{b,CO_3^{2-}}\right) \quad (4.19)$$

$$FK_{mt,H_2S}\left(c_{b,H_2S}-c_{s,H_2S}\right)+FK_{mt,HS^-}\left(c_{b,HS^-}-c_{s,HS^-}\right)=FK_{mt,S^-}\left(c_{s,S^-}-c_{b,S^-}\right) \quad (4.20)$$

IV. The first and second dissociations of carbonic acid, aqueous hydrogen sulfide and water dissociation occur at the steel surface. Equilibrium constants of these reactions are presented earlier (Eqns. 3.4 to 3.8).

B. Model Solution

To obtain model solution, first bulk concentrations of involved species are determined using the solubility model, then mass transfer coefficients and equilibrium constants are inserted in the model expressions to establish a system of equations (3.4 – 3.8 and 4.16 – 4.20) with ten unknowns. The unknown variables include all surface concentrations of the involved species produced from chemical and electrochemical reactions in addition to the corrosion potential (E_{corr}). Similar to CO_2 corrosion model, the system of equations is numerically solved using Newton Raphson method to determine the equilibrium potential and subsequently the corrosion current density (i_{corr}) and corrosion rate (Eqn. 4.15).

The electrochemical-based corrosion CO_2-H_2S model developed in this study has incorporated all relevant phenomena involved in corrosion process with the exception of corrosion scale. The model can be used to predict corrosion rate in CO_2

and CO_2-H_2S containing environment under stagnant and dynamic conditions. The model has not been validated for corrosion environment that does not contain CO_2.

4.2 Mass Transport Based CO_2-H_2S Corrosion Model

As described in the literature survey, numerous mathematical models have been developed in the past few years for H_2S and CO_2-H_2S corrosion of carbon steel. However, their applications are limited to oil pipeline, which means restricted to relatively low pressure and low temperature conditions. In this study, an existing Mass Transport Based (MTB) model (Sun and Nesic 2009) has been improved to predict uniform corrosion of steel in wet H_2S and H_2S-CO_2 environment under HPHT. The improvement includes: i) enhancement in accuracy of water chemistry prediction technique by employing the thermodynamic calculation to determine bulk concentration of active species and solution pH, as presented in Chapter 3; and ii) modifications of diffusion and mass transfer coefficients to account for the effects of temperature and fluid velocity.

The MTB model accounts for the influence of H_2S concentration, temperature, flow condition and protective scale on the corrosion process. Thickness and type of iron sulfide layer formed on steel surface change with time and depend on scale-formation and removal rates. It should be noted that the model does not account for a change in FeS scale type. According to surface analysis conducted by Sun and Nesic (2007), mackinawite layer is predominantly iron sulfide, which is formed due to direct

reaction of H_2S with metal surface (Fig. 4.2). Based on experimental observations and theoretical analysis, the following four assumptions are often made in developing the MTB model for aqueous CO_2-H_2S corrosion of steel:

I. Hydrogen sulfide leads the corrosion process; thus, corrosion scale mechanism in aqueous sour system takes place via direct heterogeneous solid-state reaction at steel surface and the overall reaction can be expressed as:

$$Fe_{(S)} + H_2S \rightarrow FeS_{(S)} + H_2 \tag{4.21}$$

II. After short time of exposure, very fluffy and compact mackinawite layer (less than 1 μm) forms on steel surface.

III. At long-time exposure, a thin mackinawite layer that goes continuously through a cyclic process of scale growth, cracking and delamination forms. The cyclic process eventually results in the formation an outer mackinawite layer.

IV. A thicker (greater than 1 μm) and loosely porous outer mackinawite layer is formed on top of the thin layer.

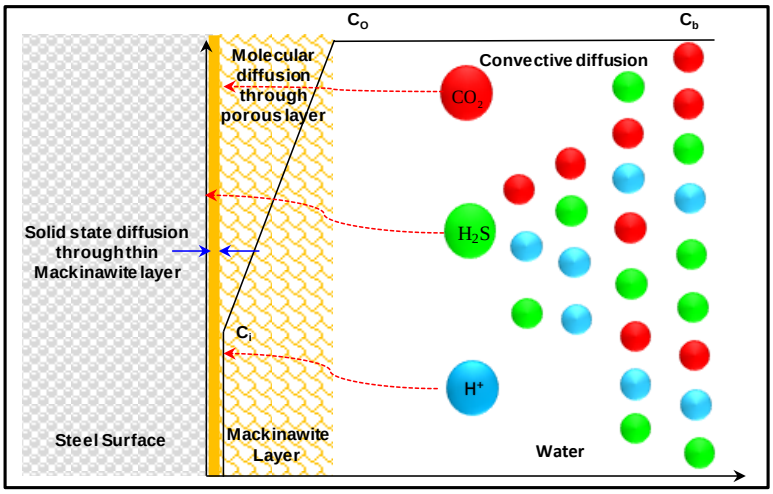

Figure 4.2 Schematic of H_2S corrosion process (adopted from Sun and Nesic 2009)

To formulate the MTB model for CO_2-H_2S corrosion, the contributions of four major factors (H_2S concentration, pH, CO_2 concentration and protective scale) to the total corrosion rate are independently evaluated and modeled.

Effect of H_2S Concentration: In CO_2-H_2S environment, due to formation of mackinawite layers (inner and outer), which works as electronic barrier, the corrosion process is assumed to be under mass transfer control rather than electrochemical or chemical reaction control.

Throughout corrosion process, mass transport of the reactive species occurs via diffusion mechanisms caused by concentration gradients. Various types of diffusion processes (Fig. 4.2) are involved including: convective diffusion in surrounding fluid, molecular diffusion through porous outer layer and solid-state diffusion through thin mackinawite layer. Thus, molecular and ionic fluxes (mol/m^2.s) of the three diffusion processes can be written as:

- Convective diffusion through the surrounding fluid as:

$$Flux_Z = K_{m,Z}.\left(C_{b,Z} - C_{o,Z}\right) \tag{4.22}$$

- Molecular diffusion through outer layer:

$$Flux_Z = \frac{D_Z \varepsilon \psi}{\delta_{OS}}\left(C_{o,Z} - C_{i,Z}\right) \tag{4.23}$$

- Solid-state diffusion through inner mackinawite film:

$$Flux_Z = A_Z \ln\left(\frac{C_{i,Z}}{C_{s,Z}}\right) \tag{4.24}$$

where C_b, C_o, C_i and C_s represent concentrations of different species in bulk solution, outer scale-solution interface, inner scale-film interface, and steel surface, respectively. Subscript Z denotes components H_2S, H^+ and CO_2. Under steady state condition, the three fluxes (Eqns. 4.22 – 4.24) of each single component are equal. By eliminating unknown interfacial concentrations from Eqns. (4.22) through (4.24), the flux of H_2S can be described as:

$$Flux_{H_2S} = A_{H_2S} \ln \frac{C_{b,H_2S} - Flux_{H_2S}\left(\frac{\delta_{0.5}}{D_{H_2S}\varepsilon\psi} + \frac{1}{K_{m,H_2S}}\right)}{C_{s,H_2S}} \tag{4.25a}$$

The flux of aqueous hydrogen sulfide in Eqn. (4.25) is related to the corrosion rate as:

$$CR_{H_2S} = Flux_{H_2S}.M_{Fe}/\rho_{Fe}, \tag{4.25b}$$

where M_{Fe} and ρ_{Fe} are molecular weight and density of iron, respectively.

Effect of pH: Solution pH has a critical impact on corrosion behavior. For instance, pH interferes with the formation of corrosion scale. High pH (greater than 5) is favorable condition for protective scale precipitation and ultimately corrosion rate reduction. At low H_2S concentration, pH significantly affects the corrosion rate. Although mackinawite layers form and control corrosion process due to direct reaction of dissolved H_2S with steel surface, the process is strongly driven by reduction of protons rather than the direct reaction. Proton transport rate (flux of proton) is controlled by convective diffusion, diffusion through the pores outer layer and solid-state diffusion through thin mackinawite layer. Fluxes of protons through the three layers are obtained from Eqns. (4.22 – 4.24). At steady state condition, the three fluxes of H^+ are equal and relate to the corrosion rate as: $CR_{H^+} = Flux_{H^+}.M_{Fe}/2\rho_{Fe}$. The flux of protons, which is controlled by mackinawite layer, is expressed as

$$Flux_{H^+} = A_{H^+} \ln \frac{C_{b,H^+} - Flux_{H^+}\left(\frac{\delta_{0.5}}{D_{H^+}\varepsilon\psi} + \frac{1}{K_{m,H^+}}\right)}{C_{s,H^+}} \tag{4.26}$$

Effect of CO_2 Concentration: In CO_2-H_2S corrosion, mass transfer mainly governs corrosion process. Hence, the contribution of CO_2 to the sour corrosion can be evaluated by applying similar approaches used in determining H_2S and H^+ effects on corrosion. Consequently, at steady state condition, the three fluxes of CO_2 must be

equal and related to CO_2 corrosion rate as: $CR_{CO_2} = Flux_{CO_2}.M_{Fe}/\rho_{Fe}$. Hence, the flux of CO_2 is given by:

$$Flux_{CO_2} = A_{CO_2} \ln \frac{C_{b,CO_2} - Flux_{CO_2}\left(\frac{\delta_{0.5}}{D_{CO_2}\varepsilon\psi} + \frac{1}{K_{m,CO_2}}\right)}{C_{s,CO_2}} \tag{4.27}$$

Unlike H_2S and H^+ contributions, the CO_2 contribution arises from the corrosive species generated from the hydration of CO_2. In this case, the CO_2 hydration reaction at steel surface becomes step-determining process. Therefore, CO_2 flux has to be equated to the limiting rate of hydration at steel surface.

$$Flux_{CO_2} = C_{s,CO_2}\left(D_{H_2CO_3}.\varepsilon.\psi.K_{hyd}^{f}.K_{hyd}\right)^{0.5} \tag{4.28}$$

By eliminating the unknown variable, C_{s,CO_2} from Eqns. (4.27) and (4.28), CO_2 flux can be expressed as:

$$Flux_{CO_2} = A_{CO_2} \ln \frac{C_{b,CO_2} - Flux_{CO_2}\left(\frac{\delta_{0.5}}{D_{CO_2}\varepsilon\psi} + \frac{1}{K_{m,CO_2}}\right)}{\frac{Flux_{CO_2}}{\left(D_{H_2CO_3}\varepsilon.\psi_{hyd}^{f}.K_{hyd}\right)^{0.5}}} \tag{4.29}$$

Effect of Corrosion Scale: In CO_2-H_2S corrosion, hydrogen sulfide is responsible for the formation of mackinawite layers. In addition, the aqueous H_2S contributes to the total corrosion rate. In this study, kinetics of layer formation is described using two mechanisms. The inner layer forms due to direct reaction of aqueous H_2S with steel whereas the outer layer forms because of continuous precipitation of corrosion products

resulting from cyclic process occurring in the inner layer. During the corrosion process, thickness of outer mackinawite layer changes with time. It is assumed that thickness of the layer depends on the balance between layer-formation and layer-damage rates, which can be expressed as:

$$SRR = SFR - SDR \tag{4.30}$$

where, SRR, SFR and SDR are sulfide retention rate, sulfide layer-formation rate and sulfide layer-damage rate, which all are in units of (mol/m^2.s). For typical pH range (4 < pH < 7), precipitation and dissolution of iron sulfide layer have major role; thus, Eqn. (4.30) can be written as:

$$SRR = CR - SDR_m \tag{4.31}$$

where SDR_m is measured sulfide layer mechanical damage rate. As proposed by Sun et al. (2008a), $SDR_m \approx 0.5CR$. Once the layer retention rate is determined, change in mass of the outer sulfide layer can be estimated as:

$$\Delta m_{os} = SRR \times M_{FeS} \times A_{sp} \times \Delta t \tag{4.32}$$

where M_{FeS} is molecular weight of iron sulfide in kg/mol and Δt is the time interval in seconds. A_{sp} is surface area of the steel in m^2**.** In Eqn. (4.29), mackinawite layer porosity and tortuosity factor are needed to compute flux of CO_2. Porosity of outer mackinawite layer is expected to be very high ($\varepsilon \approx 0.9$) and tortuosity factor (ψ) is estimated to be 0.003. Afterward, thickness of mackinawite layer is determined by:

$$\delta_{os} = \Delta m_{os} / \left(\rho_{FeS} \times A_{sp} \right) \tag{4.33}$$

Equations (4.25, 4.26 and 4.29) are nonlinear with respect to variable Flux_Z; therefore, solutions are obtained numerically (Fig. 4.3).

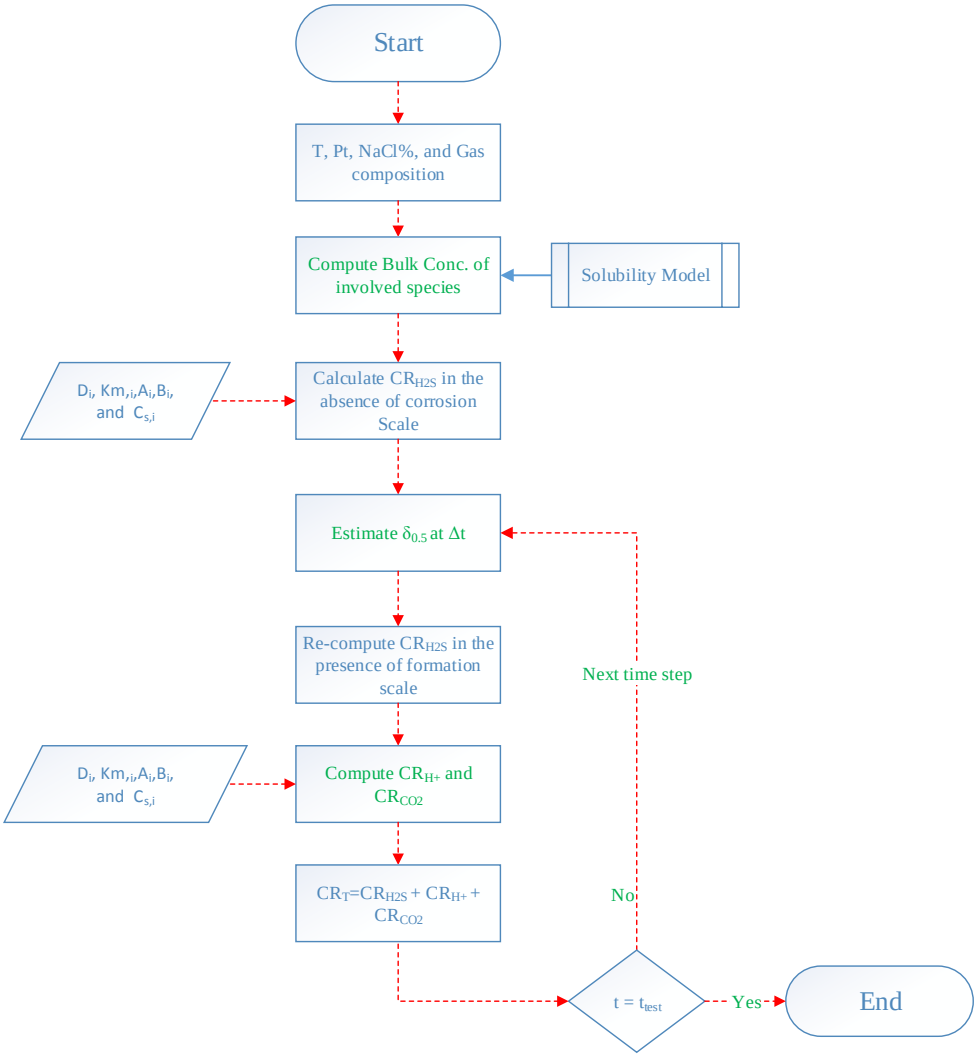

Figure 4.3 Computational flow chart for CO_2-H_2S corrosion model (MTB)

Chapter 5 : EXPERIMENTAL STUDY

The experimental study consists of i) Low pressure corrosion studies conducted at 0.83 MPa and varying temperature (26 to 80°C), salt content (1 and 2%), and gas phase CO_2 concentration (0 to 100%); and ii) high-pressure corrosion investigations performed varying temperature (37.78 -107°C), pressure (20.68 to 62.05 MPa), steel grade (T95, C110 and Q125), and CO_2 and H_2S concentrations.

5.1 Low Pressure Corrosion Study

In this study, two corrosion measurement techniques (weight loss and LPR) are employed to determine corrosion rate of tested materials. To identify CO_2 corrosion mechanism, instantaneous corrosion rate was monitored applying the linear polarization resistance method (LPR). Detailed test procedures and equipment descriptions are presented elsewhere (Elgaddafi et al. 2015).

5.1.1 Test Material

To measure the average corrosion rate, cylindrical test specimens were used. The specimens were solid rod with dimensions of 0.64 cm diameter and 10.16 cm length. They were cut from C1045 carbon steel. During the experiments, a specimen was partially (50%) immersed into the test solution. Typical chemical composition of C1045 carbon steel is presented in Table 5.1 (Azo materials, 2015). The test solution

was prepared by mixing deionized water with desired amount of sodium chloride. A graphite rod with length of 13.97 cm and diameter of 0.64 cm was used as a counter electrode. Temperature and pressure transmitters are installed on the autoclave to monitor and record test temperature and pressure. A test matrix of the experimental investigation is shown in Table 5.2.

Table 5.1 Chemical composition of Grade C1045 carbon steel (Azo materials, 2012)

Element	C	Fe	Mn	P	S
Content by weight (%)	0.420 - 0.50	98.51 - 98.98	0.60 - 0.90	≤ 0.040	≤ 0.050

Table 5.2 Test matrix for corrosion test

Temperature (°C)	Total pressure (MPa)	Salt Conc.	CO_2 partial pressure (MPa)					Exposure time (h)	Flow condition
26	0.83	1% and 2% NaCl	0*	0.21	0.41	0.62	0.83	187	Stagnant
43			0*	0.21	0.41	0.62	0.83		
60			0*	0.21	0.41	0.62	0.83		
80			0*	0.21	0.41	0.62	0.83		

*These tests were performed with pure nitrogen at 0.83 MPa

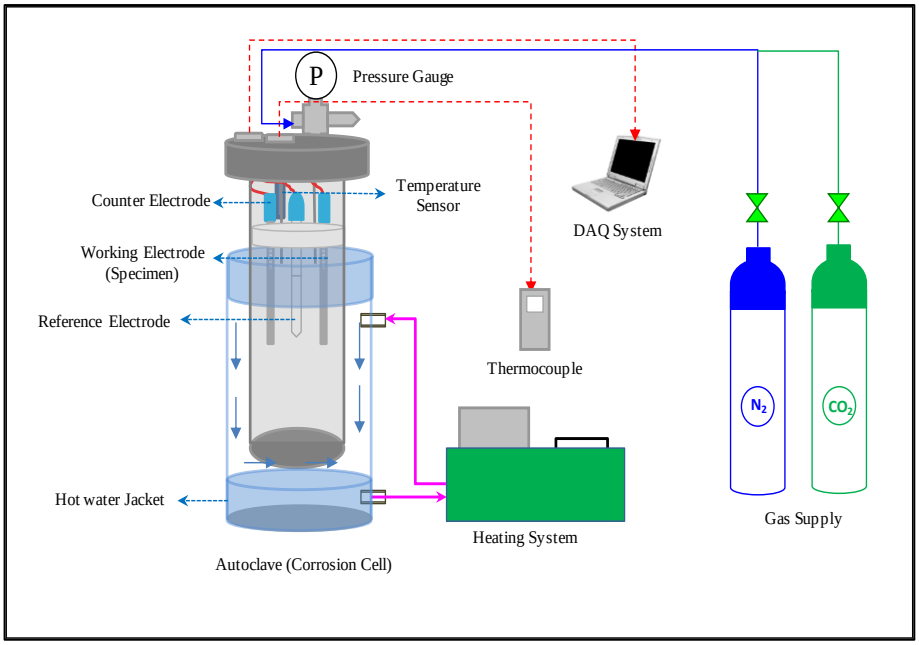

Figure 5.1 Schematic of low-pressure corrosion test setup (Elgaddafi et al. 2015)

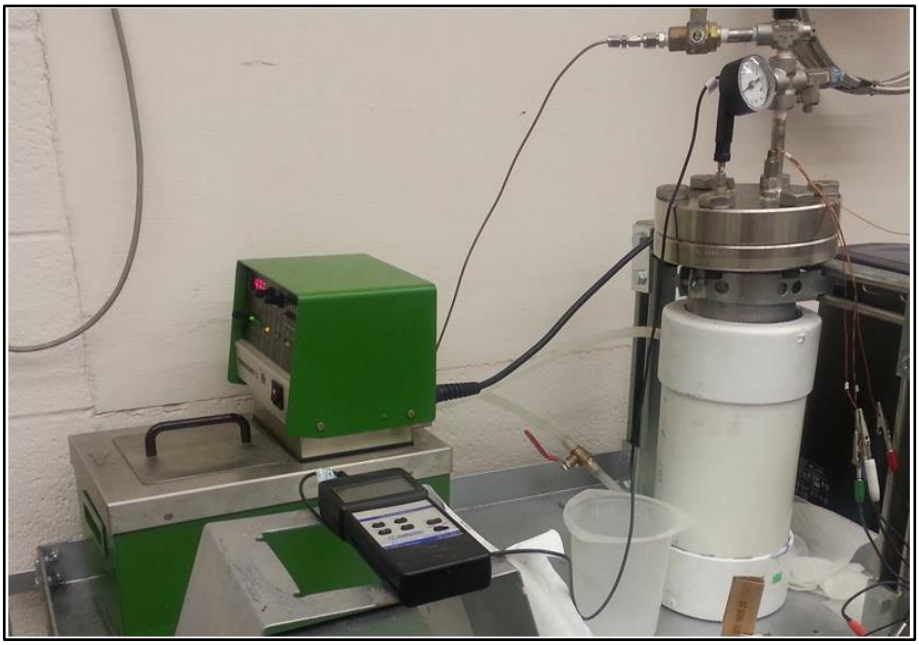

Figure 5.2 Low-pressure corrosion test apparatus (Naidu 2014)

5.1.2 Experimental Apparatus

The test facility was designed to carry out corrosion experiments under moderate pressure and temperature. All corrosion experiments were conducted under stagnant condition. A schematic of the experimental setup is shown in Fig. 5.1. The test apparatus consists of: i) corrosion cell (2-liter autoclave) with 8.9 cm diameter and 33 cm length; ii) circulating bath; iii) LPR system (Gamry G300 Potentiostat); iv) data acquisition system (DAS);

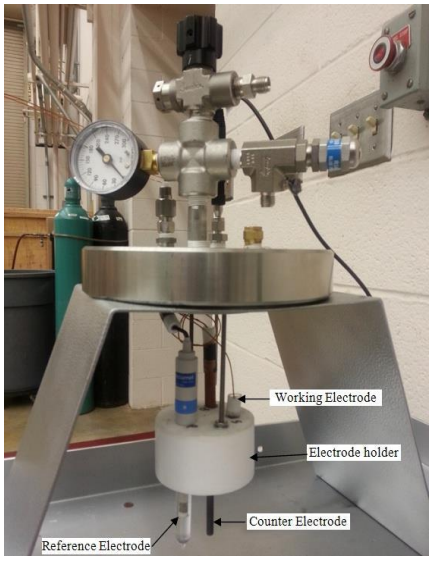

Figure 5.3 Autoclave lid with cylindrical PTFE block (Elgaddafi et al. 2015)

and v) carbon dioxide and nitrogen supply cylinders. The cell is jacketed and mounted on a supporting frame, as shown in Fig. 5.2. To maintain the test temperature at desired level, heating fluid (Glycol fluid) was circulated through the jacket. A recirculation bath was used to control test temperature. The corrosion cell consists of three electrodes (Fig. 5.3): i) working electrode (specimen), ii) Ag/AgCl reference electrode, and iii) counter electrode (graphite). The three electrodes are wired to the LPR system, which is installed on data acquisition computer.

5.1.3 Experimental Procedure

A reliable test procedure was developed during this study and consistently used to determine the influence of temperature, CO_2 concentration and salt content on corrosion of carbon steel. The test procedure is summarized into six major steps:

1. **Specimen Preparation and Weight Measurement**: A test specimen was cut and machined from 1045 medium carbon steel rod. The surface of the specimen was polished using medium grade brush and cleaned with deionized water, and dried. Then, initial specimen weight was measured. To eliminate atmospheric corrosion, the test specimen was immediately inserted into the copper sleeve, connected to the LPR system and installed on the PTFE block
2. **Electrode Preparation**: After each experiment, the counter electrode was removed, cleaned and reinstalled. The reference electrode was disassembled, examined, calibrated, filled with KCl to the marked level and reassembled.
3. **Continuity Test**: After the three electrodes were wired and installed on the PTFE block, they were checked for continuity using a multi meter to ensure the

signals transfer from the electrodes to the LPR leads and to avoid any short circuit between the electrodes and autoclave lid.

4. **Test Fluid Preparation**: 1 L of sodium chloride solution was prepared for corrosion experiment. Afterward, 75% of the autoclave was filled with the test solution. Subsequently, the lid of autoclave was assembled and tightened to prevent gas leak. In order to reduce dissolved oxygen content, the solution was purged with nitrogen for 5 to 15 min at 26°C.
5. **Pressurizing the system:** After purging, nitrogen gas was released from the autoclave. Afterward, the system was heated to the desired temperature and dry CO_2 and N_2 were injected into the autoclave, maintaining desired partial pressures of CO_2 and N_2.
6. **Instantaneous Corrosion Rate Measurement (LPR):** Following the injection of gas into the autoclave, corrosion test was started. Instantaneous corrosion rate was measured using LPR system. LPR measurements were performed in a range of ± 5 mV with respect to the open circuit potential (OCP) and at scan rate of 0.125 mV/s. Other variables such as exposed area and equivalent weight of the specimen were entered into the LPR system software (DC-105) for initiation of the measurement. The corrosion test was carried out for 187 h. The software recorded polarization resistance (Rp), which is related to corrosion current density (i_{Corr}) according to the following formula:

$$i_{corr} = \frac{\beta}{R_p} = \frac{\beta_a \times \beta_c}{2.303 \times R_p \times (\beta_a + \beta_c)} \quad (5.1)$$

where β_a and β_c are anodic and cathodic Tafel constant; and R_p is linear polarization resistance. β is a constant with a value of 120 mV/decade. Subsequently, instantaneous corrosion calculated from LPR is a function of corrosion current density (i_{corr}):

$$\text{Corrosion rate} = \frac{0.00327 \times i_{corr} \times EW}{\rho_{st}} \quad (5.2)$$

where i_{corr} is corrosion current density in mA/cm^2. ρ_{st} is density of steel in g/cm^3. EW is equivalent weight in grams.

7. **Specimen Cleaning and Final Weight Measurement:** After 187 h of exposure time for each test, the autoclave was de-pressurized gradually and the specimen was carefully removed from the copper holder. The tested specimen then was cleaned with de-ionized water in order to remove any type of corrosion scale deposited on specimen surface and gently polished using a paper towel, and dried. The final weight of tested specimen was measured after drying. Finally, average corrosion rate (mm/y) was calculated based on weight loss measurement approach, as following:

$$\text{Corrosion rate} = \frac{11.14 \times (W_1 - W_2)}{A \times t} \quad (5.3)$$

where W_1 and W_2 are the initial and final weight in grams, respectively. A is the exposed area in cm^2 and t is the exposure time in hour.

5.2 High-Pressure Corrosion Investigation

This investigation is aimed to determine the influence of various variables such as pressure, CO_2 and H_2S concentrations, temperature, type of material, and fluid flow condition on the corrosion of common oil field tubulars. Salt concentration was maintained at 2% NaCl. A test facility was built to carry out corrosion experiments at HPHT condition. Elgaddafi et al. (2016b) presented details of experimental procedures and apparatus used in this investigation.

5.2.1 Test Material and Preparation

Test specimens of flat coupons with 2-mm thickness were cut from API grades carbon steels (T95, C110, and Q125). Hydraulic water-jet machining techniques were used to manufacture the specimens with high degree of precision, with smooth surface and without material defect. Test specimens were designed in accordance with the ASTM standard (ASTM E8M-98, 2009) to function as uniform corrosion and tensile strength specimens (Fig. 5.4a). The middle narrow portion of the specimens was utilized to measure corrosion rate (CR) and loading carry capacity (LCC). To prevent galvanic corrosion and accurately measure corrosion rate, the specimens were covered with silicon-based corrosion protective coating except the front side (Fig. 5.4b) of the narrow section (exposure area of 1.92 cm^2). Chemical compositions of materials used in this study are presented in Table 5.3.

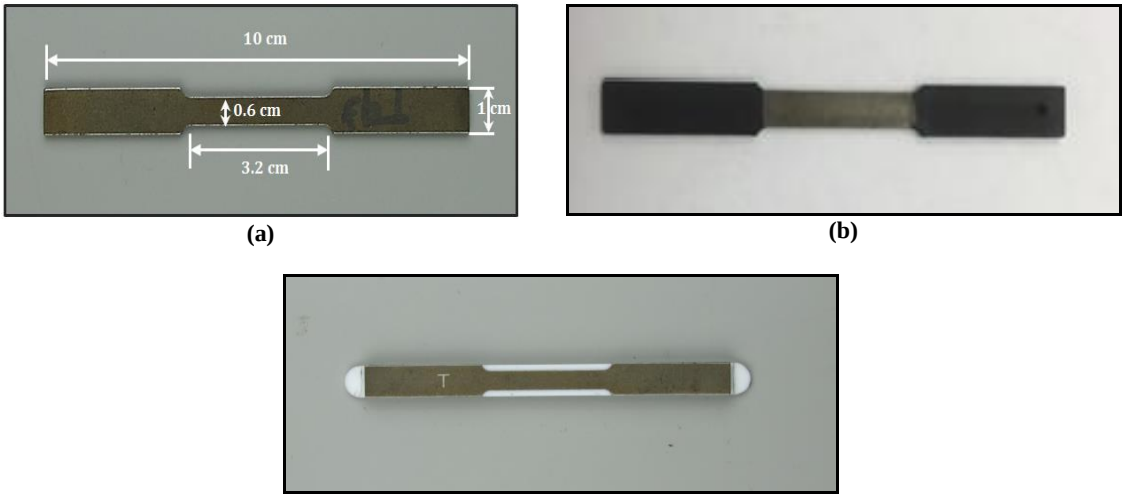

Figure 5.4 Test specimen: a) Design; b) covered with protective coating; and C) Specimen with holder (Elgaddafi et al. 2016b)

Table 5.3 Chemical compositions of API carbon steels used in this study

Elements (wt %)		C	Mn	P	S	Si	Cu	Ni	Cr	Mo	Fe
T95	Min	-	-		-	-	-	-	-	-	-
	Max	0.33	0.34	0.009	0.001	0.27	0.02	0.03	1.01	0.79	balanced
C110	Min	-	-		-	-	-	-	-	-	-
	Max	0.30	0.47	0.007	0.001	0.23	0.01	0.01	1.01	0.78	balanced
Q125	Min	-	-		-	-	-	-	-	-	-
	Max	0.26	0.49	0.012	0.001	0.21	0.03	0.04	0.91	0.26	balanced

During stagnant corrosion experiments, test specimens were attached to a coupon holder (Fig. 5.5a), which is made of Teflon sleeve. After the specimens were covered with protective coating, they assembled with the holder (Fig. 5.5c) and mounted in vertical orientation on the Teflon sleeve. In order to be consistence with dynamic experiments, stationary cylinder made of PTEF material was placed inside the Teflon sleeve. Afterward, two Teflon bushings were used to keep the specimens in place as shown in Fig. 5.5b.

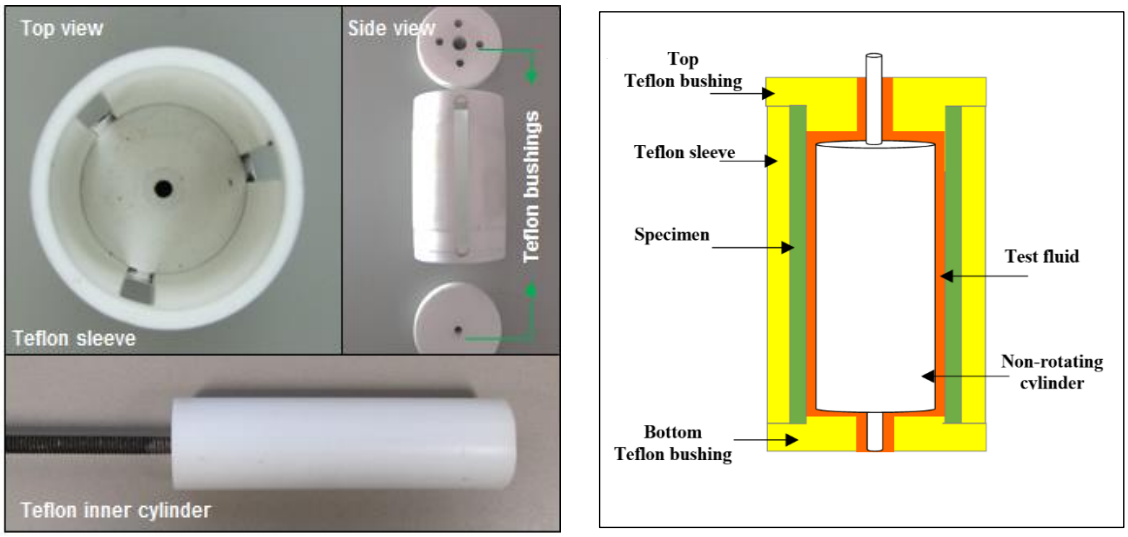

(a) **(b)**

Figure 5.5 Test specimen holder for stagnant corrosion experiments: a) photo; and b) holder with two specimens and non-rotating cylinder

For dynamic corrosion experiment, instead of stationary PTFE cylinder, a rotating cylinder (inner cylinder) made of stainless steel was connected to a motor with speed controlling capability (Fig. 5.6a). The wall shear stress in a Couette flow is a function of fluid properties, rotational speed, and diameters of inner and outer cylinders. Like the static test, specimens were mounted on the holder. Then, inner cylinder and, top and bottom bushings were assembled with Teflon sleeve (outer cylinder) to keep the specimens in place (Fig. 5.6b).

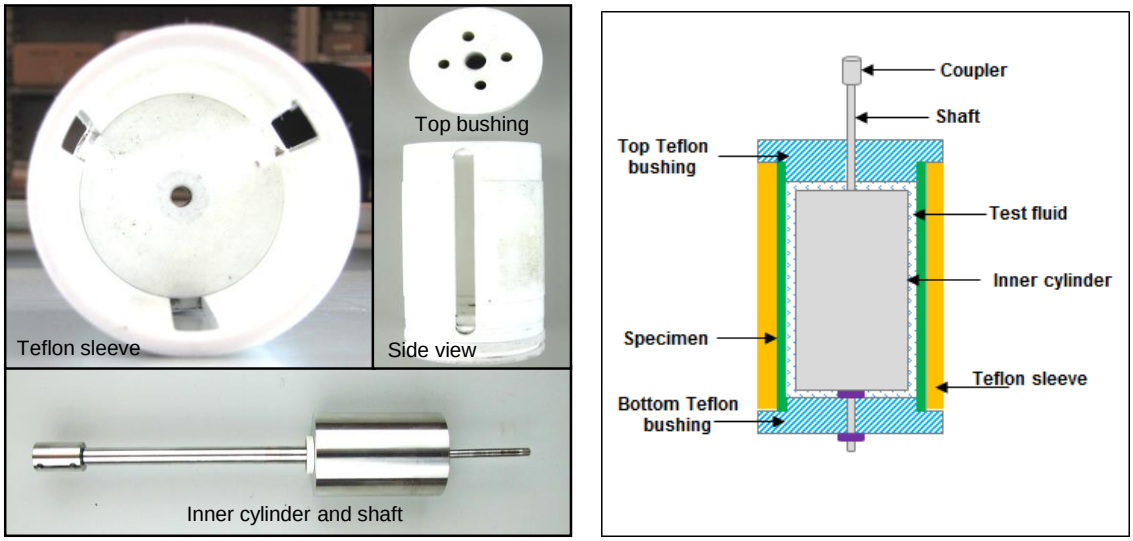

(a) **(b)**

Figure 5.6 Test specimen holder for dynamic corrosion experiments: a) photo; and b) holder with two specimens and inner cylinder

5.2.2 Experimental Setup

The schematic of test setup is displayed in Fig. 5.7. The setup consists of: i) high-pressure high-temperature (HPHT) autoclave (corrosion cell); ii) dynamic rotating system consists of: air motor; magnetic coupler; and cylindrical shaft and speed gauge; iii) gas supply system consists of four cylinders of CO_2, H_2S, CH_4 and N_2; iv) injection system to control gas composition and boost supply gas pressure; v) heating system to precisely control test temperature; vi) measurement and instrumentation system (sensors and transmitters) to measure and record relevant test parameters; and vii) data acquisition and control system. The internal face of the autoclave, which has capacity of 2364 cm^3 (D=8.9 cm and L = 38 cm) is made of Hastelloy C-276 to prevent corrosion. It is installed inside a heating jacket to maintain constant temperature during experiment (Fig. 5.8). The jacket is fully covered with insulation to minimize heat loss. Heating

system consists of a heater, fluid reservoir, heating fluid (synthetic oil), circulating pump, pipelines covered with insulation to minimize heat lose, and valves to control the circulated fluid. Autoclave temperature was maintained constant by circulating synthetic-based heating fluid in the jacket. Before the test, covered specimens, specimen holder, non-rotating or rotating cylinder and Teflon bushings were assembled as shown in Fig. 5.6b, and the assembly was placed inside the autoclave.

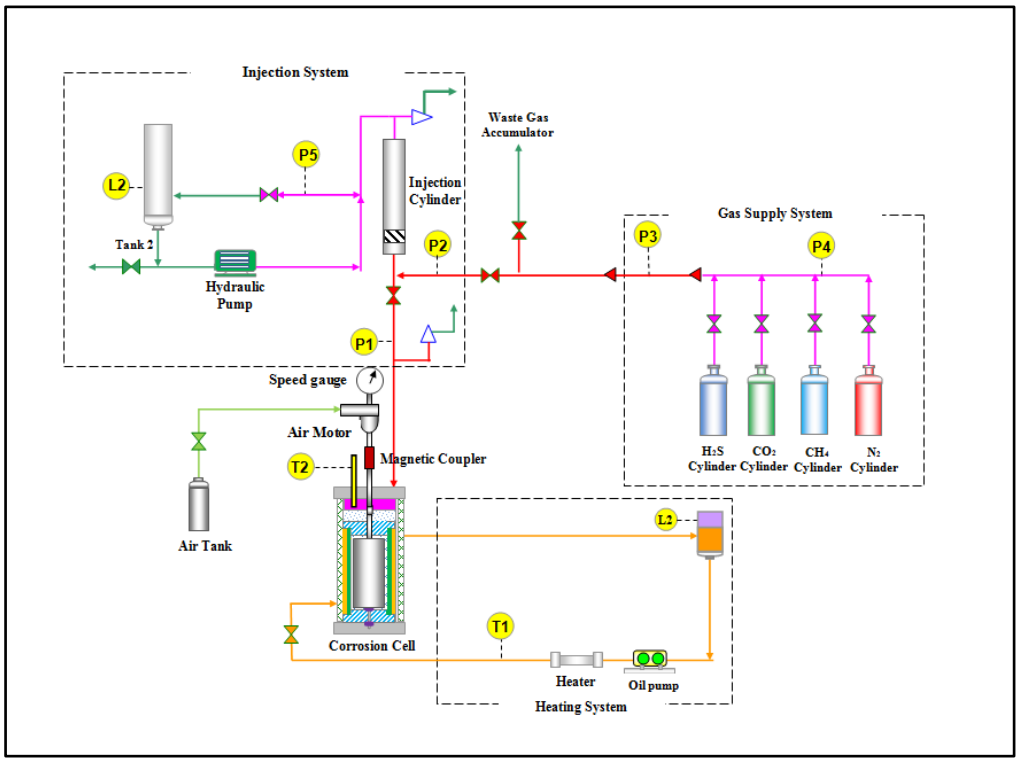

Figure 5.7 Schematic of high-pressure experimental setup

The maximum pressure that can be supplied from the gas cylinders was approximately 17 MPa. Therefore, a gas injection system was used to boost the supply pressure to a desired level and accurately control composition of mixed gas (methane, hydrogen sulfide and carbon dioxide) in the autoclave. Two temperature transducers are installed to monitor autoclave (T_1) and heating fluid (T_2) temperature. A pressure

transducer (P_1) is mounted on the autoclave to measure total pressure. The test variables for this investigation are shown in Table 5.4.

Table 5.4 Test variables for corrosion test at HPHT

Grade	Salt Conc. (%)	Total pressure (MPa)	Temp. (°C)	Gas composition			Flow status (rpm)	Exposure time (Days)
				CO_2 (%)	H_2S (ppm)	CH_4 (%)		
T95	2	20.68	37.78	0 - 100	0 - 150	0-100	0 - 1000	7
C110		41.37	71.11					
Q125		62.05	107.00					

5.2.3 Test Procedure

The experimental procedure for high-pressure corrosion experiment is consists of the following steps:

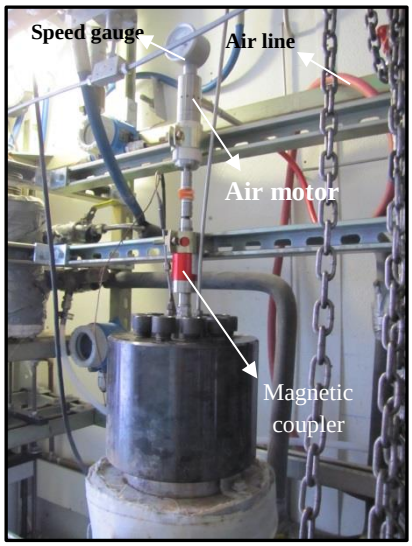

Figure 5.8 Corrosion cell

1. **Preparation of test specimen:** In high-pressure study, two or three identical specimens were employed to obtained average corrosion rate measurement. The specimen preparation was conducted in accordance with ASTM standard (ASTM G 111-97). Firstly, the specimens were cleaned with deionized water, dried in the air, punch marked with numbers and their initial weights were measured. Then, they were painted with high-temperature coating except the front part of the narrow section. Then, the unpainted area was cleaned with Methyl Ethyl Ketone in accordance with ASTM standard. After they were cleaned, immediately

attached to the specimen holder and inner cylinder and bushings were assembled as displayed in Fig. 5.6b.

2. **Test fluid preparation (electrolyte):** Test solution (2% NaCl) was prepared by using deionized water. During the experiment, the autoclave filled up with 950 ml of test solution and heated steadily to the desired temperature by circulating heating fluid. To remove oxygen, the solution was purged with nitrogen for 30 minutes by pressurizing the autoclave up to 10.34 MPa. Then, the holder assembly with specimens was inserted into the autoclave.
3. **Gases injection and test implementation:** Once the purging process was accomplished, nitrogen gas was gradually vented from the autoclave. Subsequently, testing gases consisting of carbon dioxide, hydrogen sulfide and methane were injected into the autoclave as required. When the desired gas composition and total test pressure were attained, the autoclave was fully closed, and temperature and pressure were maintained constant for 7 days.
4. **Depressurizing of the autoclave:** when the test was completed, inner cylinder was stopped (for only dynamic test) and the autoclave was de-pressurized. Then, the autoclave was opened and the specimen holder was carefully removed, and the specimens were recovered. Optical micrographs of specimens were obtained immediately after they were recovered from the autoclave. Microscopic image of each specimen was taken at a selected spot, which represents corroded area of the specimen.

5. **Specimen cleaning and weight measurement:** After the surface analysis, corrosion scale deposits were removed by washing the specimens with clean water and scrubbing it gently using a paper towel. Then, the specimens were soaked in a paint remover (Methyl Ethyl Ketone) and rinsed with alcohol and water to remove the coating. After drying, the final weight of each specimen was measured. The average corrosion rate was obtained from the weight loss (Eq. 5.3). Finally, the specimens were placed in sealed vials for further investigations (Tensile strength test).

5.3 Tensile Strength Test (TST)

To assess the effect of uniform corrosion as well as localized corrosion on the mechanical properties, TST tests were carried out prior and after performing corrosion experiment. Elgaddafi et al. (2016b) presented details of experimental procedures and apparatus used to carried out tensile strength test.

Chapter 6 : RESULTS AND DISCUSSION

During the course of this study, extensive experiments were conducted and corrosion and tensile strength measurements were gathered. In this chapter, these measurements are thoroughly presented and extensively discussed.

6.1 Low-Pressure Corrosion Measurements

6.1.1 Instantaneous Corrosion Rate

During low-pressure corrosion experiments, liner polarization resistance (LPR) method was employed to measure the instantaneous corrosion rate. Figure 6.1 displays LPR measurement (corrosion rate vs. time) obtained at 80°C and various CO_2 partial pressures. At the beginning of the test, the corrosion rate increased reaching its maximum value at about 10 hrs. Subsequently, a rapid decrease in corrosion rate was observed, gradually reaching steady state condition at the end of the test (approximately after 176 h of exposure). The maximum instantaneous corrosion rate observed at the beginning of the experiment was dependent on CO_2 partial pressure. The peak corrosion rate increased with CO_2 partial pressure. The peak rate occurred due to contributions of different phenomena. This observation is attributed to formation of iron carbide scale. As corrosion process progresses, first, iron carbide (Fe_3C) scale forms on steel surface.

Iron carbide is strong electrical conductor, which can accelerate corrosion because of galvanic effect between steel substrate and Fe_3C layer (Crolet et al. 1998; Choi et al. 2013). Subsequently, a decline in corrosion rate occurs due to formation of

iron carbonate ($FeCO_3$) scale, which is caused by increase in iron and carbonate ion concentrations near steel surface. Moreover, the increase in corrosion rate with CO_2 partial pressure is due to increase in H_2CO_3 concentration in the solution, which accelerates the cathodic reaction. The trend of instantaneous corrosion rate with CO_2 partial pressure is consistent with results of previous studies (Suhor et al. 2012; Zhang et al. 2013b; Choi et al. 2013).

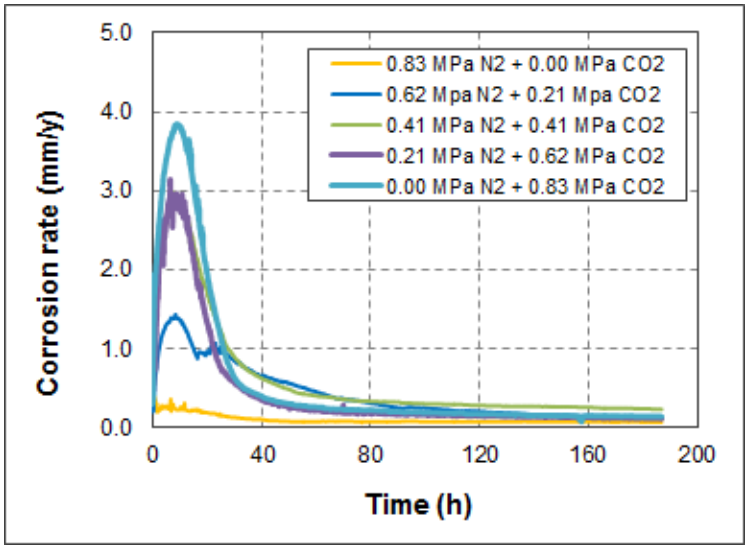

Figure 6.1 Instantaneous corrosion rate measurements at 0.83 MPa, different CO_2 partial pressures, 2% NaCl solution and 80°C

Figure 6.2 compares instantaneous corrosion rate obtained from LPR with average corrosion rate from weight loss measurement at various CO_2 partial pressures. As depicted from the figure, both techniques showed comparable results under steady state condition (test time exceeding 80 h). However, at the beginning of experiment, LPR measurements demonstrated higher corrosion rate, which is approximately 3.05 mm/y. After one day of exposure, LPR corrosion rates decreased approaching zero asymptotically.

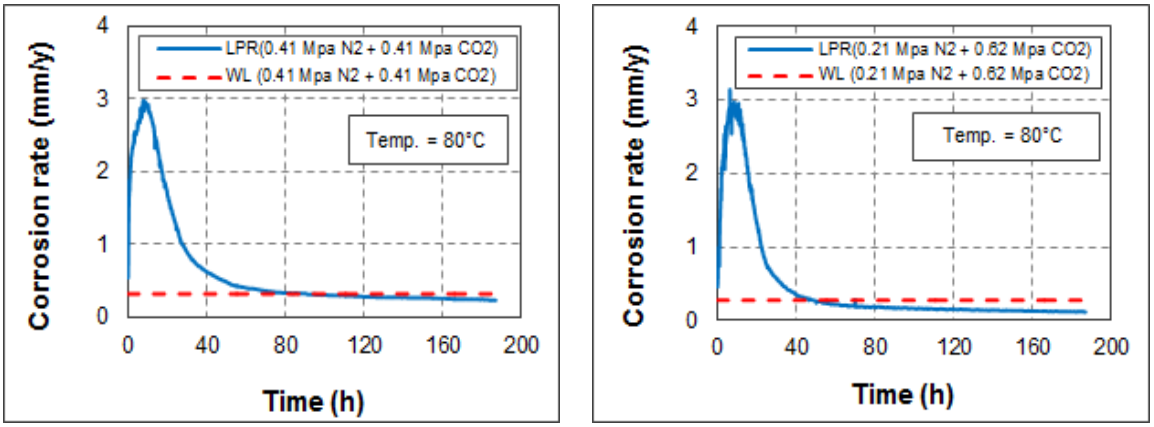

(a) (b)

Figure 6.2 Instantaneous corrosion rate (LPR) and average corrosion rate (WL) at various CO_2 partial pressures (2% NaCl solution): a) P_{CO2} = 0.41 MPa; and b) P_{CO2} = 0.62 MPa

6.1.2 Comparison of WL and LPR Measurements

It is well known that LPR technique involves analysis of complex electrochemical process based on polarization resistance measurements. Regularly, it contains a number of calibration techniques to obtain reasonable measurements. Therefore, weight loss measurements are compared with average LPR data obtained in 187 hours (Fig. 6.3).

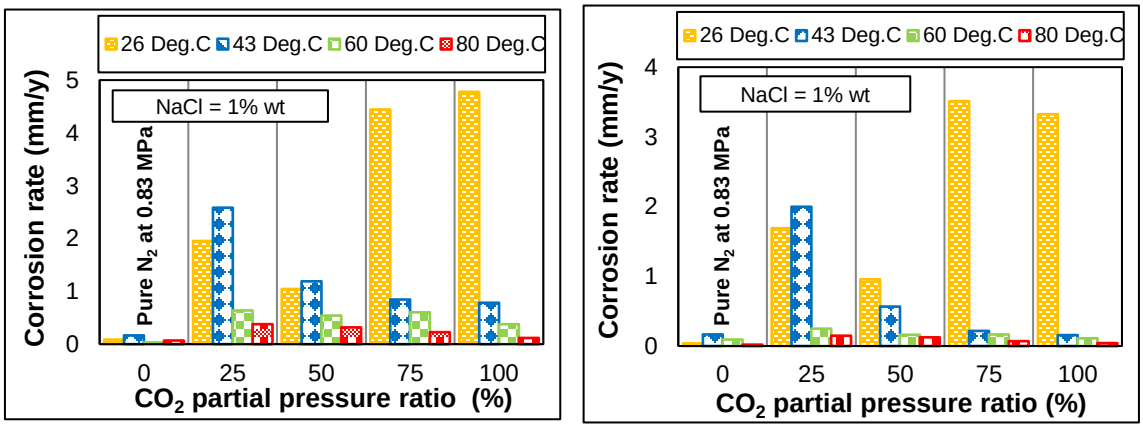

(a) (b)

Figure 6.3 Average corrosion rate vs. PPR at different temperatures (1% NaCl solution): a) weight loss and b) LPR

Even though very high instantaneous corrosion rate was observed during the first two days of the test, the overall average corrosion rate is comparable with weight loss measurement. Results show satisfactory agreement between the LPR and WL methods. Very similar corrosion rate trends were observed at different CO_2 partial pressures. In some cases, discrepancies exist between LPR and WL measurements due to calibration challenge with LPR instrument.

6.1.3 Effect CO_2 Partial Pressure Ratio (PPR)

Figure 6.4 demonstrates impact of PPR on corrosion rate at different temperatures (26, 43, 60 and 80°C). For specimens tested at low-temperature (26°C), the results display gradually decaying growth in corrosion rate with PPR. Minor change was observed when PPR exceeded 50%. One possible explanation for this trend could be improvement of cathodic reaction due to the increase in carbonic acid concentration in the liquid phase. This observation is in agreement with results of other studies (Cui et al. 2004; Nesic 2007; Choi and Nesic 2011; Jia et al. 2012; Choi et al. 2014). At relatively low PPR (below 50%). A similar corrosion rate trend with PPR was observed at intermediate temperatures (between 43 and 60°C) wherein corrosion rate increased with PPR (Figs. 6.4b and 6.4c); however, it decreased with PPR when PPR > 75%. Wen-fei et al. (2012) have attributed the corrosion rate improvement to change in corrosion scale characteristics. They observed transformation of compact fine-grain scale into bulky-grain scale with PPR, accelerating the corrosion. Furthermore, as PPR increased further, decline in corrosion rate was caused by the formation of more

condensed corrosion scale of $FeCO_3$ (Hernandez, et al. 2012). Nesic (2007) experienced this behavior and provided possible explanation. Accordingly, the increase in PPR results in increase in concentrations of H_2CO_3 and, Fe^{2+} and CO_3^{2-}, causing super-saturation near the steel surface, which is necessary for the formation of protective scale that decreases corrosion rate. The decline in corrosion rate with CO_2 content at high PPR is consistent with previous studies (Sun and Nesic 2004; Seiersten 2001). At high temperature (80°C), the trend is slightly different. Remarkable increase in corrosion rate was observed with CO_2 concentration at low PPR (less than 25%). Nevertheless, with further increase in PPR (above 25%), slight variation in corrosion rate was observed. This observation is consistent with previous findings of Jepson and Bhongale (1995).

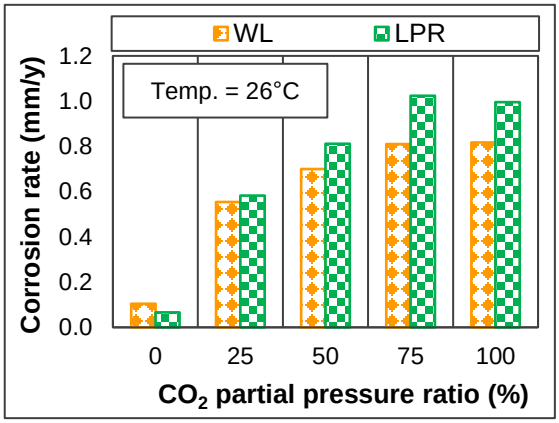

(a)

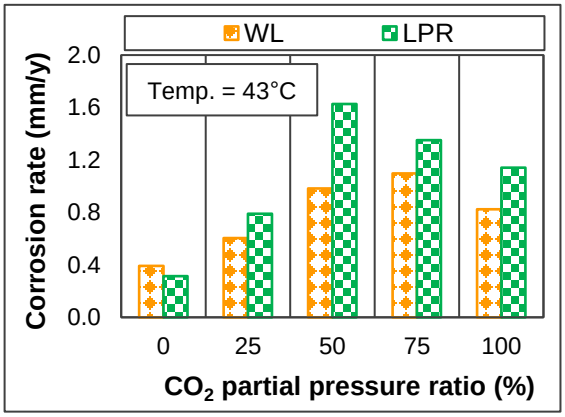

(b)

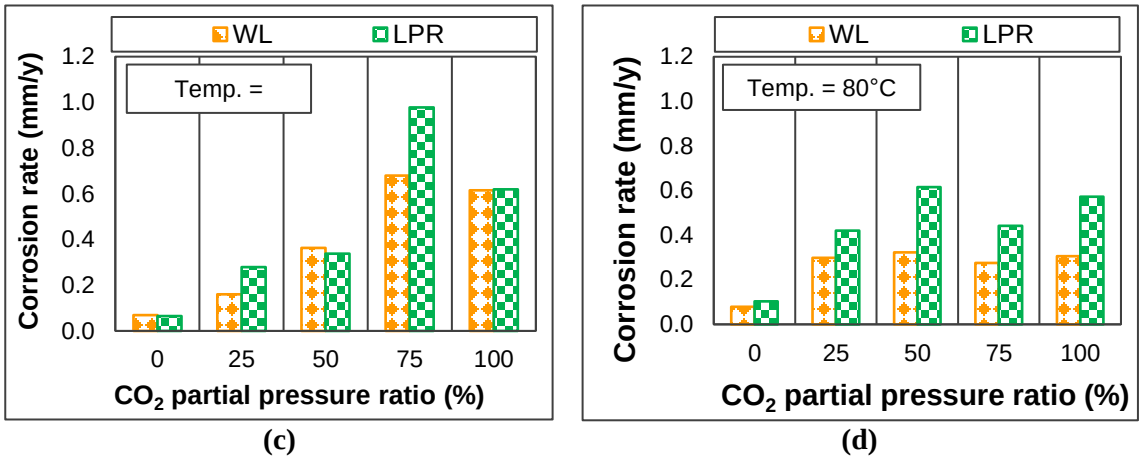

Figure 6.4 Average corrosion rate measurements for 178 h versus PPR at different temperatures (2% NaCl solution): a) 26°C; b) 43°C; c) 60°C; and d) 80°C

6.1.4 Effect Temperature

Temperature is one of the most significant environmental parameters that influence corrosion of carbon steel. Figure 6.5 shows average corrosion rate (measured using weight-loss technique) of test specimen exposed to 2% NaCl solution at various temperatures and PPRs. Corrosion rate was increased when temperature was increased from 26 to 43°C. Low temperature reduces the possibility of scale formation; consequently, corrosion exacerbates as temperature increases (Forero et al. 2013).

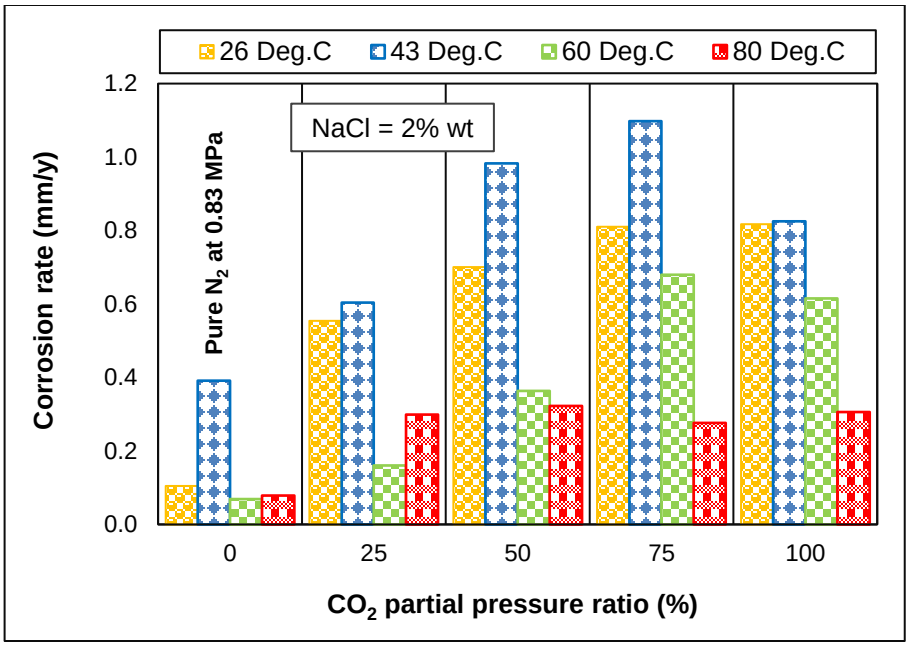

Figure 6.5 Effect of temperature on corrosion rate at various PPR in 2% NaCl solution

As temperature increased above 43°C, corrosion rate remarkably decreased with temperature regardless of the PPR. The decline in corrosion rate at high temperature (above 43°C) could be attributed to the influence of temperature on physical phenomena involved in corrosion process including CO_2 solubility, H_2CO_3 ionization, electrochemical reactions, and corrosion scale. These observations are consistent with previous investigations (Seiersten 2001; Yin et al. 2009; Xiang et al. 2013; and Li et al. 2013a). In this study, the maximum corrosion rate was observed at 43°C (critical temperature). This observation has been found in accordance with previous studies (Yin et al. 2009; Li et al. 2013a) conducted under similar condition. However, in studies carried out at low CO_2 partial pressure (Ikeda et al 1984; Ikeda et al 1985; Dugstad 1995; Zhao et al 2000), the critical temperature was approximately at 85°C. The critical temperature can be affected with other test parameters such as pressure, salt

concentration and CO_2 partial pressure, and material type. In pure nitrogen saturated brine (absence of CO_2), corrosion rate was extremely low and comparable except at 43°C. Previous investigators (Hernandez et al. 2012) reported similar results.

Since temperature affects most of the phenomena associated with corrosion process, its impact on corrosion is complex and not fully understood. Increase in temperature can accelerate electrochemical reactions and transport of species (molecular diffusion); hence, it intensifies corrosion. In contrast, high temperature tends to increase precipitation rate of corrosion product and assists formation of protective scale, resulting in reduction of corrosion. For instance, in pure CO_2 saturated brine, iron carbonate ($FeCO_3$) precipitates on metal surface after its solubility limit is reached. Corrosion product in CO_2 saturated environment ($FeCO_3$) is extremely sensitive to the temperature (Johnson and Tomson 1991). Moreover, at temperature below 149°C, CO_2 solubility declines with temperature leading to reduction in carbonic acid concentration and increase in pH, which has adverse effect on corrosion process.

Predominantly, severity of CO_2 corrosion is higher at low-temperature than at high-temperature due to the absence of corrosion product (Valdes et al. 1998). Figure 6.3 show the effect of temperature on corrosion rate of carbon steel exposed to 1% NaCl solution at different PPR. As displayed from the figure, the maximum corrosion rate, which is observed at 43°C, is not only temperature-dependent but also PPR.

6.2 High-Pressure Corrosion Measurements

In this study, specimens used for corrosion tests were utilized to measure material strengths after exposure to corrosive environment. Results of mechanical strength tests are presented in Section 6.3.

6.2.1 Effect CO_2 Partial Pressure Ratio

T95 Carbon Steel

Figure 6.6 presents average corrosion rate of T95 carbon steel in brine solution saturated with mixed gas containing methane and CO_2. The corrosion rate values displayed in the figure represents the average of two test specimens. The experiments were carried out at 40.37 MPa and 38°C under static condition varying CO_2 partial pressure ratio (PPR) from 0 to 100%. T95 exhibited relatively high corrosion rate in pure methane saturated environment approximately 10 mm/y, which is attributed to the absence of protective corrosion scale (Fig. 6.8a). As PPR increased from 0 to 25%, the corrosion rate doubled. This is expected because existence of carbon dioxide creates corrosive environment containing carbonic acid and lowers solution pH, resulting in higher corrosion rate. Above 25% PPR, the corrosion rate gradually increased with PPR. There are two possible explanations for the increase in corrosion rate with PPR. First, dissolved amount of carbon dioxide exponentially increases with PPR, which in its turn hydrates and raises H_2CO_3 concentration in the brine and ultimately corrosion rate. The other possible reason is attributed to the formation of non-protective scale that partially covers the test specimen surface (Fig. 6.7). Therefore, corrosion continues in the uncovered portion of specimen.

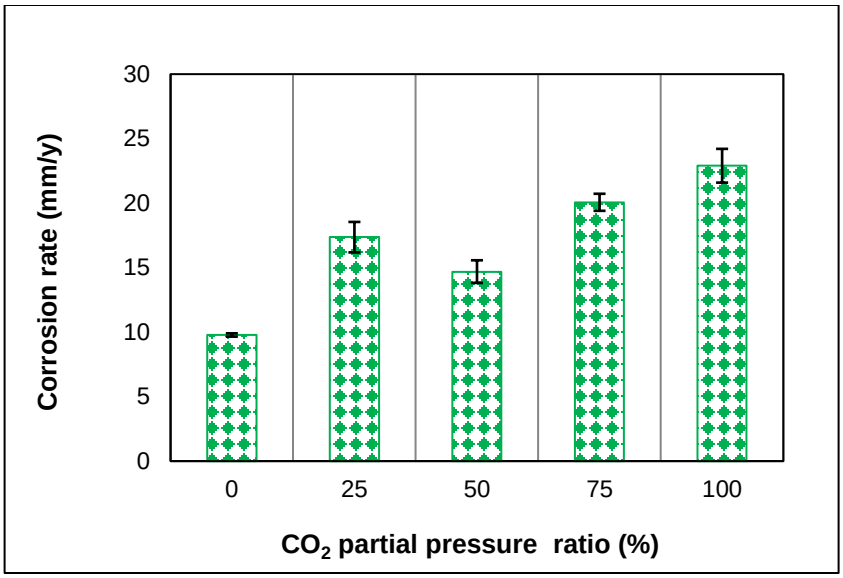

Figure 6.6 Average corrosion rate of T95 grade steel vs. PPR at 41.37 MPa

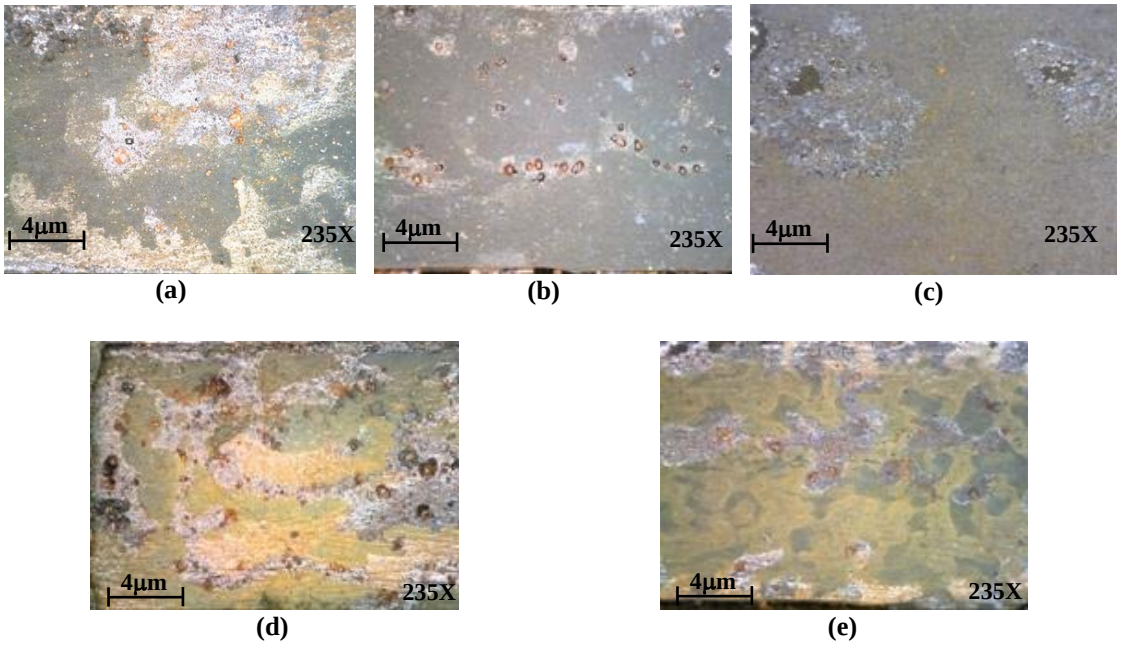

Figure 6.7 Optical micrographs of T95 specimens tested at 41.37 MPa and various CPPR: a) 0%; b) 25%; c) 50%; d) 75%; and e) 100%

C110 Carbon Steel

Figure 6.8 presents corrosion rate of C110 carbon steel in NaCl solution saturated with mixed gas containing methane and CO_2 at different total pressure (20.68, 41.37, and 62.05 MPa). For corrosion measurement at 20.68 MPa (Fig. 6.8a), Corrosion rate predominantly increased as PPR was increased, resulting from improved dissolution of CO_2 in brine, which raised carbonic acid concentration and consequently reduced solution pH. A number of studies (Honarvar Nazari et al. 2010; Choi and Nesic 2011; Zhang et al. 2011) reported exacerbation of corrosion with acid concentration. Increasing acid concentration often accelerates cathodic reactions and promotes corrosion. Measured corrosion rate increased approximately tenfold with the injection of 100% CO_2. The highest corrosion rate (14.21 mm/y) was observed at 100% PPR. Corrosion rate trend with respect to PPR is predominantly consistent with findings of previous studies (Choi and Nesic 2011; Huang et al. 2014; Schmitt and Horstemeier 2006).

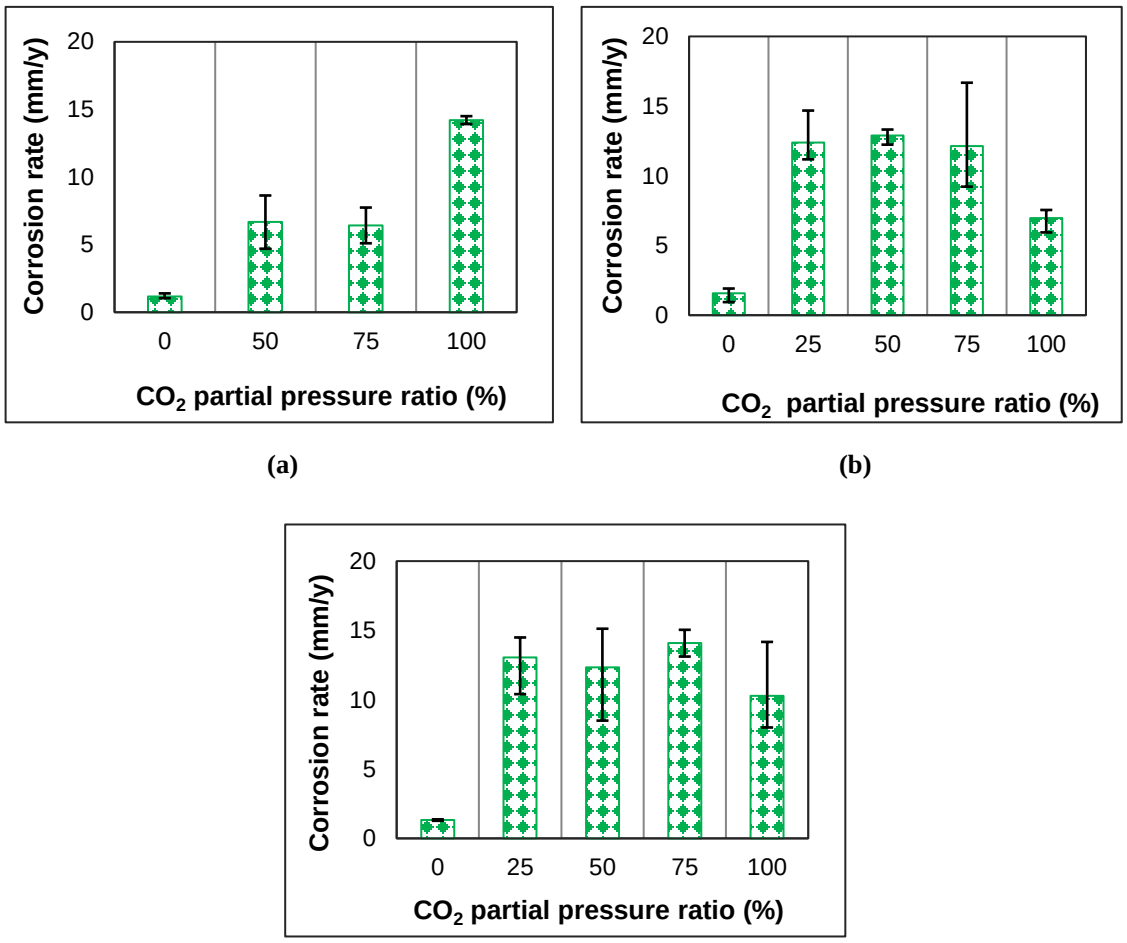

Figure 6.8 Average corrosion rate of C110 grade steel vs. PPR at different total pressures: a) 20.68 MPa; b) 41.37 MPa; and 62.05 MPa

Figure 6.9 shows surface morphology of C110 specimens corroded at 20.68 MPa and 38°C varying PPR. A micrograph of uncorroded specimen (Fig. 6.9a) is presented for comparison purposes. As depicted from the figure, non-protective layer was formed on specimen surface. Microscopic examinations were conducted on specimen surface before and after removing corrosion protective layer. The

examination did not indicate presence of localized corrosion. Only uniform corrosion was visually observed in all the specimens.

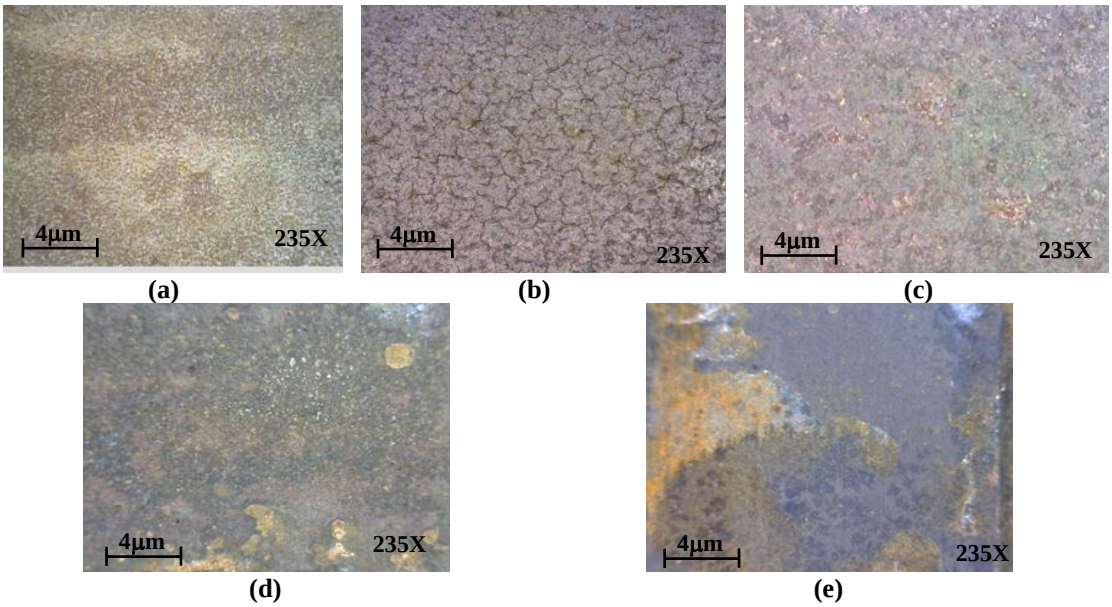

Figure 6.9 Optical micrographs of C110 specimens tested at 20.68 MPa and various PPR: a) Uncorroded; b) 0%; c) 50%; d) 75%; and e) 100%

Average corrosion rate obtained at 41.37 MPa is presented in Fig. 6.8b. Consistent with results obtained at 20.68 MPa (Fig. 6.8a), at low PPR (less than 25%), the corrosion rate significantly increased with PPR. This observation could be attributed to accelerated cathodic reaction (Nesic 2007), which facilitates corrosion process considerably. This is in agreement with the findings of Wang et al. (2004) who reported strong increase in cathodic limiting current density due to dominant effect of increased H_2CO_3 concentration, although anodic reaction is unaffected. This is very common corrosion rate trend, which has been reported by a number of theoretical and experimental studies (Nesic et al. 1996; Choi and Nesic 2011; Zhang et al. 2013a;

Dugstad et al. 1994; de Waard and Lotz 1993; Mohammed Nor et al. 2011). At low PPR (less than 25%), mixed charge transfer mechanism controls the corrosion process.

In intermediate PPR (between 25 and 75%), effect of PPR on the corrosion rate was minimal. Minor change in corrosion rate was observed with PPR, indicating change in corrosion mechanism. In intermediate PPR, CO_2 corrosion mechanism changes from mixed charge transfer control to cathodic reaction control, which leads to reduction of hydrogen ions (Tran et al. 2015). Similar corrosion rate trend with respect to PPR has been reported in previous studies (Choi and Nesic 2011; Gavanluei et al. 2013).

Optical micrographs of specimens tested at 41.37 MPa are presented in Fig. 6.10. At high PPR (greater than 75%), corrosion rate decreased by 46% due to formation of protective film, which was confirmed by examining corroded surface of test specimens (Fig. 6.10f). Usually protective film reduces corrosion rate (Seiersten 2001; de Waard and Lotz 1993; Seiersten and Kongshaug 2005; Lin et al. 2006). At PPR of 75%, severe pitting (Fig. 6.10e) was observed on one of the three tested specimens. The pitted specimen displayed considerably higher corrosion rate than the others. As a result, the highest data scattering was observed at PPR of 75%. Although the occurrence of pitting at elevated pressure is still being debated, this observation is found to be in agreement with a previous study (Zhang et al. 2011). However, some experimental studies (Sun and Nesic 2004; Suhor et al. 2012; Choi and Nesic 2011) conducted at low temperature (less than 50°C) did not report existence of localized corrosion.

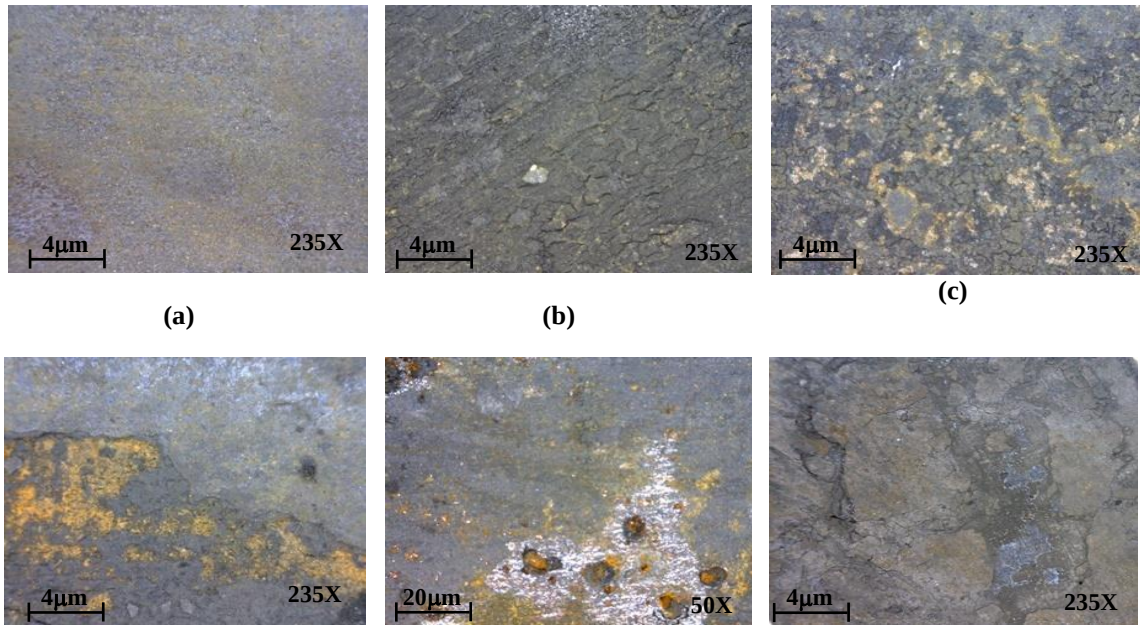

Figure 6.10 Optical micrographs of C110 specimens tested at 41.37 MPa and various PPR: a) 0%; b); 25% c) 50%; d) 75%; e) 75% showing pitting; and f) 100%

Two of the specimens exposed to the same corrosive environment did not show any pitting. Pitting corrosion is often initiated by a small surface defect. In order to minimize surface defect during manufacturing of the specimens, high-precision water-jet cutting and milling machines were used. Moreover, the specimens were well-polished and preserved in vacuum containers. In spite of this, one of the specimens exhibited pitting at 75% PPR. Further microscopic examination revealed that morphologies of corrosion scales did not vary significantly in the intermediate PPR range. This could be one of the possible reasons for high and consistent corrosion rate observed in the intermediate PPR range.

At 100% PPR, specimen surface was covered with more compact and dense corrosion product (Fig. 6.10f), which hindered the corrosion process. In absence of carbon dioxide (pure CH_4-saturated brine), no corrosion film was formed on specimen surface; nevertheless, corrosion rate was very low compare to tests conducted with CO_2-saturated fluid.

Figure 6.8c demonstrates the relationship between corrosion rate and PPR at 62.05 MPa and 38°C. Corrosion rate trend is similar to the one observed at intermediate pressure (41.37 MPa). At low PPR (less than 25%), the average corrosion rate was significantly increased with PPR. In the intermediate PPR range (25 to 75%), variations in corrosion rate was minimal. At 100% PPR, slight reduction in the corrosion rate was observed. The reduction in corrosion rate is consistent with formation of scattered corrosion scale that partially covered specimen surface. No localized corrosion (pitting) was observed under high-pressure condition.

Q125 Carbon Steel

Figure 6.11 displays average corrosion rate of Q125 API grade steels as a function of PPR at 41.37 MPa and 38°C. Corrosion rate of Q125 carbon steel increased roughly five fold when 25% of carbon dioxide was introduced to the system. Normally corrosion increases due to the formation of carbonic acid, which promotes the electrochemical reaction at metal surface. Moreover, the lack of protective scale on the specimen surface contributed to high corrosion rate (Fig. 6.12b).

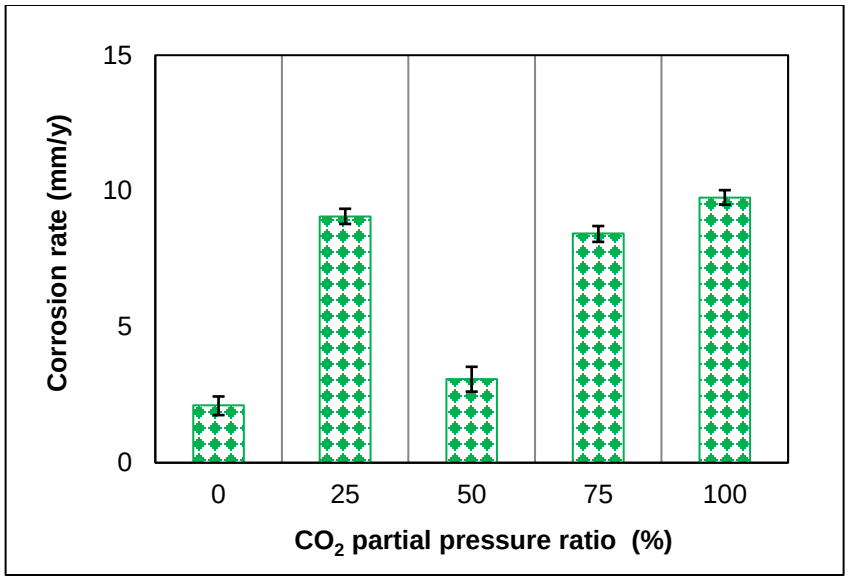

Figure 6.11 Average corrosion rate of Q125 grade steel vs. PPR at 41.37 MPa

Substantial reduction in corrosion rate of Q125 was observed as the PPR was increased from 25% to 50%. This reduction is mainly attributed to the formation of protective corrosion scale, which covered most of the specimen surface (Fig. 6.12c). At high PPR (greater than 50%), corrosion rate increased with PPR, because of increase in concentration of dissolved carbon dioxide.

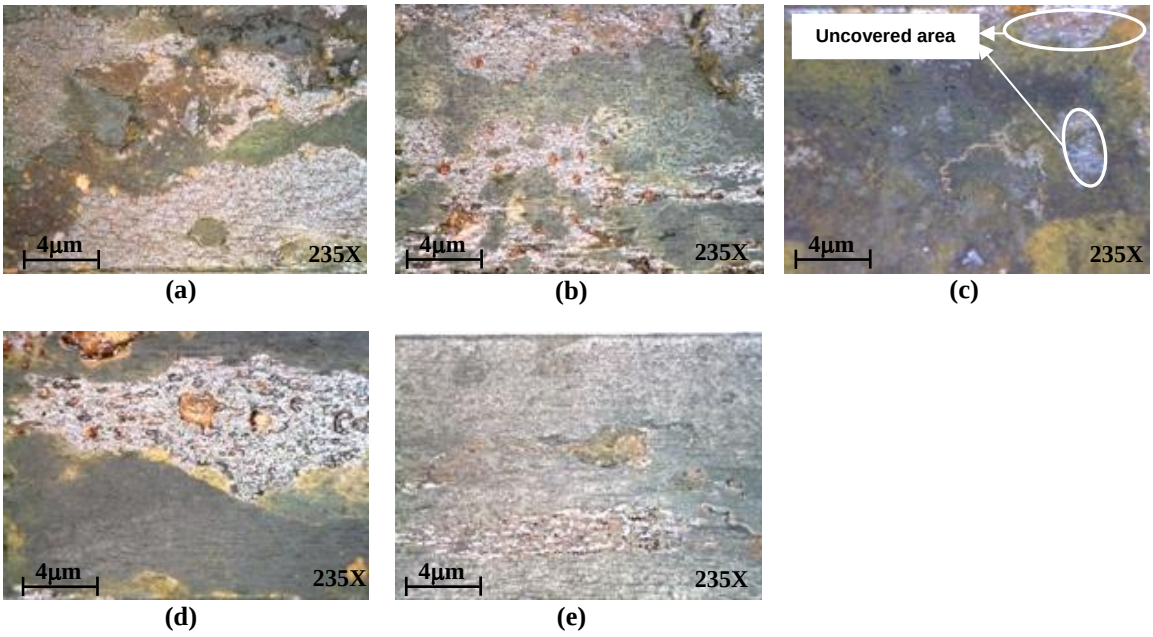

Figure 6.12 Optical micrographs of Q125 specimens tested at 41.37 MPa and various PPR: a) 0%; b); 25% c) 50%; d) 75%; and e) 100%

6.2.2 Effect of Hydrogen Sulfide Concentration

To evaluate the effect of H_2S concentration on CO_2 corrosion of API carbon steels (T95, C110, and Q125), a number of corrosion tests were carried out at 38°C, 41.37 MPa, PPR of 50% and various H_2S concentrations. The corrosion measurements are shown in Fig. 6.13.

T95 Carbon Steel

Average corrosion rate of T95 steel is shown in Fig. 6.13a as a function of H_2S concentration. The corrosion measurement was obtained at 38°C, 41.37 MPa and PPR of 50%. As displayed from the figure, at low H_2S concentrations (below 10 ppm H_2S), the presence of small amount of H_2S into mixed gas containing approximately 50% CO_2 and 50% CH_4 promotes corrosion. Increase in corrosion rate occurred due to

intensification of cathodic or anodic reaction (Valdes et al. 1998; Zheng et al. 2014). Moreover, adding hydrogen sulfide to CO_2 saturated brine tends to change the corrosion mechanism in which additional cathodic reactions such as direct H_2S reduction contribute to the corrosion process (Kittel at al. 2013; Zheng et al. 2014). The level of corrosion rate increase due to small addition of H_2S has been found in accordance with other similar studies (Valdes and Case 1998; Kittel at al. 2013; Wei et al. 2016). At H_2S concentration (more than 10 ppm), the corrosion rate trend changed; the rate reduced with the concentration up to 50 ppm and with further increase above 50 ppm, minor increase in the corrosion rate was noticed. As reported by Valdes et al. (1998), the maximum corrosion rate was observed at H_2S concentration of approximately 10 ppm.

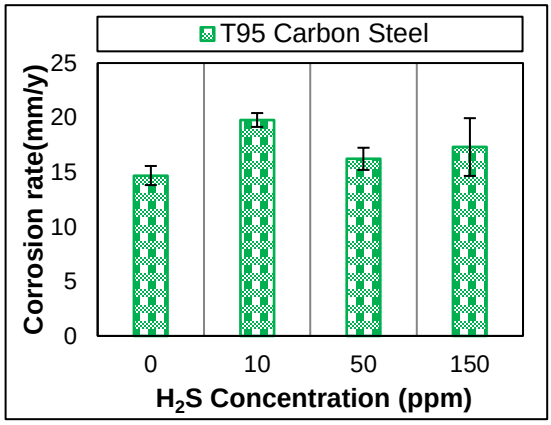

(a)

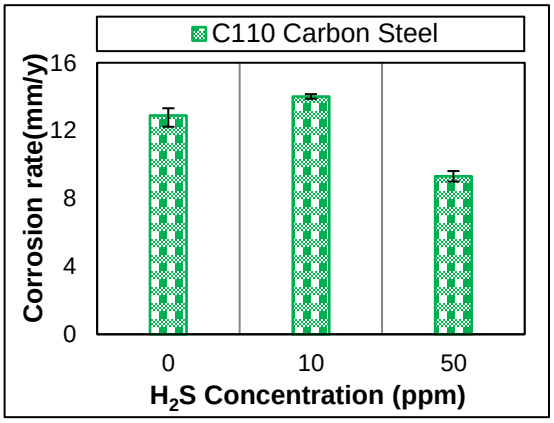

(b)

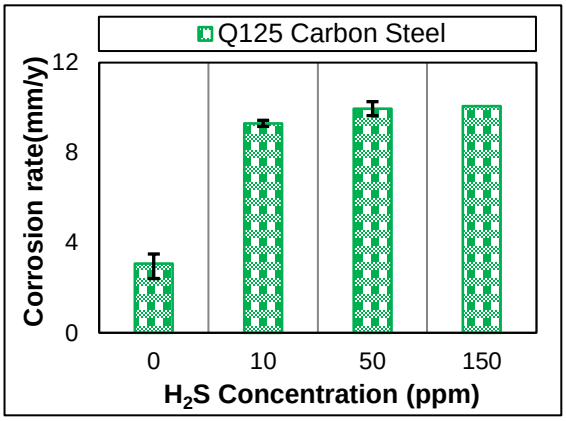

(c)

Figure 6.13 Corrosion rate vs. H_2S concentration at 41.37 MPa and 38°C for different materials: a) T95; b) C110; and c) Q125

In most recent studies (Sun et al. 2006; Yan et al. 2015) carried out under comparable conditions, the formation of $FeCO_3$ and mackinawite scales were observed in presence of H_2S. Figure 6.14 displays surface morphology of T95 specimens corroded at 41.37 MPa and 38°C varying H_2S concentration (ranging from 0 to 150 ppm). As depicted from the figure, when H_2S concentration was varied from 10 to 150 ppm, non-protective scales (i.e. less dense, un-compacted and scattered film) were formed on specimen surface. Normally, a loose corrosion scale is not effective in preventing diffusion of Fe^{2+} and does not reduce corrosion (Fig. 6.14). At intermediate H_2S concentration (50 ppm), a different corrosion scale was formed. Surface examination of the specimen demonstrated the existence of localized corrosion (Fig. 6.14b). Similar tests (Zhang et al. 2011) conducted at low-CO_2 pressures showed occurrence of localized (pitting) corrosion.

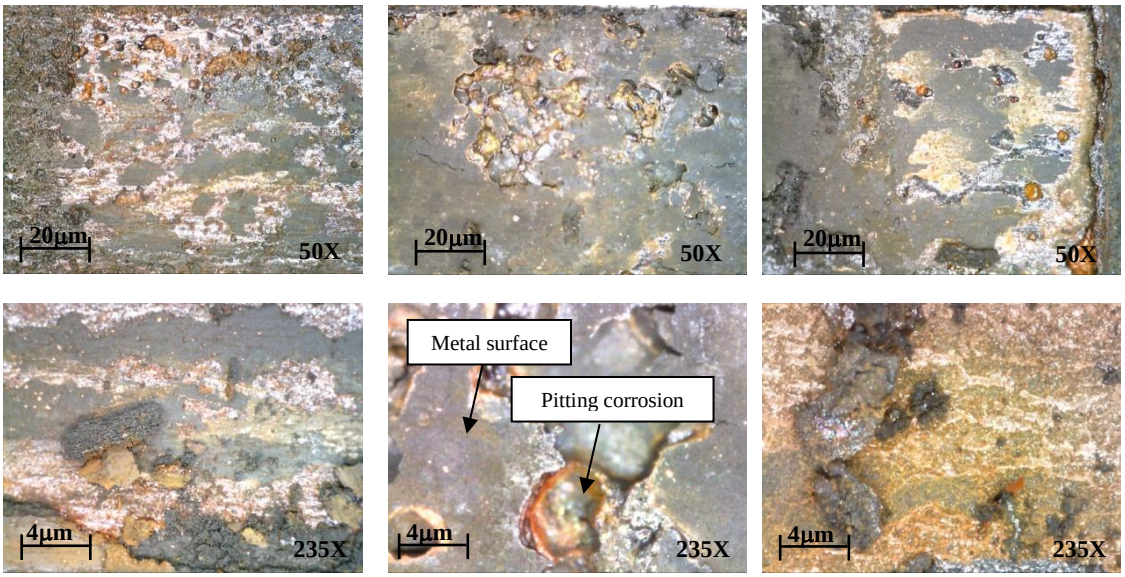

(a) **(b)** **(c)**

Figure 6.14 Optical micrographs of T95 specimens tested at 41.37 MPa and various H_2S Concentrations: a) 10 ppm; b) 50 ppm, and c) 150 ppm

C110 Carbon Steel

As displayed in Fig. 13b, adding trace amount of H_2S marginally accelerates corrosion. One possible explanation for this is that H_2S content enhances the cathodic reaction through two mechanisms: i) indirect effect by providing more protons to the solution (buffering effect); and/or ii) direct effect by adding a new reduction reaction to the corrosion process (i.e. direct reduction of aqueous H_2S). Consistent with T95 Grade trend, corrosion of C110 steel was exacerbated as H_2S was injected to system at low concentrations (less than 10 ppm). However, an apparent reduction (roughly 30%) in corrosion rate of C110 carbon steel was observed when H_2S concentration was further increased to 50 ppm. The reduction in corrosion rate at 50 ppm is in agreement with previous corrosion measurements (Marcus et al. 1990; Valdes et al. 1998; Zheng et al. 2014; 2015; Yan et al. 2012; Zhang et al. 2012; Li et al. 2014; Choi et al. 2011a). This

decline could be attributed to increase in dissolved amount of H_2S in the brine and formation of protective scale.

Specimens exposed to 50 ppm H_2S concentration were partially covered with a thin compact protective scale (Fig. 6.15d). A scattered non-protective corrosion scale formed (Fig. 6.15b) on the specimen surface in absence of H_2S. With addition of small amount of H_2S (10 ppm), the scale did not form and corrosion rate significantly increased. However, previous similar investigations (Valdes et al. 1998; Wei et al. 2016) carried out at relatively low-pressure reported the formation of scale consists of $FeCO_3$ and iron sulfides. Pitting corrosion was not detected with C110 specimens.

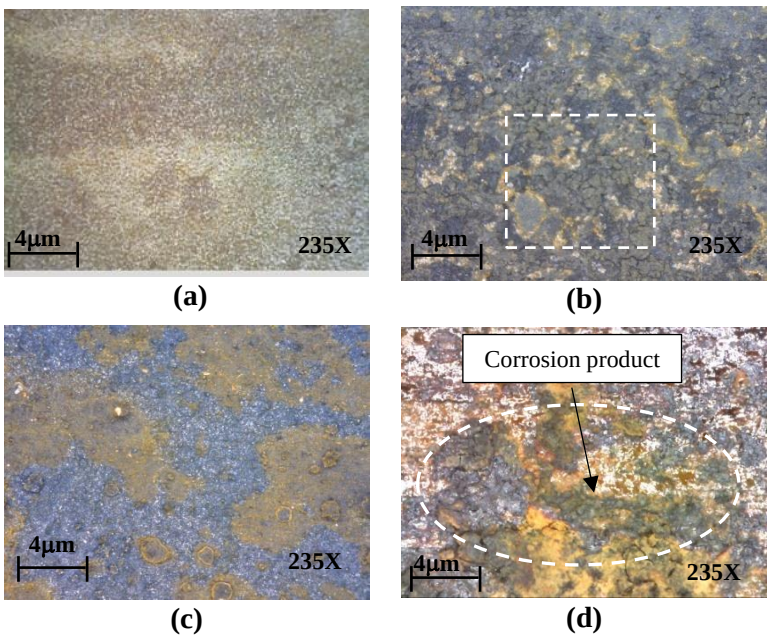

Figure 6.15 Optical micrographs of C110 specimens tested at 41.37 MPa and various H_2S concentrations: a) Uncorroded; b) 0 ppm; c) 10 ppm, and d) 50 ppm

Q125 Carbon Steel

Corrosion rate of Q125 accelerated considerably with introduction small amount of H_2S (10 ppm). As revealed from Fig. 13c, Minor variation in corrosion rate was observed as H_2S concentration was increased from 10 to 150 ppm. One possible explanation for the corrosion rate trend with H_2S content is involvement of two mechanisms (direct reduction and buffering effect), which are influenced by H_2S concentration (Tran et al. 2015; Elgaddafi et al. 2016b).

Figure 6.16 displays surface morphologies of corrosion scales formed on Q125 carbon steel exposed to brine-saturated with mixed gas containing approximately 50% CO_2 and 50% CH_4 and various concentrations of H_2S. In absence of H_2S, corrosion scale formed, resulting in relatively low corrosion rate (Fig. 6.16a). When specimens were exposed to brine saturated with mixed gas containing 10 ppm of H_2S, dense porous corrosion scales with small grain size were formed and partially covered specimen surface (gold colored scale shown in Fig. 6.16b). As the H_2S concentration increased, more scattered and un-compacted corrosion scales were formed on specimen surface (Figs. 6.16c and 6.16d). The scales did not provide good protection; as a result, corrosion rate slightly increased with H_2S concentration as reported by Li et al. (2014).

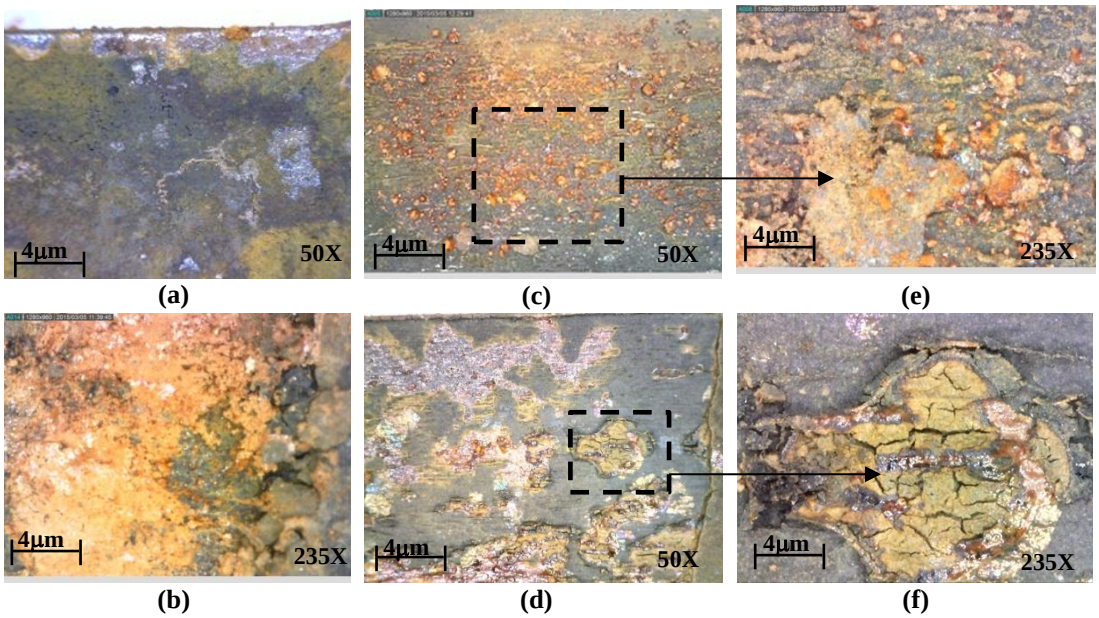

Figure 6.16 Optical micrographs of Q125 specimens tested at 41.37 MPa and various H_2S concentrations: a) 0 ppm; b) 10 ppm; c) 50 ppm and d) 150 ppm

Grain size and shape of corrosion scale vary with H_2S concentration (Fig. 6.16f). The influence of H_2S concentration on the grain size and shape of corrosion scale have been found in accordance with recent studies (Yan et al. 2012; Yan et al. 2015; Li et al. 2014a).

6.2.3 Effect of Temperature

Temperature is considered one of the most critical environmental variables in sweet and sour corrosion. It affects most of the phenomena involved in the corrosion process. The influence temperature on corrosion of API steels was investigated at 41.37 MPa varying temperature from 38 to 107°C. Specimens were exposed to brine saturated with mixed gas (50% CO_2 and 50% CH_4) under static condition. Average corrosion rates of tested materials are shown in Fig. 6.17. All grades showed similar corrosion rate-temperature trend in which the corrosion rate sharply decreased with temperature. The

reduction is mainly attributed to reduction in the dissolved amount of carbon dioxide with temperature. Q125 carbon steel exhibited the best corrosion resistance. At high temperature (107°C), three tested materials demonstrated comparable corrosion rates.

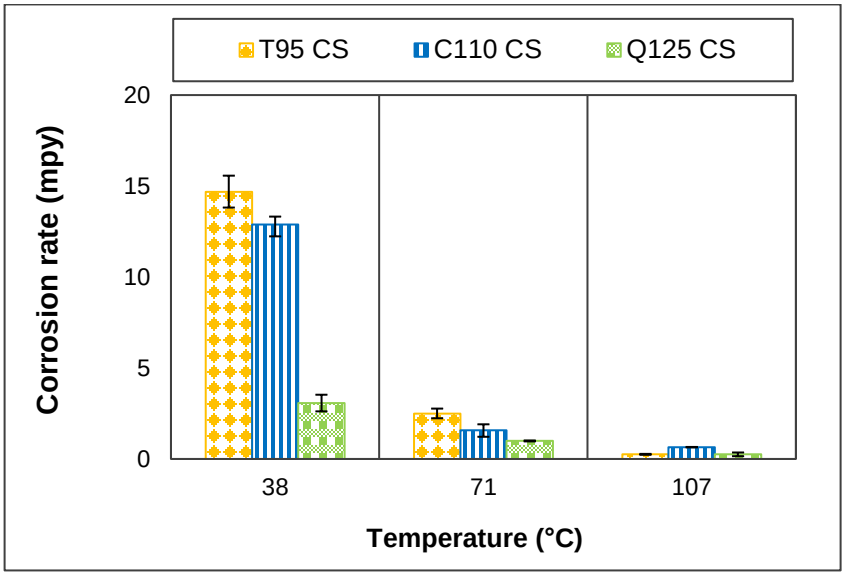

Figure 6.17 Effect of test temperature on the corrosion behavior of tested material T95, C110, and Q125 at 50% CO_2 and 41.37 MPa of total pressure

Figure 6.18 shows surface morphologies of corrosion scales formed on tested materials at intermediate (71°C) and high (107°C) temperatures. At intermediate temperature (71°C), very scattered and un-compacted corrosion scale was formed on T95 specimen, resulting in pitting corrosion (Fig. 6.18a); while, denser and protective scales were formed on C110 and Q125 carbon steels (Figs. 6.18c and 6.18e) causing reduction in corrosion rate. The surface analysis conducted on the specimens tested at high temperature (107°C) revealed varieties of corrosion scales from being scattered to nonexistent (Figs. 6.18b, 6.18d, and 6.18f).

The surface morphologies of corrosion scale formed on T95, C110, and Q125 at low temperature (38°C) are presented in Figs. 6.7b, 6.10c, and 6.12c, respectively. According to the analysis, the thickest and the thinnest scales were observed with Q125 and T95, respectively.

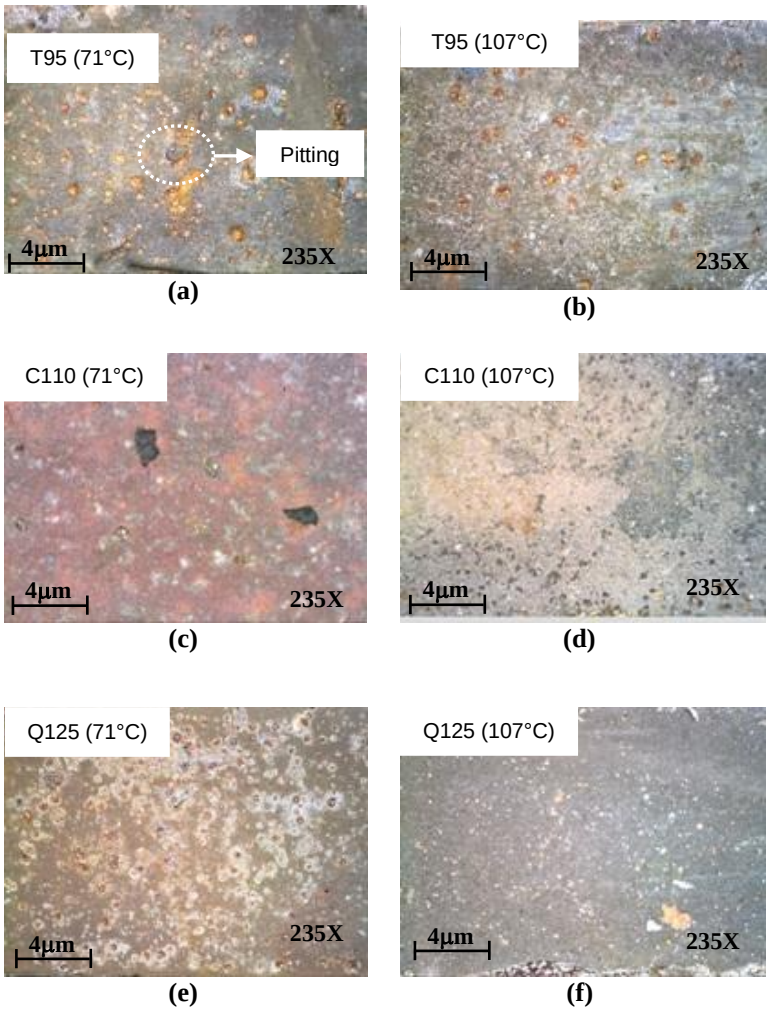

Figure 6.18 Optical micrographs of specimens tested at 41.37 MPa and 50%CO_2 concentrations: a) T95 (71°C); b) T95 (107°C); c) C110 (71°C); d) C110 (107°C); e) Q125 (71°C) and f) Q125 (107°C)

6.2.4 Effect of Flow Velocity

To assess the impact of fluid flow on corrosion behavior of steel, a set of corrosion tests were carried out varying fluid velocity in a Couette cell in which inner cylinder is rotating and outer cylinder is stationary.

T95 Carbon Steel

Figure 6.19a presents average corrosion of T95 carbon steel exposed to 2% NaCl solution saturated with mixed gas containing 50% CO_2 and 50% CH_4 at 41.37 MPa. Inner cylinder rotational speed was varied from 0 to 600 rpm. At 38°C, CO_2 corrosion rate increased significantly (almost doubled) as the inner cylinder rotational speed was increased to 216 rpm (Fig. 6.19a). Corrosion-rate trend with fluid velocity is as expected. It indicates that the corrosion process is controlled by mass transport mechanism; as a result, increasing the rotational speed is expected to enhance the transport of species toward and away from the metal surface. The process promotes corrosion and ultimately increases its rate. The increase in corrosion rate with rational speed has been found in agreement with previous study carried out at relatively low pressure and temperature (Nesic et al. 1995; Mohammed Nor et al. 2012; Mohammed Nor et al. 2011).

As the rotational speed was increased above 216 rpm, minor change in the CO_2 corrosion rate was observed. This implies that the corrosion mechanism changed from being mass transport controlled process to mixed charge/chemical reaction controlled at high fluid velocity. Similar results have been obtained when tests were conducted at low-pressure (Nesic et al. 1995; Mohammed Nor et al. 2011). Corrosion rate becomes

insensitivity to fluid velocity at low temperature (less than 40°C) possibly due to the dominate effect of carbonic acid reduction, which is limited by the hydration of dissolved CO_2 (Wang et al. 2004; Mohammed Nor et al. 2012).

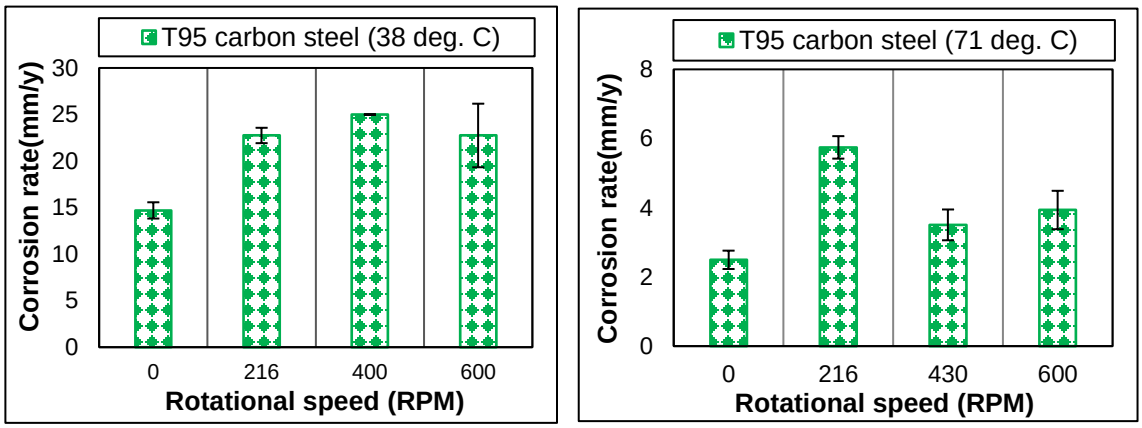

(a) **(b)**

Figure 6.19 Corrosion rate of T95 vs. rotational speed (2% NaCl, 50% CO_2, 50% CH_4 at 41.37 MPa): a) 38°C; and b) 71°C

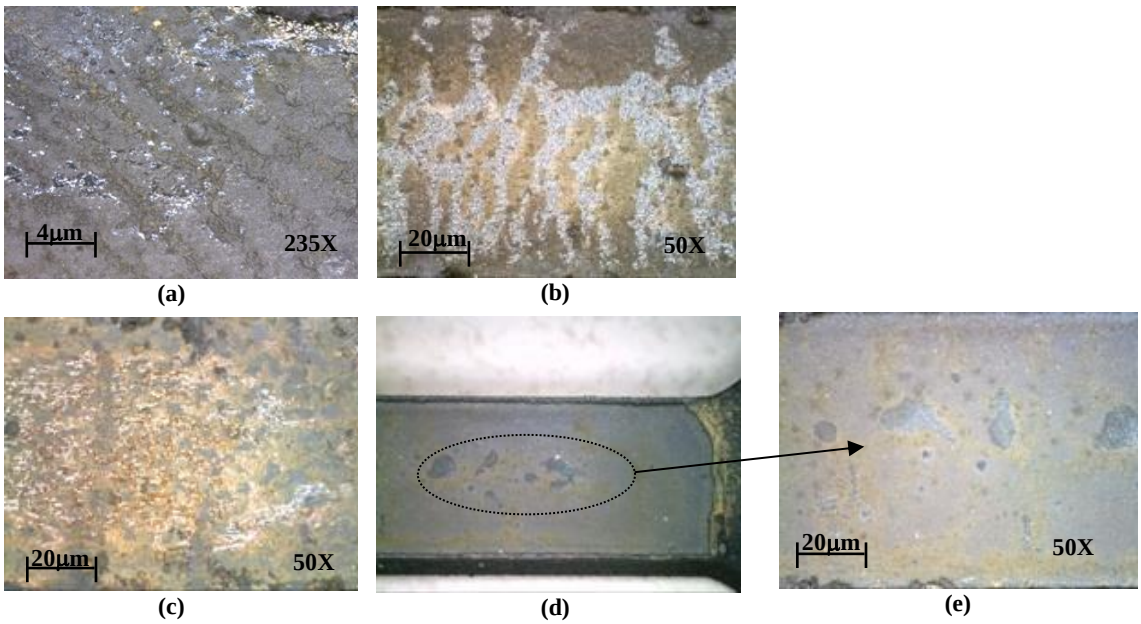

(a) **(b)** **(c)** **(d)** **(e)**

Figure 6.20 Optical micrographs of T95 specimens tested at 41.37 MPa, 38°C and various rotational speed: a) 0 rpm; b) 216 rpm, c) 400 rpm, d) 600 rpm, and e) 600 rpm (50X)

Figure 6.20 displays surface micrographs of T95 test specimens after exposure. Very thick corrosion scale precipitated (Fig. 6.20a) on T95 specimen tested under static condition. The scale resulted in low corrosion rate. Under dynamic condition, very thin non-protective corrosion scale was formed on specimens (Fig. 6.20b, 6.20c, and 6.20e). It is important to note that corrosion scales formed under dynamic condition had similar characteristics. This observation explains insensitivity of corrosion rate with rotational speed at high speeds (greater than 216 rpm)

Figure 6.19b shows corrosion of T95 as a function of rotational speed at 71°C. A substantial reduction in corrosion rate was observed as temperature was raised from 38 to 71°C regardless of rotational speed. The maximum corrosion rate was observed at 216 rpm. It is noteworthy that corrosion test at 216 rpm was carried out twice and measurements were almost the same. The corrosion rate decline due to change in temperature could be because of reduced gas and $FeCO_3$ solubility in brine. Increasing temperature considerably reduces dissolved CO_2 in brine and thus carbonic acid content (CO_2 hydration reaction), leading to corrosion rate reduction. Increase in temperature decreases solubility of $FeCO_3$ in brine and accelerates formation of protective scale, which reduces corrosion rate.

Furthermore, temperature has an impact on flow-sensitivity of corrosion rate in which the corrosion rate vs. speed trend at 71°C is distinguished from that at 38°C. As anticipated, the corrosion was increase by roughly three fold as the rotational speed was increased to 216 rpm (Fig. 6.19). This increment is attributed to mass transport enhancement and formation of iron carbide scale, which causes galvanic effect that

accelerates the corrosion (Dugstad et al. 1994). Subsequently, the corrosion rate declined as the speed was increased to 430 rpm. However, the corrosion rate under dynamic condition was considerably higher than that at stagnant condition. Low corrosion rate occurred under stagnant condition due to formation of scale, which commonly consists of iron carbide and iron carbonate (Fig. 6.21). In this case, the scale diminished corrosion by acting as a diffusion barrier preventing ionic transport and promoting less galvanic effect due to reduced iron carbide content. Minor change in corrosion rate was observed as the speed was increased from 430 to 600 rpm. In general, the flow minimizes super-saturation by enhancing the ionic transport and results in formation of porous and uncompacted corrosion scale (Dugstad 1998).

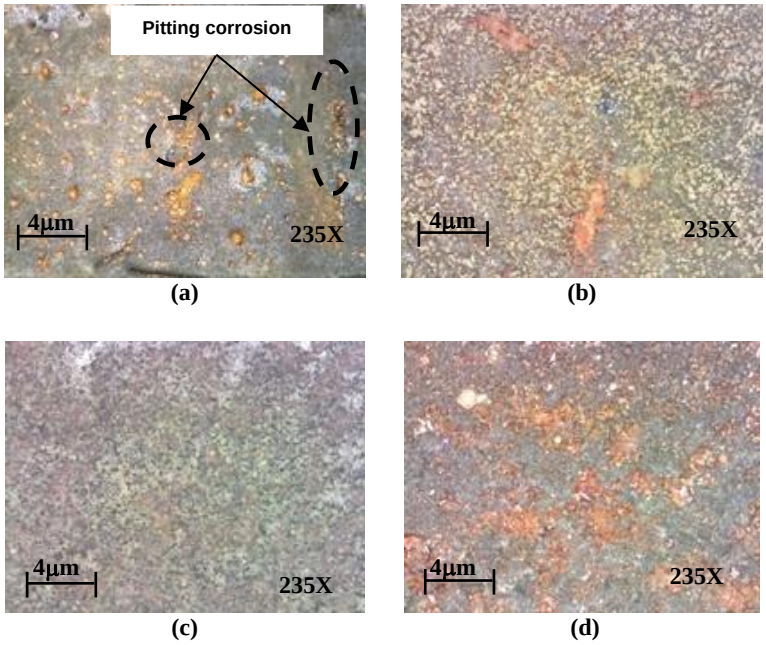

Figure 6.21 Optical micrographs of T95 specimens tested at 41.37 MPa, 71°C and various rotational speeds: a) 0 rpm; b) 216 rpm, c) 430 rpm, and d) 600 rpm.

Q125 Carbon Steel

Q125 carbon steel was similarly tested under dynamic condition to assess its corrosion resistance. Figure 6.22a presents corrosion rate of Q125 exposed to 2% NaCl solution saturated with mixed gas containing 50% CO_2 and 50% CH_4 at 41.37 MPa and 38°C. The test was carried out varying rotational speed from 0 to 1000 rpm. The corrosion rate consistently increased with fluid velocity. It increased approximately four fold as the flow status changed from being static to dynamic (216 rpm). Significant increase in corrosion rate indicates diffusion controlled corrosion process. Under dynamic condition, the corrosion rate gradually increased with rotational speed. Corrosion rate became less flow-sensitive at high fluid velocities. Although the speed was increased to 1000 rpm, the mass transfer process maintained its control.

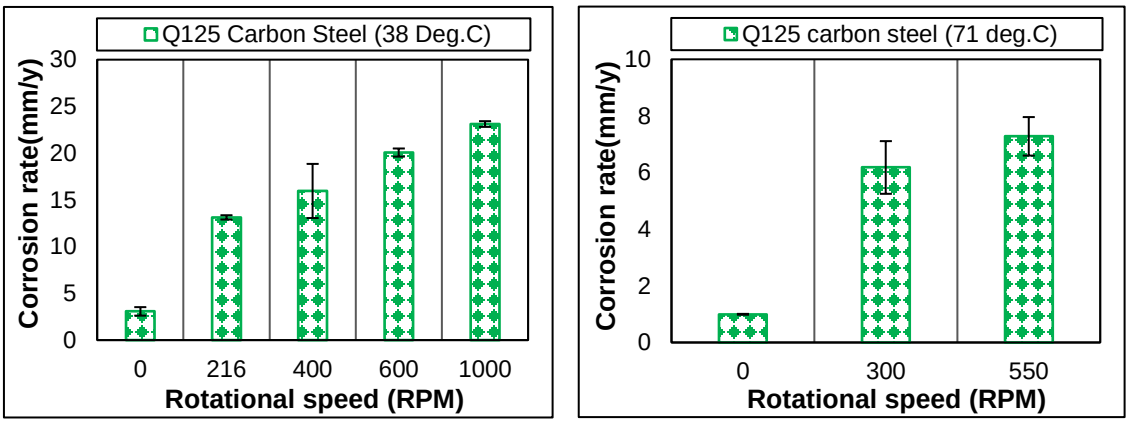

Figure 6.22 Corrosion rate of Q125 vs. rotational speed (2% NaCl, 50% CO_2, 50% CH_4 at 41.37 MPa): a) 38°C; and b) 71°C

It is evident that mass transport mostly dominates the corrosion process at low fluid velocities. At low fluid velocities, the corrosion process is often controlled by charge transport or electrochemical reaction. Moreover, it is indicated that hydrogen

ions reduction is more pronounced in the total cathodic reaction. Similar findings were obtained by previous studies (Denpo and Ogawa 1993; Hara et al. 2000). Figure 6.23 shows the surface micrographs of test specimens. Corrosion scale formed on the specimen surface became gradually less intensive and protective as the speed was increased. The flow velocity retards formation of corrosion scale by improving the transport of corrosion product species away from specimen surface and reduce the possibility of attaining super-saturation level.

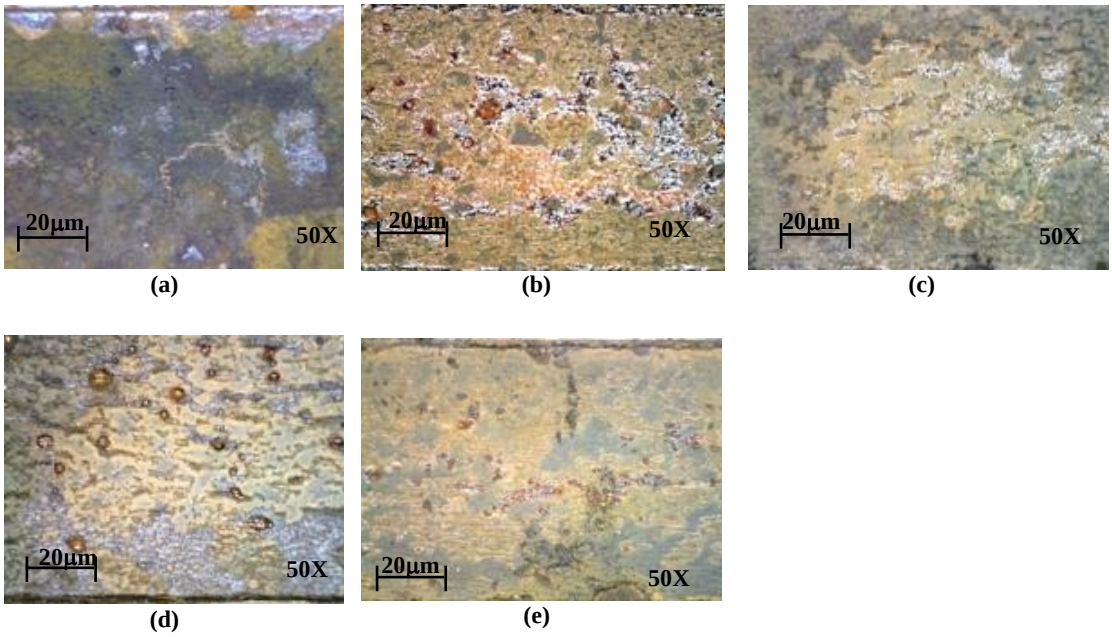

Figure 6.23 Optical micrographs of Q125 specimens tested at 41.37 MPa, 38°C and various rotational speeds: a) 0 rpm; b) 216 rpm, c) 400 rpm, d) 600 rpm, and e) 1000 rpm

Similarly, corrosion tests were carried out at high temperature (71°C) using specimen of Q125 carbon steel. Due to technical issues, the test was conducted at two different speeds (300 and 550 rpm) in addition to stagnant condition. Figure 6.22b

presents corrosion rate as a function of rotational speed at 71°C. Corrosion-rate trend with speed is similar to that observed at low temperature (i.e. consistent increase with speed). Considerable increase in speed up to 300 rpm results in remarkable increase in the corrosion rate, which is roughly six fold. The increase in corrosion rate could be explained by the enhancement in mass transport process of active species. Moderate increase in corrosion rate was observed when the speed was doubled to 600 rpm. Figure 6.24 shows the surface micrographs of tested specimens. Scattered corrosion scales formed on the specimen surface. The scales only provide partial protection.

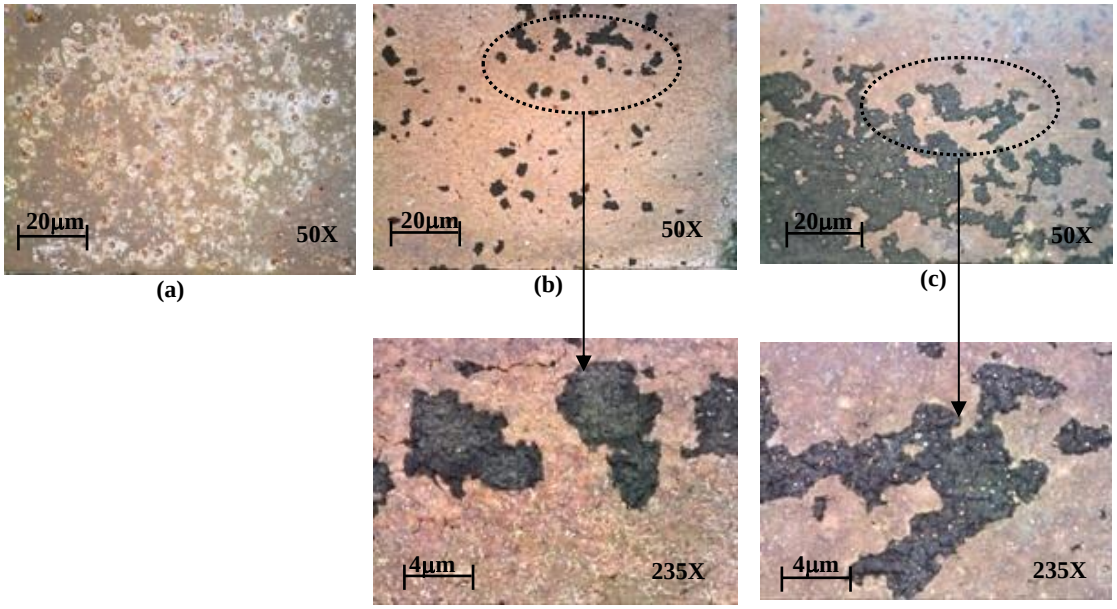

Figure 6.24 Optical micrographs of Q125 specimens tested at 41.37 MPa, 71°C and various rotational speeds: a) 0 rpm; b) 300 rpm, and c) 550 rpm

6.2.5 Effect of Material Type

Selecting a suitable tubular material for acidic environment is an important step in well-bore design. Each type of API grade steel has specific corrosion resistance. Figure 6.25

compares corrosion resistance of API carbon steels. Q125 grade steel showed superior corrosion resistance by providing lowest corrosion rate with or without presence of H_2S in the mixed gas. Corrosion rate of Q125 steel was as low as 3 mm/y in brine saturated with sweet mixed gas. However, its corrosion resistance reduced as small hydrogen sulfide was injected into the CO_2 saturated brine. Variations in corrosion behavior of the materials are attributed to difference in their chemical compositions. Chemical compositions of carbon steels (T95, C110 and Q125) used in this study vary slightly (Table 5.3). Obvious difference is perceived in the concentrations of alloying elements (Chromium, Manganese, Nickel and Carbon).

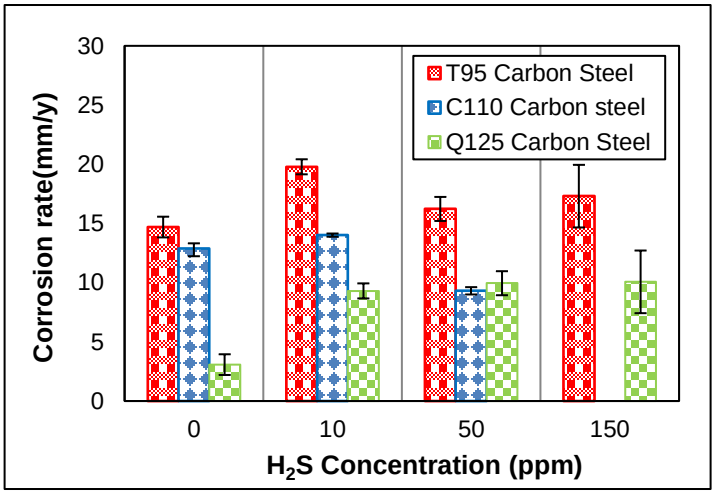

Figure 6.25 Comparison of average corrosion rate of three tested materials T95, C110 and Q125 exposed to CO_2-H2S environment at 41.37 MPa, 38°C and static condition

The influence of Cr-containing element on the CO_2 corrosion resistance of steel at low pressure conditions have been extensively investigated (Takabe and Ueda 2001; Sun et al. 2009a; Sun et al. 2016; Kermani et al. 2001; Liu et al. 2009; Hu et al. 2011; Chen et al. 2005a; Hassani, et al. 2014). There is a prevalent consensus that Cr-rich

steels (i.e. Cr content of more than 3%) display a higher uniform corrosion resistance in sweet corrosion environment than regular carbon steels (Sun et al. 2016; Kermani et al. 2001; Liu et al. 2009; Hu et al. 2011; Chen et al. 2005a; Hassani et al. 2014). Nevertheless, in the most recent sweet corrosion studies (Yevtushenko et al. 2014; Pfennig and Kranzmann 2012), a localized corrosion (pitting corrosion) was detected on the surface of Cr-rich (between 1% and 13%) steel alloys under elevated pressure and temperature conditions (100 bar and 60°C).

In contrary to previous findings, corrosion measurements revealed that Q125 steel provides the highest corrosion resistance even though its composition contains the lowest Cr concentration. It is important to note that Q125 carbon steel has higher content of Mn and Ni. The presence of chromium with high content of manganese improves the corrosion resistance of carbon steels in CO_2-H_2S environment (Suk Seo et al. 2015).

Reaction mechanism of Cr-rich material in CO_2-H_2S environment is more complex than that in pure CO_2 environment; as a result, corrosion resistance of Cr-rich steels in CO_2-H_2S environment is different from that in CO_2 saturated brine (Liu et al. 2015; Sun et al. 2009a). Very limited corrosion studies (Sun et al. 2016; Liu et al. 2015; Suk Seo et al. 2015; Yin et al. 2012) have been conducted to determine effects of alloying element on corrosion behavior of carbon steel in CO_2-H_2S environment. The outcomes of these studies are not consistent on the effect of chromium alloying on corrosion of steels. Liu et al. (2016) has compared the corrosion behavior of 3%Cr alloy with API X60 carbon steel under elevated pressure (2.5 MPa) and temperature

(90°C). Interestingly, the alloy displayed higher corrosion resistance than API X60. The improvement in the corrosion resistance of alloying steel is attributed to formation of a triple-layer corrosion scale consisting of FeS (outer layer), $FeCO_3$ (middle layer) and mixture of $FeCO_3$, Cr $(OH)_3$ and Cr_2O_3 (inner layer).

Figure 6.26 compares the corrosion behavior of two tested materials (T95 and Q125 carbon steels) at 41.37 MPa, 38°C varying rotational speed. Both materials reveal similar corrosion trend with rotational speed. However, under this test condition, Q125 exhibits again higher corrosion resistance than T95, which is more apparent under static condition. However, it can be seen that the difference in the corrosion rate diminishes with rotational speed. It became negligible at rotational speed of 600 rpm. The superior corrosion resistance of Q125 is attributed to the characteristic of corrosion scale and its composition (i.e. low Cr, high Mn and low carbon contents). The cementite scale is commonly formed at low temperature with steel that has low carbon content (Gulbrandsen et al. 1998; Cabrini et al. 2014). Al-Hassan et al. (1998) found a relationship between corrosion rate and carbon content in which corrosion rate increases with carbon content. Moreover, high Mn and low Cr contents can improve corrosion resistance of carbon steels (Sun et al. 2016; Suk Seo et al. 2015).

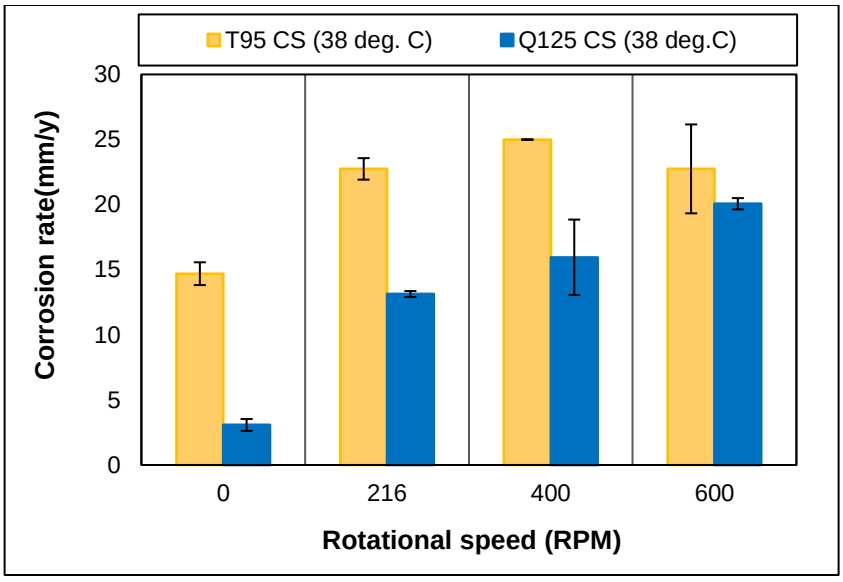

Figure 6.26 Comparison of carbon steels resistance in 2% NaCl solution saturated with 50% CO_2 at different rotational speeds, 41.37 MPa and 38°C

6.2.6 Effect of Pressure

Figure 6.27 compares corrosion rate of three API grade steels exposed to 2% NaCl solution saturated with mixed gas containing 50% CO_2 and 50% CH_4 (i.e. CO_2 PPR = 50%) at 38°C. Corrosion rate of Q125 showed a different trend with pressure. For T95 and C110, the maximum corrosion rate was observed at 41.37 MPa due to the absence of protective corrosion scale. In contrast, Q125 displayed the best corrosion resistance at 41.37 MPa by demonstrating the lowest corrosion rate. It is noteworthy that three tested materials demonstrated comparable corrosion resistance at 62.05 MPa.

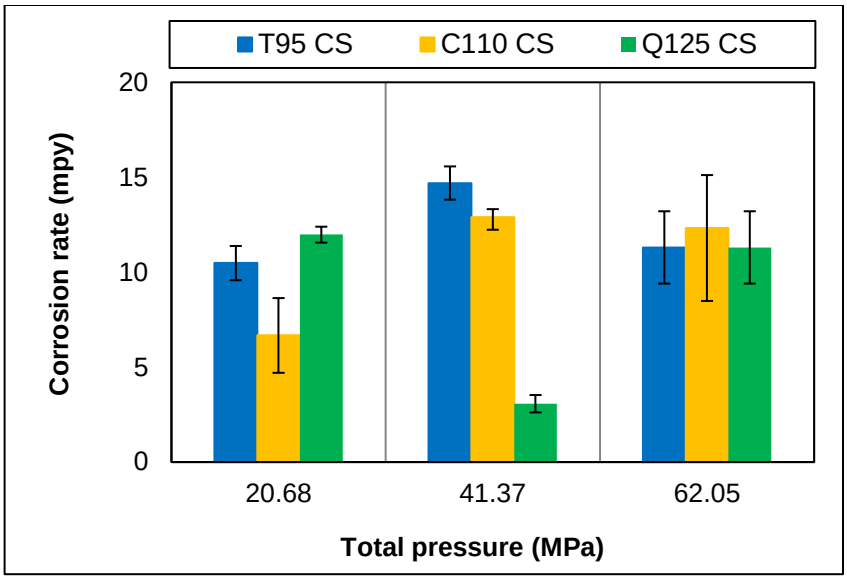

Figure 6.27 Effect of pressure on corrosion behavior of T95, C110, and Q125 at 50% CO_2 and 38°C

Figure 6.28 compares corrosion rate of C110 obtained at CO_2 PPR of 100% and different pressures (20.68, 41.37, and 62.05 MPa). The maximum corrosion rate was observed at 20.68 MPa due to absence of protective scale (Fig. 6.29a). Corrosion rate considerably reduced as the pressure was increased to 41.37 MPa.

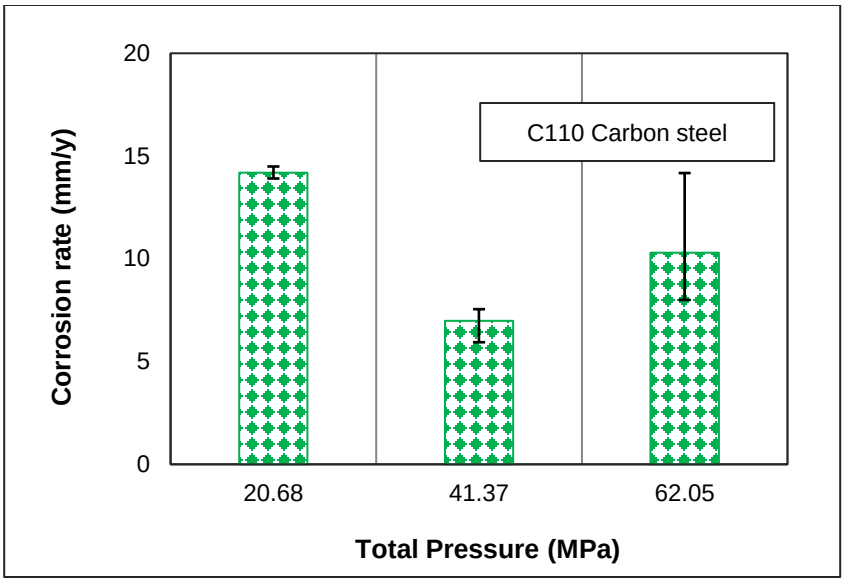

Figure 6.28 Corrosion rate of C110 vs. pressure at 100% PPR

The reduction in corrosion rate occurred due to formation of protective scale (Fig. 6.29b) that creates a diffusion barrier and slows down the corrosion process. Corrosion rate increased by 30% as the pressure was elevated to 62.05 MPa. This behavior can be attributed to increase in concentration of carbonic acid in surrounding brine solution. As the amount of dissolved CO_2 increases, concentration of carbonic acid increases and accelerates cathodic reactions. In addition, corrosion product formed at 62.05 MPa (Fig. 6.29c) was lower in density and compaction than the one formed at 41.37 MPa (Fig. 6.29b).

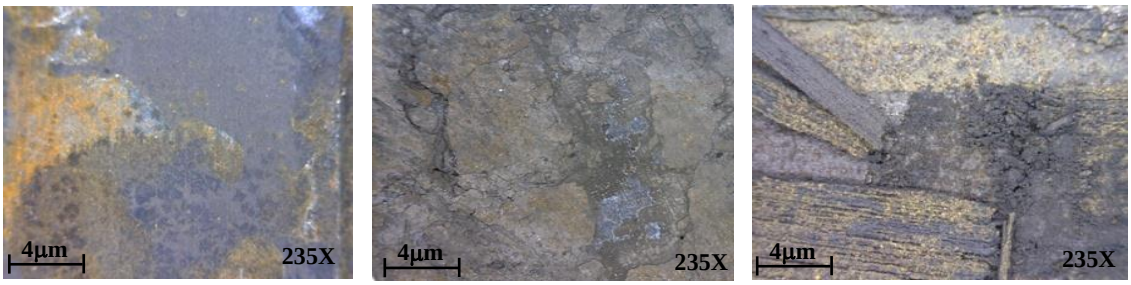

(a) **(b)** **(c)**

Figure 6.29 Optical micrographs of C110 specimens tested at 100% PPR and various pressures: a) 20.68 MPa; b); 41.37 MPa; and c) 62.05 MPa

6.3 Tensile Strength Measurement

A metal exposed to a corrosive environment experiences material loss, which is often measured as thickness reduction. However, localized and intergranular corrosion can reduce metal strength without significant material loss. In this study, total loss of material strengths (total reduction of load carrying capacity, ΔLCC_T) and loss of material strength due to uniform corrosion (reduction of load carrying capacity due to uniform corrosion, ΔLCC_{uc}) are compared to identify presence of intergranular and/or localized corrosion. The reduction in load capacity is chosen for the comparison purpose because it displays a trend, which is similar to the corrosion rate. To perform the comparison, uncorroded and corroded specimens of each material were stretched to the breaking (failure) point to determine ultimate tensile strength of the materials. Load carrying capacity of specimens measured at the breaking point is the total load carrying capacity. Tensile strength testing apparatus, presented in Elgaddafi et al. (2016b), was used to measure load carrying capacity of the specimens. Reduction of load carrying

capacity because of uniform corrosion (ΔLCC_{uc}) can be predicted using weight loss measurement. Thus:

$$\Delta LCC_{uc} = \Delta T * w * UTS \tag{6.1}$$

where, w and ΔT are specimen width and average specimen thickness reduction, respectively. UTS is ultimate tensile strength. The average thickness reduction is determined from weight loss measurement as:

$$\Delta T = \frac{(W_1 - W_2)}{A\rho_{st}} \tag{6.2}$$

Total (overall) reduction in carrying capacity of specimen (ΔLCC_T) is determined from measured LCCs of uncorroded and corroded specimens as:

$$\Delta LCC_T = LCC_{uncor} - LCC_{cor} \tag{6.3}$$

where, LCC_{uncor} and LCC_{cor} are measured load carrying capacities of uncorroded and corroded specimens, respectively. Average load carrying capacities of uncorroded specimens are presented in Table 6.1.

Table 6.1 Average load carrying capacity of uncorroded specimens

	T95	**C110**	**Q125**
LCC_{uncor} (KN)	9.97	11.02	13.22

6.3.1 Effect of CO_2 Partial Pressure

Figure 6.30 shows the comparison between ΔLCC_T and ΔLCC_{uc} for C110 API steel grade at various PPRs (0 – 100%) and pressures (20.68, 41.37, and 60.05 MPa). The comparison demonstrated good agreement between the trend of total LCC reduction and LCC decline due to uniform corrosion. In addition, the results indicate that total LCC reduction is slightly higher than ΔLCC_{uc}, which is predicted from the strength. Indications of higher total LCC reduction can be evidence of the occurrence of localized corrosion and/or minor irregularities of uniform corrosion, which cause localized thinning of specimens. Since thickness of corroded specimens were slightly (approximately 0 to 20%) varying with location, failure during tensile test was predominantly occurring at a location where specimen thickness was relatively low. As a result, the ΔLCC_{uc} formula (Eq. 6.1) underestimates the actual reduction in LCC due to the use of average specimen thickness. Even though the ΔLCC_{uc} is underestimated, it is still found to be comparable with total LCC reduction. The results (Fig. 6.30) do not indicate the occurrence of effective localized corrosion such as pitting and intergranular corrosion, which often have profound effect on mechanical properties of corroded metals. For C110 specimens exposed to pure CO_2 saturated brine, the difference between ΔLCC_T and ΔLCC_{uc} falls in the range of 0 to 30%, which is approximately the variation normally observed in specimen thickness. This indicates that the uniform corrosion is a dominant contributor to the total carrying capacity reduction and demonstrates minor contribution of localized corrosion.

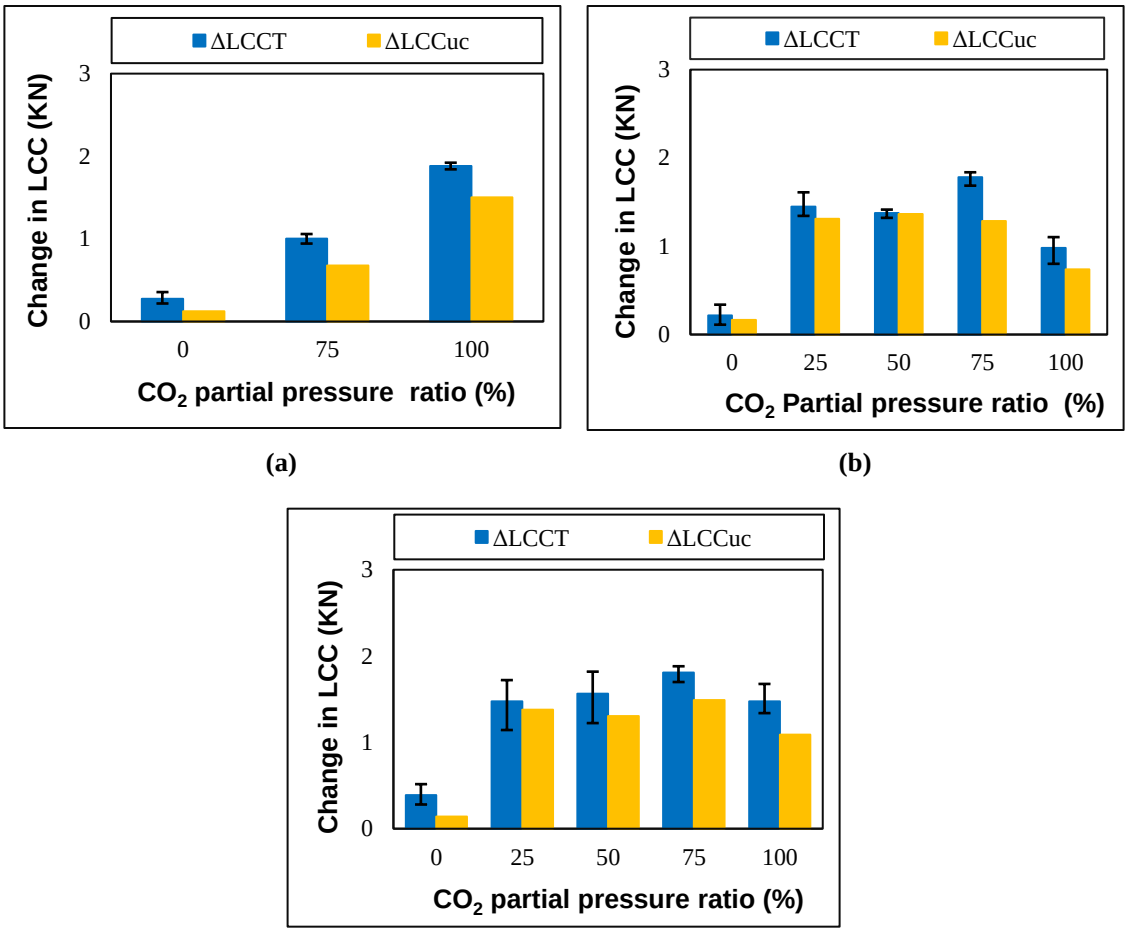

Figure 6.30 ΔLCCT and ΔLCCuc of C110 as a function of PPR at different pressures: a) 20.68 MPa; b) 41.37 MPa; and c) 62.05 MPa

6.3.2 Effect of H_2S Concentration

Presence of H_2S can reduce ductility and increase embrittlement due to intergranular attack resulting from liberated hydrogen atom during corrosion process and catalytic nature of H_2S. Mechanical properties of T95, C110, and Q125 API grade steels were measured after exposure to brine saturated with mixed gas containing approximately 50% CO_2, 50% CH_4 and various concentrations of H_2S (0 to 150 ppm) at 40.37 MPa and 38°C under static condition. After exposure to the corrosive environment, specimen thickness diminished due to corrosion and resulted in reduction of load carrying

capacity of corroded specimens. Average measured tensile force as a function of strain for uncorrroded and corroded specimens are shown in Fig. 6.31.

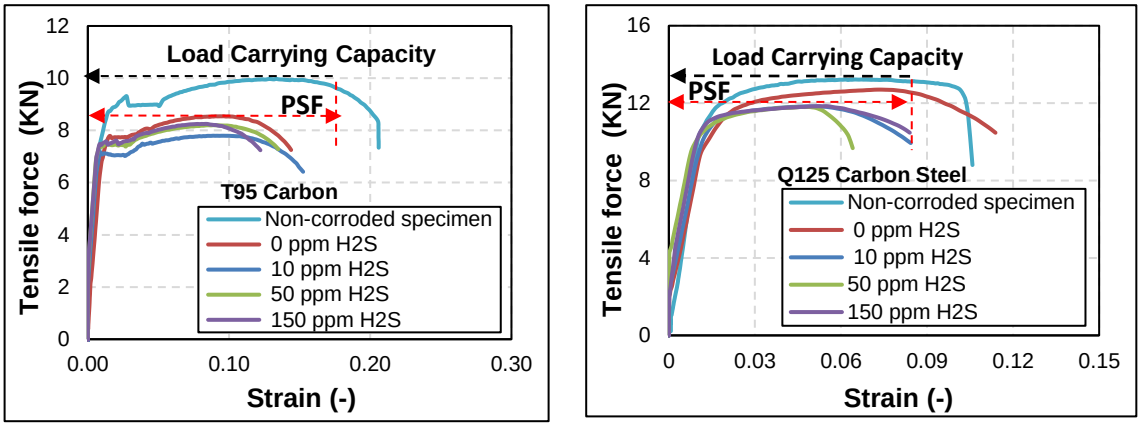

(a) **(b)**

Figure 6.31 Tensile force vs. strain for specimens exposed to brine saturated with mixed gas containing various concentrations of H_2S at 41.37 MPa and 38°C: a) T95; and b) Q125

Considerable change in mechanical properties such as ultimate tensile strength (UTS) and Plastic Strain before Failure (PSF) occurred when it exposed to the corrosive environment containing H_2S. The UTS and PSF of both grades reduced after exposure. In general, PSF gradually diminishes with H_2S concentration. This implies reduction in ductility and increases in embrittlement of T95 and Q125 due to presence of small amount of aqueous H_2S. Moreover, LCC of Q125 is slightly reduced when test specimens were exposed to the environment due to specimen thickness loss.

Figure 6.32 compares ΔLCC_T and ΔLCC_{uc} at different H_2S concentration for three tested materials. In general, there is slight non-uniformity in corrosion and subsequently thickness reduction; and the total LCC reduction is slightly higher than $\Delta LCC_{uc.}$ For T95 carbon steel, ΔLCC_T and ΔLCC_{uc} show good agreement indicating

absence of hidden corrosion during exposure to the test fluid. Similar results were obtained with other grades (C110 and Q125) except at H_2S concentration of 50 ppm. Since pitting was not detected from the optical micrographs, abnormal reduction in load carry capacity could be attributed to structural damage occurred during the exposure. Due to their high strength and brittleness, C110 and Q125 are more susceptible for wet H_2S cracking, which can be exacerbated due to residual or/and applied stresses.

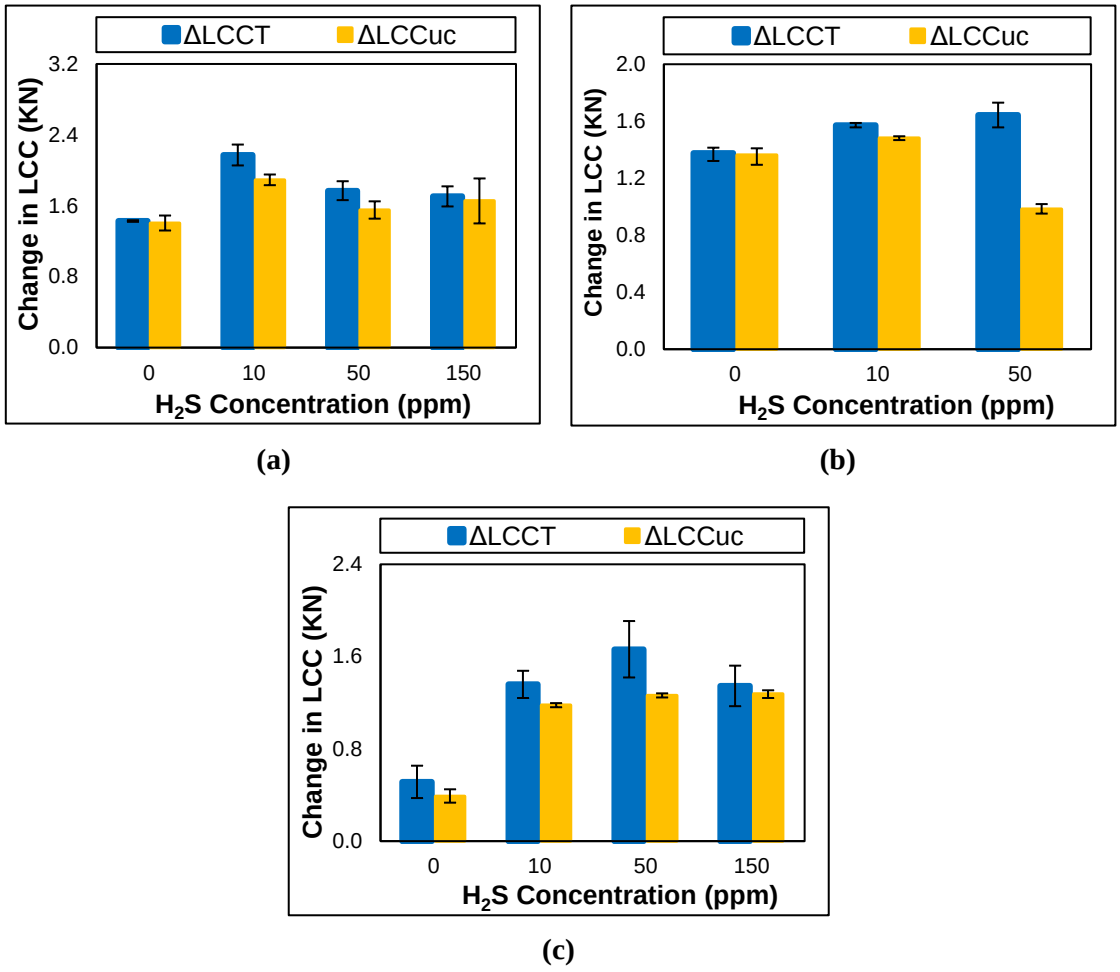

Figure 6.32 ΔLCCT and ΔLCCuc as a function of H_2S concentration for different test materials: a) T95; b) C110; and c) Q125

6.3.3 Effect of Flow Velocity

Figure 6.33 compares change in total load carrying capacity (ΔLCC_T) with change load carrying capacity resulting from uniform corrosion at different rotational speed and temperature (38 and 71°C). Figures 6.33a and 6.33c reveal good agreement between LCC_T and LCC_{uc} for both T95 and Q125, respectively. These results indicate the absence of intergranular damage or localized corrosion during exposure to the test fluid at low temperature (38°C). It should be noticed that minor variation between ΔLCC_T and ΔLCC_{uc} commonly occurs because of slight non-uniformity in corrosion and subsequently thickness reduction (Elgaddafi et al. 2016b). At high temperature (71°C), a substantial discrepancy between ΔLLC_T and ΔLCC_{uc} is obviously observed under dynamic test condition. The abnormal reduction in load carry capacity could be relevant to the occurrence of localized corrosion. The occurrence of pitting/localized corrosion under dynamic condition is consistent with findings of previous studies (Kumar et al. 2013; Li et al. 2014b).

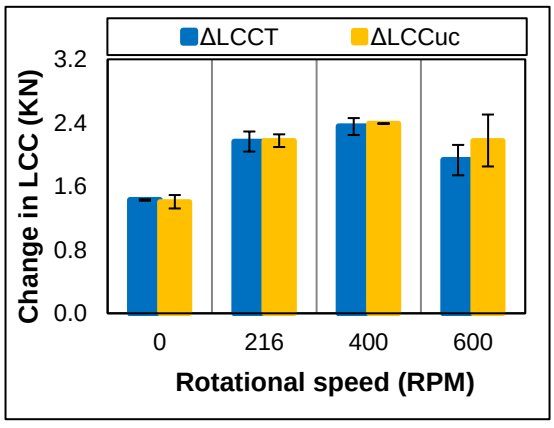

(a)

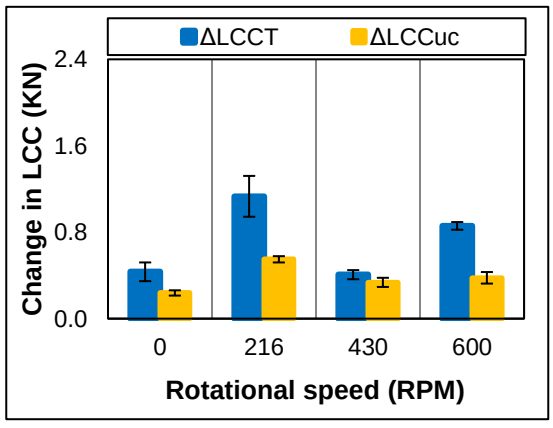

(b)

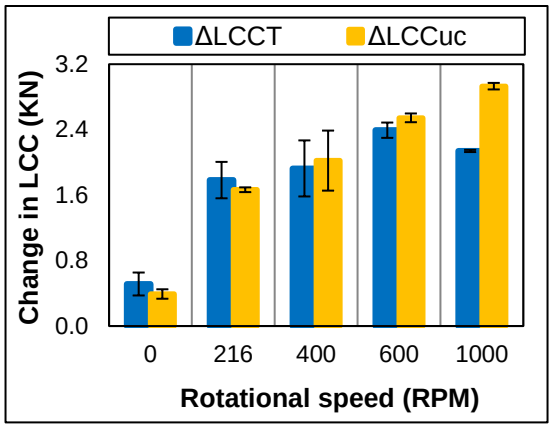

(c)

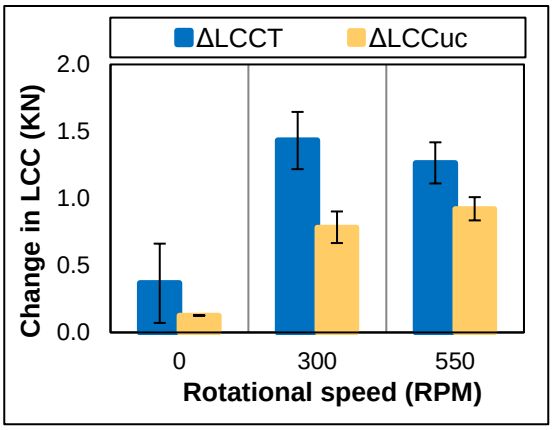

(d)

Figure 6.33 ΔLCCT and ΔLCCuc as a function of rotational speed and temperature for different test materials: a) T95 (38°C); b) T95 (71°C); c) Q125 (38°C) and d) Q125 (71°C)

Chapter 7 : MODEL VALIDATION

In Chapter 4, mathematical models are developed to predict corrosion rate of carbon steel in sweet and sour corrosive environment. To ensure accuracy of the developed models, predictions are compared with experimental measurements generated in this study and other available data in the literature.

7.1 Validation of Electrochemical-Based CO_2 Corrosion Model

The model presented in Section 4.1.1 predicts corrosion rate in CO_2 environments under steady state conditions. Under dynamic condition, an accurate correlation is used to calculate mass transfer coefficient taking into consideration of fluid velocity and flow geometry. The corrosion model is applicable for wide range of CO_2 partial pressures and temperatures. Moreover, the model account for the effect of material type on corrosion rate. To validate the model, its predictions are extensively compared with measurements generated in this study. The experimental data obtained by exposing test specimen to 2% NaCl solution saturated with various concentrations of CO_2 in the gas phase. Figure 7.1 compares model predictions with measurements obtained from weight loss (WL) method at low-pressure (up to 0.83 MPa and 80°C). Model predictions show predominantly reasonable agreement with experimental data. In some cases, measurements are less than model prediction due to formation of protective scale, which hinders the corrosion process. The model does not account for the impact of corrosion scale. Hence, in some cases, considerable discrepancies are observed.

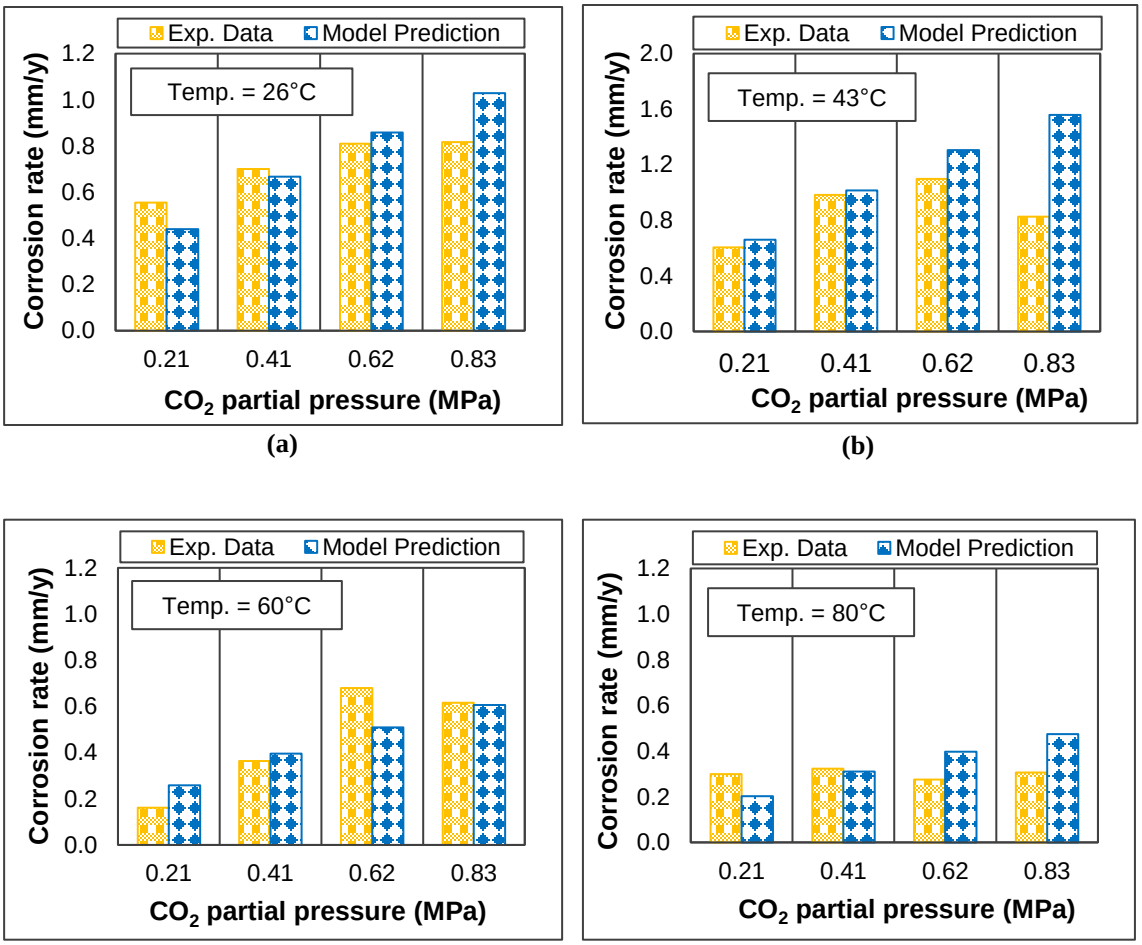

Figure 7.1 Predicted and measured corrosion rate vs. CO_2 partial pressure at various temperatures: a) 26°C, b) 43°C, c) 60°C and d) 80°C

In addition to temperature, flow velocity is considered one of the major variables that has remarkable effect on CO_2 corrosion process. It influences corrosion rate of carbon steel in two ways: i) enhancing mass transport of electro-active species, and ii) interfering in the formation of corrosion sale. To incorporate the flow effect on corrosion phenomena, mass transport term was altered to include both molecular and convective diffusion. Mass-transport coefficient for turbulent flow (k_m) in Eqn. (4.7) is

calculated using correlation of Eisenberg et al. (1954). In order to ensure the accuracy of the model, predictions are compared (Fig. 7.2) with corrosion rate measurements.

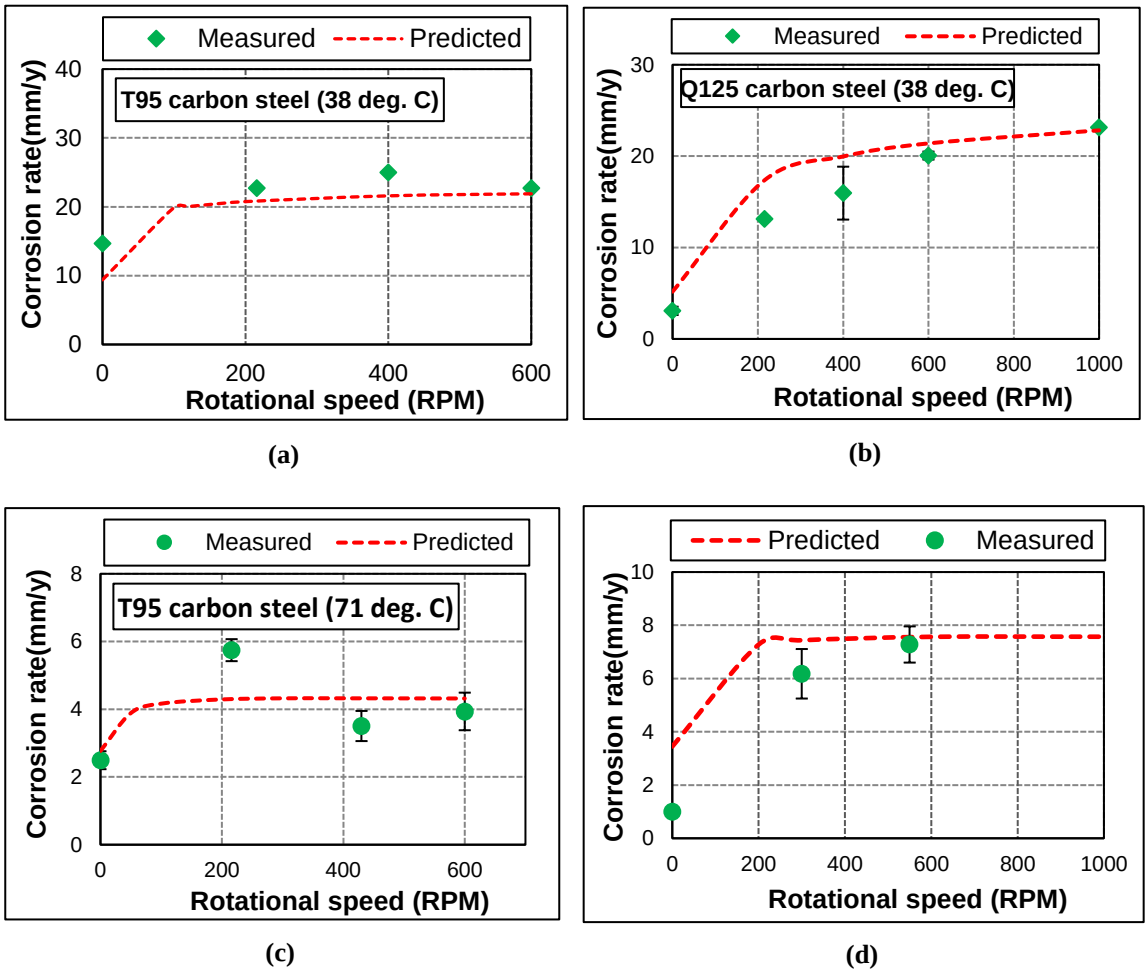

Figure 7.2 Predicted and measured corrosion rate vs. rotational speed at 41.37 MPa: a) T95 at 38°C; b) Q125 at 38°C; c) T95 at 71°C; and d) Q125 at 71°C

Figure 7.2 compares experimental measurements with model predictions for T95 and Q125 grade steels at 41.38 MPa and different temperatures (38 and 71°C). Corrosion rate consistently increased with rotational speed until controlling mechanism changed. At relatively low temperature, the model predictions show predominantly good agreement with the experimental data for two tested materials. Discrepancies are

in the range of 5-7% at high rotational speed. At intermediate temperature (71°C), the corrosion rate trend is similar and the maximum discrepancy is roughly 30%, which is observed at 200 rpm for T95 carbon steel (Fig. 7.2c). The increased discrepancy is attributed to other factors that are not considered in the model formulation. Despite some noticeable discrepancies, in general, the model reasonably captured the corrosion rate trend with rotational speed (Fig. 7.2).

7.2 Validation of Electrochemical-Based CO_2-H_2S Corrosion Model

The severity of CO_2 corrosion could be accelerated or inhibited due presence of H_2S. It essentially depends on environment conditions as well as test material. In this study, corrosion resistance of three different API grade steels was studied at 41.37 MPa and 38°C. Corrosive environment was 2% NaCl solution saturated with mixed gas containing approximately 50% CO_2, 50% CH_4 and various concentrations of H_2S. To ensure model accuracy, its predictions are compared with measurements. Predictions display predominantly reasonable agreement with experimental data (Fig. 7.3). Minor discrepancies exist because of data scattering and model inaccuracy resulting from assumptions and idealizations of real corrosion process, which is complex and difficult to describe fully using a mathematical model.

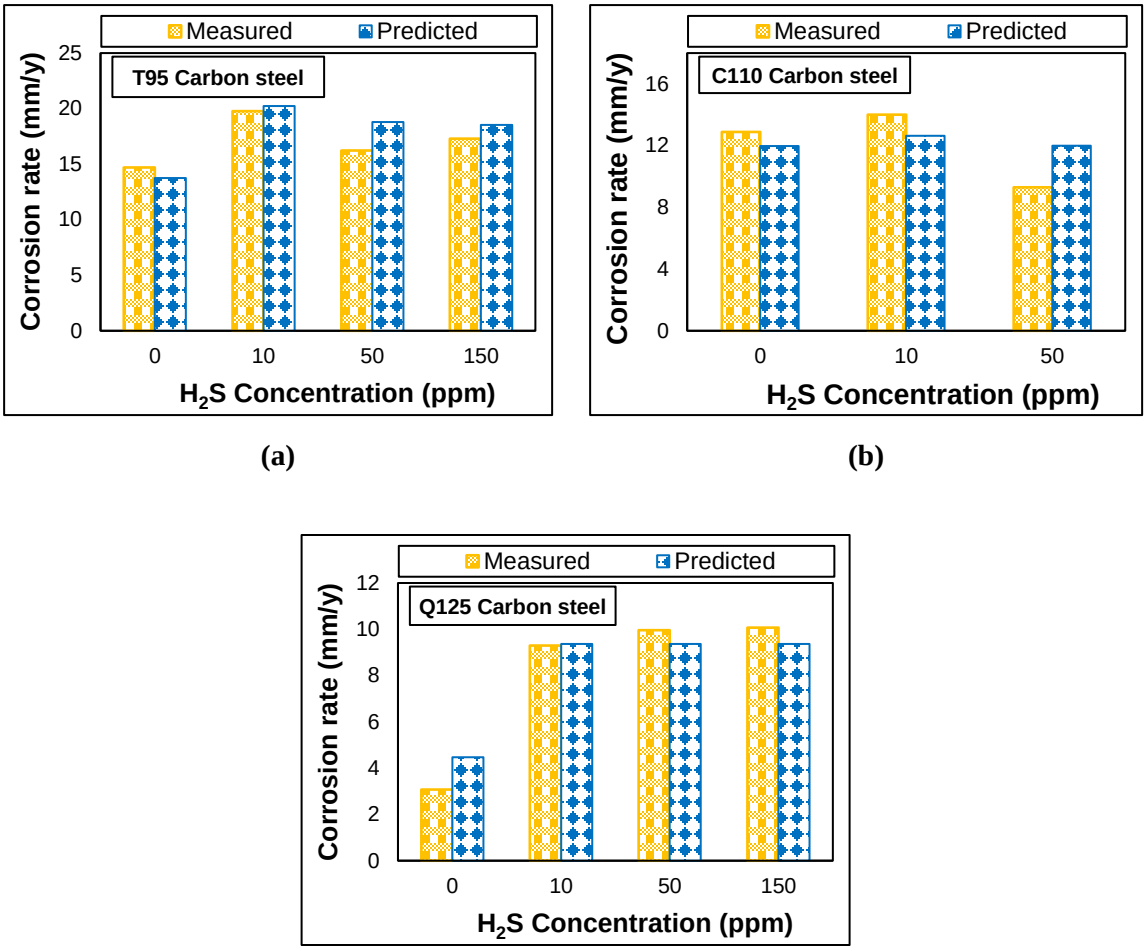

Figure 7.3 Predicted and measured corrosion rate vs. H_2S concentration at 41.37 MPa and 38°C: a) T95; b) C110; and c) Q125

7.3 Mass Transfer-Based CO_2-H_2S Corrosion Model Validation

The CO_2-H_2S corrosion model is improved by incorporating new mathematical model to describe the thermodynamic properties of corrosive gases. To evaluate accuracy of the model, its predictions are extensively compared with published measurements (Kvarekval et al. 2003) and predictions of the original model (Sun and Nesic 2009).

Published measurements are obtained under various H_2S partial pressures and exposure time (Table 7.1).

Table 7.1 Experimental conditions (Kvarekval et al. 2003)

Case No.	Time (h)	T(°C)	Gas Composition	
			P_{CO2} (bar)	P_{H2S} (bar)
A	24	120	6.90	1.38
B	20	120	6.90	2.76
C	138	120	6.90	2.76
D	166	120	6.90	2.76
E	21.5	120	6.90	3.45
F	383	120	6.90	3.45
G	68.5	120	6.90	4.14

Model predictions mostly demonstrate reasonable agreement with measurements with the exception of Case F in which moderate discrepancies are observed (Fig. 7.4). In other cases, the new model slightly under-predicts corrosion rate, even though the original model provided better prediction. In general, the model predictions demonstrate satisfactory agreement with experimental data and original model.

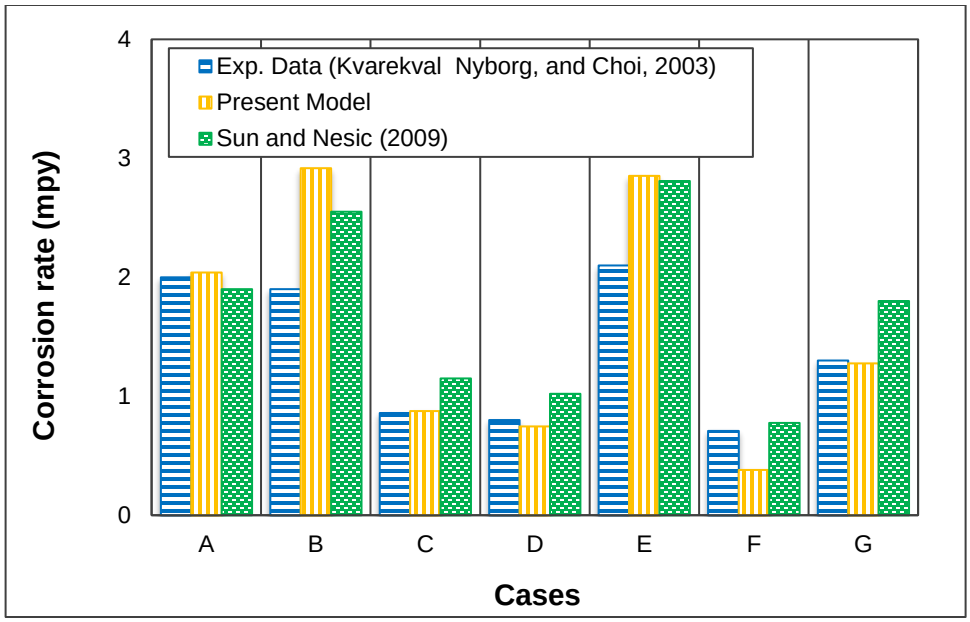

Figure 7.4 Comparison of model predictions with experimental measurements

In Fig. 7.5, model predictions are compared with published data (Omar et al. 2005) and predictions of the original model. The corrosion rate measurements were obtained at elevated temperature and high H_2S concentration (Table 7.2). In this case, the new model displays better accuracy than the original model, which overestimates corrosion rate due to inaccuracy of the Henry's law at high pressures. The original model shows high discrepancy, which reaches up to 100% (Case C). The maximum discrepancy of new model is approximately 50% (Case A). Previous studies (Kumar et al. 2014; Han et al. 2011) reported the overestimation of corrosion rate due to the application of Henry's law for solubility of CO_2 and H_2S under high-pressure.

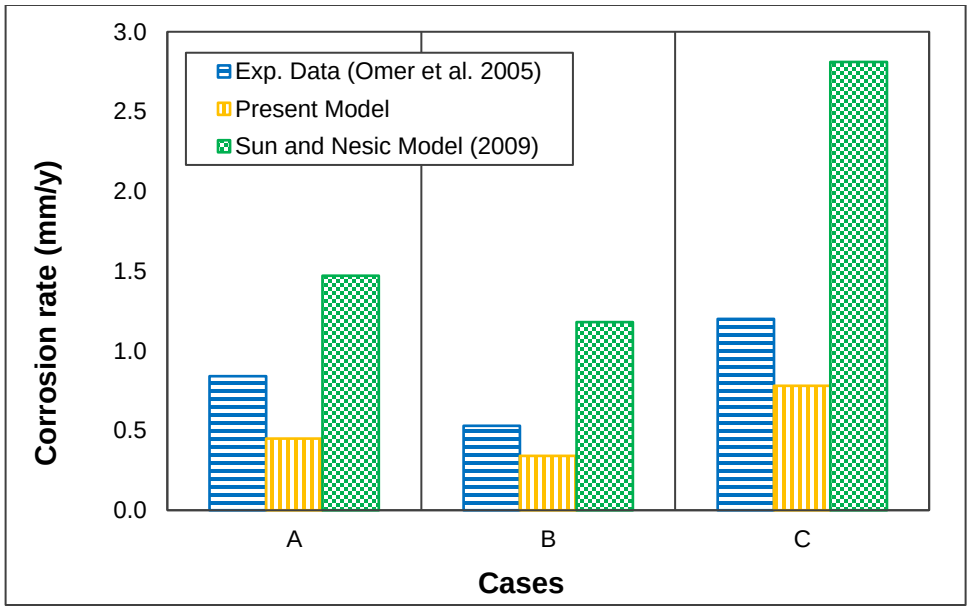

Figure 7.5 Comparison of model predictions with measurements (Omar et al., 2005)

Table 7.2 Experimental conditions (Omer et al. 2005)

Case No.	Time (h)	T(°C)	Gas partial pressure	
			P_{CO2} (bar)	P_{H2S} (bar)
A	456	80	3.30	10.00
B	504	25	3.30	10.00
C	360	80	10.00	30.00

Pressure and temperature have remarkable influence on sour corrosion. To further validate the new model for wide range of pressure and temperature, model predictions are compared (Fig. 7.6) with experimental data presented by Bich and Goerz (1996). The data was obtained at high temperature (65°C) and various CO_2 and H_2S partial pressure ratios (Table 7.3). Moreover, the new model is compared with an existing mechanistic model (Fardisi et al. 2012). Overall, the present model displays better accuracy than the existing model.

Figure 7.6 Comparison of model predictions with experimental measurements (Bich and Goerz 1996)

Table 7.3 Experimental conditions (Bich and Goerz 1996)

Case No.	Time (h)	T(°C)	Gas Composition	
			P_{CO2} (bar)	P_{H2S} (bar)
A	71	60	5.3	3.0
B	91	60	5.3	3.0
C	69	65	3.5	12.2
D	91	65	12.8	8.0
E	63	65	3.0	4.2

Figure 7.7 compares model predictions with published experimental measurements (Zhang et al. 2009b; Zhang et al. 2011; Jingen et al. 2011; Yin et al. 2007; Wen-fei et al. 2012). Generally, model comparison shows reasonable predictions. However, few data points display noticeable scattering. The discrepancies are due to very sensitive nature of corrosion to the formation of protective scale. The

new model is more accurate than the existing model (Sun and Nesic 2009) because its applicability is extended to high pressure (CO_2 and H_2S partial pressure of 3 MPa) and elevated temperature. The model accuracy diminishes outside its application range. Pitting corrosion, which is not considered in the present model formulation, can occur when partial pressure is more than 3 MPa.

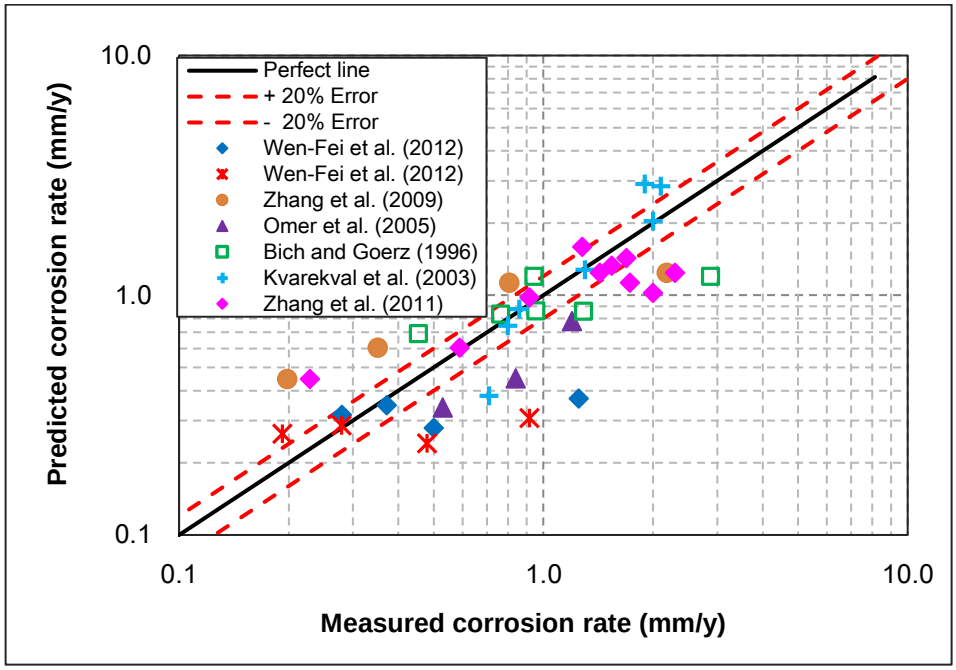

Figure 7.7 Predicted vs. measured corrosion rate under wide range of test conditions

Chapter 8 : CONCLUSIONS AND RECOMMENDATIONS

8.1 Conclusions

8.1.1 Low-Pressure Corrosion Study

Corrosion behavior of 1045 carbon steel in CO_2 environment was investigated at 0.83 MPa and varying temperature, salt content and CO_2 PPR. The corrosion rate was measured using linear polarization resistance and weight loss techniques. A mathematical model has been developed to predict corrosion rate in sweet environment. Based on the results, the following conclusions can be drawn:

- Corrosion in aqueous CO_2 environment is considerably affected by temperature and CO_2 partial pressure in which corrosion rate reduced by averaging of 140% when temperature was elevated from 26 to 80°C at various CPPR. As the temperature increased, the corrosion rate increased until it reached a peak value, and then declined. Regardless of CO_2 partial pressure, the maximum corrosion rate was observed at 43°C.
- Increasing CO_2 partial pressure results in increased concentrations of carbonic acid, and carbonate and iron ions, which accelerate scale formation and subsequently impede corrosion process.
- The impact of CO_2 partial pressure on corrosion rate is strongly influenced by temperature. In absence of corrosion scale, increase in temperature facilitates corrosion reactions and molecular diffusion (transport of species); hence, it

facilitates the corrosion process. However, higher temperatures (greater than 43°C) result in super-saturation of corrosion products and favor formation of corrosion scale.

- Corrosion rate is considerably affected by the salt concentration with or without the presence of carbon dioxide. At CO_2 concentration less than 50%, CO_2 corrosion rates significantly (roughly by 50%) decreases with the increase in the salt concentration. The influence of salt concentration on the corrosion is less dependent on temperature than CO_2 concentration.
- Corrosion rate predictions of the electrochemical-based model show reasonable agreement with experimental measurements obtained under low-pressure.

8.1.2 High-Pressure Corrosion Study

An extensive experimental investigation has been conducted on corrosion behavior of API carbon steels (T95, C110, and Q125) under high-pressure condition. Experimental variables were pressure, temperature CO_2 and H_2S contents in the gas phase, and flow condition. The electrochemical-based CO_2 corrosion model has been extended to account for presence of hydrogen sulfide and fluid flow effect. Subsequently, experimental results are used to validate model predictions under static and dynamic conditions. Based on the experimental results and theoretical analysis, the following conclusions can be drawn:

- Presence of CO_2 in corrosive environment exacerbates corrosion of API grade carbon steels. CO_2 partial pressure ratio, pressure and type of protective scale have strong impact on corrosion behavior of API carbon steel.
- Presence of small amount of H_2S (less than 10 ppm) generally promotes corrosion process in brine saturated with mixed gas containing methane and CO_2.
- Both temperature and fluid velocity have very strong influence on corrosion of API grade steels. Corrosion of API steels significantly reduced with temperature. The maximum corrosion rate was observed at 38°C. Furthermore, corrosion of the materials remarkably increased with fluid flow.
- Under the test conditions considered in this research, Q125 carbon steel mostly exhibited superior resistance to sweet corrosion.

- C110 and Q125 carbon steels demonstrated considerable susceptibility for localized corrosion when test specimen exposed to CO_2-H_2S containing environment under dynamic condition. Mechanical property measurements indicated occurrence of other types of corrosion with C110 and Q125 when the materials exposed to test fluid with 50 ppm H_2S at 71°C and dynamic condition (above 300 rpm).

- Uniform corrosion is the main mechanism for CO_2 corrosion of C110 at 38°C and high-pressure condition. Results show absence of localized corrosion that can cause strength degradation. Even though mechanical strength is

predominately preserved after exposure to CO_2-brine environment, carrying capacity of a corroded metal diminishes largely due to material loss.

- In absence of CO_2, T95 carbon steel exhibits relatively high corrosion, which is roughly 10 mm/y at 41.37 and 38°C.
- Predictions of electrochemical-based corrosion models are in good agreement with experimental data obtained under HPHT static and dynamic conditions for both sweet and sour environments.

8.2 Recommendations

Even though desired objectives have been successfully achieved in this investigation, other corrosion complexities need to be investigated to improve our understanding and prediction of sweet and sour corrosion in harsh environments. Thus, the following is recommended:

- More advanced theoretical work is encouraged to study CO_2 corrosion phenomena of carbon steel under unsteady state condition. In spite of complexity, it is important to include corrosion scale influence in the mathematical models.
- In this study, corrosion rate measurements were limited to relatively low NaCl concentration (2 wt %). It is recommended to investigate the effect of salt concentration on corrosion rate at high NaCl content. Moreover, it is better to include other salts such as $CaCl_2$ and KCl in the test solution to simulate produced water in the field.

- Solution pH is a critical factor affecting corrosion rate. It is highly recommended to measure instantaneous pH during the corrosion test.
- The use of other technical methods including linear polarization resistance and potential dynamic sweep techniques to measure corrosion rate at HPHT is recommended in order to have a better understanding of CO_2 corrosion mechanism and learn how it is affected by test variables.
- It is recommended to analyze various types of corrosion scale formed on specimen surface using scanning electron microscopy (SEM) and X-ray diffraction (XRD) techniques.
- In this study, dynamic corrosion test is limited to single-phase flow. It is recommended to study the impact of multi-phase flow on the corrosion behavior of carbon steels (supercritical CO_2).
- The severity of CO_2 corrosion has been extensively investigated under HPHT condition. It is recommended to study corrosion protection by adding chemical inhibitors and/or modify chemical composition of the metal.

REFERENCES

Aagotnes, N.O., Hernmingsenl, T., Haarseth, C., Midttveitt, I. 1999. Comparison of corrosion measurements by use of AC-impedance, LPR and polarization methods on carbon steel in CO_2 purged NaCl electrolytes, presented at the NACE Corrosion/99 conference, San Antonio, Texas, 25-30 April, Paper No. 99027.

Abayarathna, D., Naraghi, A., and Wang, S. 2005. The Effect of Surface Films on Corrosion of Carbon Steel in a CO_2-H_2S-H_2O System, Houston, TX., April 3 - 7, Paper No. 624.

Abelev, E., Ramanarayanan, T. A., Bernasek, S. L. 2009. Iron Corrosion in CO2/Brine at Low H_2S Concentrations, J. Electrochem. Sci. 156 (9): C331-C339.

Addis, J., Brown, B., and Nesic, S. 2008. Erosion-Corrosion in Disturbed Liquid/Particle Flow, Presented at Corrosion/08 conference, Houston, TX, 6-20 March, Paper No. 08276.

Agrawal, A.K., Durr, C., and Koch, G.H., 2004. Sulfide Films and Corrosion Rates of AISI 1018 Carbon Steel in Saline Solutions in the Presence of H2S and CO2 at Temperatures up to 175°F, Presented at the Corrosion/04 conference, New Orleans, LA, 28 March-1 April, Paper No.383.

Anderko, A. M. and Young, R. D. 1999. Simulation of CO2/H2S corrosion using thermodynamic and electrochemical models, presented at the NACE Corrosion/99 conference, San Antonio, Texas, 25-30 April,Paper No. 31.

Anderko, A. and Young, R. D. 2002. A Model for Calculating the Rates of General Corrosion of Carbon Steel and 13%Cr Stainless Steels in CO2/H2S Environments, March 11 -16, Houston, Tx.

Anderko, A. and P. J. Shuler, 1999. Modeling the formation of iron sulfide scales using thermodynamic simulation software, Presented at the NACE international conference, Corrosion/99, San Diego, California, 22-27 March, Paper No.64.

Anderko, A., 2000. Simulation of $FeCO_3$/FeS scale formation using thermodynamic and electrochemical models. Presented at the NACE international conference, Corrosion/00, Orlando, Florida, Orlando, Florida, 26-31 March, Paper No.102.

Asmara, Y.P. and Ismail, M.C. 2011. Study combinations Effects of HAc in H_2S/CO_2 Corrosion, Journal of Applied Sciences 11 (10):1821.

ASTM E 8M-98, 2009, Standard test Methods for flat bar tensile testing of metallic materials.

ASTM G1, 1999, Standard practice for preparing, cleaning, and evaluation corrosion test specimens.

ASTM G111-97, 2013, Standard Guide for Corrosion Tests in HTHP Environment.

Azo materials. 2012. AISI 1045 Medium Carbon Steel, http://www.azom.com/article, (Accessed 11 August 2015).

Barta, L. and Bradley, D. J. 1985. Extension of the specific interaction model to include gas solubilities in high temperature brines, Geochim. Cosmochim. Acta 49,195.

Ben-Naim, A., Yaacobi, M., 1974. Effects of solutes on the strength of hydrophobic interaction and its temperature dependence. J. Phys.Chem. 7 (2), 170–175.

Bich, N.N., and Goerz, K. 1996. Caroline pipeline failure: finding on corrosion mechanism in wet sour gas systems containing significant CO_2, Presented at the NACE international conference, Corrosion/96, Denver, Colorado, 24-29 March, Paper No. 26.

Blount, C.W., Price, L.C. 1982. Solubility of methane in water under natural conditions: A laboratory study; DOE Contract No. DE-A508-78ET12145, Final Report.

Bockris, J.O.M., Drazic, D. and Despic, A.R. 1961. The Electrode Kinetics and Dissolution of Iron, Electrochimica Acta 4 (2-4), 325 - 361.

Bonis, M. R., Girgis, M., Goerz, K., and MacDonald, R. 2006. Weight loss corrosion with H_2S: using past operations for designing future facilities, Presented at the NACE international conference, Corrosion/06, San Diego, CA., 12-16 March, Paper No.122.

Brown, B., Nesic, S. and Parakala, S. R. 2004. CO_2 corrosion in the presence of trace amounts of H_2S. Presented at the NACE international conference, Corrosion/04, New Orleans, Louisiana, 28 March-1 April, Paper No. 736.

Brown, B. N., Nesic, S. 2005. CO_2/H_2S Corrosion under Scale Forming Conditions, presented at the NACE Corrosion/05 conference, Houston, TX., 3-7 April, Paper No.625.

Cabrini, M., Lorenzi, S., Pastore, T., and Radaelli, M. 2104. Corrosion Rate of High CO_2 Pressure Pipeline Steel for Carbon Capture Transport and Storage, La Metallurgia Italiana (6).

Camacho, A., Singer, M., Brown, B., and Nesic, S. 2008. Top of the Line Corrosion in H_2S/CO_2 Environments, Presented at the Corrosion/05 conference, New Orleans, Louisiana, 16-20 March, Paper No. 470.

Carroll, J.J., Mather, A.E., 1989. Phase Equilibrium in the system water-hydrogen sulfide: experimental determination of the LLV Locus, Can. J. Chem. Eng. 67 (1989) 468–470.

Chapoy, A., Coquelet, C., and Richon, D. 2005. Corrigendum to “Revised solubility data and modeling of water in the gas phase of the methane/water binary system at temperatures from 283.08 to 318.12 K and pressures up to 34.5 MPa, Fluid Phase Equilibr. 230 (1-2): 210–214.

Chen, T. Y.,Moccari, A. and MacDonald, D. D. 1992. The Development of Controlled Hydrodynamic Techniques for Corrosion Testing. Corrosion 48(3).

Chen, Y., Hong, T., and Jepson, W. P. 2000. EIS Studies of a Corrosion Inhibitor Behavior under Multiphase Flow Conditions, Corros. Sci. 42 (6): 979-990.

Chen, C., Lu, F., Sun, M.X., Zhang, D.B., Chang, Z.H.W. 2005a. Effect of chromium on the pitting resistance of oil tube steel in a carbon dioxide corrosion system, Corrosion 61(6):594-601.

Chen, Y.Y., Tzeng, H.J., Wei, L.I., and Shih, H.C. 2005b. Mechanical properties and corrosion resistance of low-alloy steels in atmospheric conditions containing chloride, Mater. Sci. and Eng. 398(1-2): 47–59.

Chen, B.Q., and Garbatov Soares, Y.C. G., 2012. Mechanical properties assessment of specimens subjected to random on-uniform general corrosion and tensile load, Mari. Eng. Tech., London, ISBN 978-0-415-62146-5.

Choi Y.S., and Nesic, S. 2011a. Determining the Corrosive Potential of CO_2 Transport Pipeline in High P_{CO2}–Water Environments, J. Greenhouse Gas Control 5 (4): 788–797.

Choi, Y.S., Nesic, S., and Ling, S. 2011b. Effect of H_2S on the CO_2 corrosion of carbon steel in acidic solutions, Electrochimica Acta 56 (4):1752-1760.

Choi, Y.S., Farelas, F., Nesic, S., Magalhães, A.A.O., and de Azevedo Andrade, C. 2013. Corrosion Behavior of Deep Water Oil Production Tubing Material under Supercritical CO_2 Environment: Part I. Effect of Pressure and Temperature, Presented at the Corrosion/13 conference, Orlando Florida, 17-21 March, Paper No. 2380.

Choi, Y.S., Hassani, S., Vu, T.N., Nesic, S., and Abas, A. Z. B. 2015. Effect of H_2S on the Corrosion Behavior of Pipeline Steels in Supercritical and Liquid CO_2 Environments, Presented at the NACE corrosion/15 conference, Dallas, Texas, 15-19 March, Paper No. 5927.

Crolet, J., Thevenot, N., and Nesic, S. 1998. Role of Conductive Corrosion Products in the Protectiveness of Corrosion Layers, Corrosion, 54(3).

Cui, Z.D., Wu, S.L., Zhu, S.L., and Yang, X.J.2006. Study on Corrosion Properties of Pipelines in Simulated Produced Water Saturated with Supercritical CO_2, J. App. Surf. Sci. 252 (6): 2368–2374.

Cui, Z.D., Wu, S.L., Li, C.F., Zhu, S.L., Yang, X.J. 2004. Corrosion behavior of oil tubesteels under conditions of multiphase flow saturated with super-critical carbon dioxide, Mater. Lett. 58 (6):1035-1040.

Das, G.S., Khanna, A.S., 2004a. Parametric Study of CO_2/H_2S Corrosion of Carbon Steel Used for Pipeline Application, international Symposium of Research Students on Materials Science and Engineering, Chennai, India.

Das, G.S., Khanna, A.S., 2004b. Corrosion behavior of pipeline steel in CO_2 environment, Trans. Indian Inst. Met. 57, 277-281.

Das, G.S., 2014. Precipitation and Kinetics of Ferrous Carbonate in Simulated Brine Solution and its impact on CO_2 corrosion of steel, Inter. J. Adv. Eng. Tech. 7 (3): 790-797.

Dayalan, E., Vani, G., Shadley, J., Shirazi, R. S. A., Rybicki, E. F., 1995. Modeling CO_2 Corrosion of Carbon Steels in Pipe Flow, Presented at the NACE Corrosion/95 conference, Houston, TX., Paper No.118.

Dayalan, E., de Moraes, F. J., Shadley, R., Shirazi, S., Rybicki, A. E. F. 1998. CO_2 Corrosion Prediction in Pipe Flow under $FeCO_3$ Scale-Forming Conditions, Presented at the NACE Corrosion/98 conference, San Diego, Ca., 22-27 March, Paper No.51.

De Waard, C., Milliams, D.E., 1975a. Carbonic acid corrosion of steel, Corrosion 31, 177–181.

De Waard, C., Milliams, D.E., 1975b. Prediction of carbonic acid corrosion in natural gas pipelines, Presented at the Internal and External Protection of Pipes, F1–1–F1–8.

De Waard, C., and Lotz, U. 1993. Prediction of CO_2 Corrosion of Carbon Steel, Presented at Corrosion/93 conference, Houston, TX., Paper No. 69.

De Waard, C., Lotz, U., Dugstad, A., 1995. Influence of liquid flow velocity on CO_2 corrosion: A semi-empirical model, in: NACE International, Paper No. 128.

Denpo, K. and Ogawa, K. 1993. Fluid flow effects on CO_2 corrosion resistance of oil well materials, Corrosion, 49 (6), 442-449.

Duan, Z., and Sun, R. 2003. An improved model calculating CO_2 solubility in pure water and aqueous NaCl solutions from 273 to 533 K and from 0 to 2000 bar, Chem. Geol., 193 (3-4): 257 – 271.

Duan, Z. and Mao, S. 2006. A thermodynamic model for calculating methane solubility, density and gas phase composition of methane-bearing aqueous fluids from 273 to 523 K and from 1 to 2000 bar, Geochim. Cosmochim. Acta, 70 (13): 3369–3386.

Duan, Z., Sun, R.,Liu, R., and Zhu, C. 2007. Accurate thermodynamic model for the calculation of H_2S solubility in pure water and brines, Energy Fuels, 21 (4): 2056-2065.

Dugstad, A., 1992. The importance of FeCO3 Super Saturation of Carbon Steel, Paper No.14, presented at the Corrosion/92 conference, Houston, Tx.

Dugstad, A., Lunde, L., and Videm, K., 1994. Parametric Study of CO_2 Corrosion of Carbon Steel, NACE, Houston, TX, 28 Feb - 4 Mar., Paper No.14.

Dugstad, A., 1998. Mechanism of Protective Formation during CO_2 Corrosion of Carbon Steel, Presented at the Corrosion/98 conference, San Diego, Calif., 22-27 March, Paper No.031.

Eisenberg, M., Tobias, C.W., Wilke, C.R. 1954.Ionic Mass Transfer and Concentration Polarization at Rotating Electrodes, J. Electrochem. Soc.101 (6):306.

Elgaddafi, R., Ahmed R., Shah, S., 2016a. Modeling CO_2-H_2S Corrosion of Tubular at Elevated Pressure and Temperature, Research Journal of Applied Sciences, Engineering and Technology, 13(7): 510-524.

Elgaddafi, R., Ahmed, R., Hassani, S., Shaha, S., Osisanyaa, S. O., 2016b. Corrosion of C110 Carbon Steel in High-Pressure Aqueous Environment with mixed Hydrocarbon and CO_2 Gas, J. Pet. Sci. Eng. 146:777–787.

Elgaddafi, R., Naidu, A., Ahmed, R., Shah, S., Hassani, S., Osisanya, S. O., Saasen, A., 2015. Modeling and experimental study of CO_2 corrosion on carbon steel at elevated pressure and temperature, J. Nat. Gas Sci. Eng. 27(3):1620-1629.

Fang, H., Nesic, S., Brown, B. N., Wang, S. 2006, General CO_2 Corrosion in High Salinity Brines, Presented at Corrosion/06 conference, San Diego, California,12-16 March, Paper No.372.

Fang, H., Brown, B., and Nesic, S. 2010. High salt concentration effects on CO_2 corrosion and H_2S corrosion, Presented at the NACE international conference, Corrosion/10, San Antonio, Texas, 14-18 March, Paper No. 276.

Fardisi, S., Tajallipour, N., Teevens, P.J. 2012. Predicting general corrosion rates in sour environments with the growth of a protective iron sulphide film, Paper No.1471, Presented at the NACE Corrosion/2012 conference, Salt Lake City, Utah.

Forero, A. B., Milagros, M.G., and Núñez, I. S. B. 2014. Analysis of the Corrosion Scales Formed on API 5L X70 and X80 Steel Pipe in the Presence of CO_2, J. Materials Research 17(2), 461-471.

Foroulis, Z. A., 1980. Electrochemical behavior and corrosion of iron in aqueous sulfidic solution, Materials and Corrosion, 31 (6): 463–470.

Fosbøl, P.L., Thomsen, K., Stenby, E. H., 2009. Improving mechanistic CO_2 corrosion Models, Presented at the Corrosion/09 conference, Atlanta, Georgia, 22-26 March, Paper No.561.

Gray, L.G.S., Anderson, B.G., Danysh, M.J., Tremaine, P.R., 1989. Mechanisms of Carbon Steel Corrosion in Brines Containing Dissolved Carbon Dioxide at pH 4, Presented at the Corrosion/89 conference, Houston TX., Paper No. 464.

Gray, L.G.S., Anderson, B.G., Danysh, M.J., Tremaine, P.R. 1990. Effect of pH and temperature on the mechanism of carbon steel corrosion by aqueous carbon dioxide, Presented at the corrosion/90 conference Houston, TX., Paper No. 40.

Garbatov, Y., Guedes Soares, C., Parunov, J., Kodvanj, J. 2014. Tensile strength assessment of corroded small scale specimens, Corr. Sci., 85, 296–303.

Gulbrandsen E., Nesic, S., Stangeland, A., Buchardt, T., Sundfaer, B., Hesjevik S. M., Skjerve S. 1998 .Effect of precorrosion on the performance of inhibitors for CO_2 corrosion of carbon steel, Presented at CORROSION/1998 conference, Houston, TX., 22-27 March, Paper No. 013.

Han J., Carey J. W., and Zhang J. 2011. Effect of sodium chloride on corrosion of mild steel in CO_2-saturated brines, J. Appl. Electrochem., 41 (6): 741–749.

Hassani, S., Vu, T.N., Rosli, N.R., Esmaeely, S.N., Choi, Y.S., Young, D., and Nesic, S. 2014. Wellbore integrity and corrosion of low alloy and stainless steels in high pressure CO_2 geologic storage environments: an experimental study, Int. J. Greenh. Gas Control, 23: 30–43.

Hassani, S., Roberts K.P., Shirazi S.A., Shadley J.R., Rybicki E.F., and Joia C. 2011. Flow Loop Study of Chloride Concentration Effect on Erosion, Corrosion and Erosion-Corrosion of carbon Steel in CO_2Saturated Systems, Presented at the Corrosion/11 conference, Houston, TX., 13-17 March, Paper No.237.

Harvey, A.H., and Prausnitz, J.M. 1989. Thermodynamics of high-pressure aqueous systems containing gases and salts, AIChE J. 35(4), 635– 644.

Hernandez, J., Munoz, A., Genesca, J. 2012. Formation of iron-carbonate scale-layer ~ and corrosion mechanism of API X70 pipeline steel in carbon dioxide saturated 3% sodium chloride, Corrosion, 10:251–258.

Hershey, J. P., Tinka, P. and Millero, F.J. 1988. The pK_1* for the dissociation of H_2S in various ionic media, Geochim. Cosmochim. Acta, 52 (8):2047-2051.

Holmes H.F., Busey, R.H. Simonson J.M., and Mesmer R.E. 1987. The enthalpy of dilution of $HCl_{(aq)}$ to 648 K and 40 MPa thermodynamic properties, J. Chem. Therm. 19 (8): 863-890.

Hu, H., Zhang, L., Chang, W., Lu, M., Xu, L. 2011. Compare the Corrosion Resistance of 3% Cr Steel with API X65 Pipeline Steel in CO_2 Corrosion Environment, presented at the Corrosion/11 conference, Houston, TX., 13-17 March, Paper No.073.

Huang, J., Guraieb, P., Yan, C., Contreras, E., Tomson, M., and Tomson, 2014. Corrosion Behavior of Deepwater Oil Production Tubing Materials under Extremely High Temperature and High Pressure, Presented at the Offshore Technology Conference, Houston, TX, 5-8 May, Paper No. 25193.

Hudak, P.F. and Wachal, D.J. 2001. Effects of brine injection wells, dry holes, and plugged oil/gas wells on chloride, bromide, and barium concentrations in the Gulf Coast Aquifer, southeast Texas, USA, Environment International, 26(7-8): 497-503.

Ikeda, A., Mukai, S., and Ueda, M. 1985. Corrosion Behavior of 9% to 25% Cr Steels in Wet CO_2 Environments, J. Corros. Sci., 41(4): 185-192.

Ikeda, A., Ueda, M., and Mukai, S. 1984. CO_2 Corrosion Behavior and Mechanism of Carbon Steel and Alloy Steel, Corros. Sci. 83, Houston, TX.

Ikeda, A., Ueda, M., and Mukai, S. 1985. Influence of Environmental Factors on Corrosion in CO_2 Source Well, Presented at the Technical Symposia - Corrosion 85, Houston, TX.

Jangama, V.R., Srinivasan, S., 1997. A Computer Model for Prediction of Corrosion of Carbon Steels, Presented at the Corrosion/97 conference, New Orleans, Louisiana, 9-14 March, Paper No. 318.

Jepson, W.P., Bhongale, S., 1995. Effect of Pressure, Temperature and Oil Composition on Corrosion Rate in Horizontal Multiphase Slug Flow, NSF, I/UCRC Corrosion in Multi-Phase Systems Center, Department of Chemical Engineering, Ohio University.

Jingen, D. Wei, Y., and Xiaorong, L., 2011. Influence of H_2S Content on CO_2 Corrosion Behaviors of N80 Tubing Steel, J. Petro. Sci. and Tech. 29: 387-1 396.

Jinsen, Q., Changfeng, C., Shuqi, Z., and Yongji, W. 2011. Effect of partial pressure ratio H_2S/CO_2 on mechanical properties of 3Cr oil tube steel, Materials for Renewable Energy & Environment (ICMREE), Shanghai.

Jia, Z., Li, X., Du, C., Liu, Z., and Gao, J. 2012. Effect of the Carbon Dioxide Pressure on the Electrochemical Behavior of 3Cr Low Alloyed Steel at High Temperature, J. M. Chem. and Ph., 136: 973 – 979.

Jiang X. and Nesic, S.2009. The Role of Cl^- on Localized CO_2 Corrosion and the Effect of Electrode Size on Electrochemical Noise Measurements, 215th ECS Meeting, Abstract No.685, The Electrochemical Society.

Johnson M. L., and Tomson, M. B. 1991. Ferrous Carbonate Precipitation Kinetics and its Impact CO_2 Corrosion, Presented at the Corrosion/91 conference, Houston, TX., Paper No. 268.

Kahyarian, A., Singer, M., and Nesic S. 2015. Modeling of Uniform CO_2 Corrosion of Mild Steel in Gas Transportation Systems: A Review, J. Nat. Gas Sci. and Eng., 29,530–549.

Kermani, M.B., Gonzales, J.C., Linne, C., Dougan, M., and Cochrane, R. 2001. Development of Low Carbon Cr–Mo steels with Exceptional Corrosion Resistance for Oilfield Applications, Presented at the Corrosion/01 conference, Houston, TX., 11-16 March, Paper No. 065.

Kermani, M. B., Morshed, A. 2003. Carbon Dioxide Corrosion in Oil and Gas Production- A Compendium, Corrosion 59, 659.

Kermani, B., Gonzales, J. C., Turconi, G. L., Perez, T. E., Morales, C. 2004. In-Field Corrosion Performance of 3%Cr Steels in Sweet and Sour Downhole Production and Water Injection,Presented at the Corrosion/04 conference, New Orleans, La.,28 March-1 April, Paper No. 111.

Kittel,J., Ropital, F. , Grosjean, F., Sutter, E.M.M., Tribollet, B. 2013. Corrosion mechanisms in aqueous solutions containing dissolved H2S. Part 1: Characterization of H_2S reduction on a 316L rotating disc electrode, Corros. Sci. 66: 324-329.

Kimura, M., Kataoka, Y., and Nakano, Y. 1996. Sulfide Stress Corrosion Cracking Resistance of Low Cr Steel, Presented at the Corrosion/96 conference, Denver, Colorado, 24-29 March, Paper No.60.

Kumar, A., Pacheco, J. L.,Desai, K.S. Huang, W.,Reddy, V. R.,Sun, W., and Haarseth, A. C. 2014. Selecting representative laboratory test conditions for mildly sour sulfide stress corrosion (SSC) testing, Presented at the Corrosion/14 conference, San Antonio, TX.,9-13 March, Paper No. 4243.

Kvarekval, J., Nyborg, R., Seiersten, M. 2002. Corrosion Product Films on Carbon Steel in Semi-Sour CO_2/H_2S Environments, Presented at the Corrosion/02 conference, Denver, Co., 7-11 April, Paper No. 296.

Kvarekval, J., Nyborg, R. and Choi, H. 2003. Formation of multilayer iron sulfide films during high temperature CO_2/H_2S corrosion of carbon steel, Presented at the Corrosion/03 conference, San Diego, California, 16-20 March, Paper No.339.

Lee, K.L., and Nesic, S. 2005. A Mechanistic Model for CO_2 Corrosion of Mild Steel in the Presence of H2S Accompanied by Simultaneous Iron Carbonate and Iron Sulfide Film Growth, Presented at the 16th International Corrosion Congress, Chinese Society for Corrosion and Protection, Beijing, China.

Lee, K.-L. J., Nesic, S. 2005. The Effect of Trace Amount of H_2S on CO_2 Corrosion Investigated by Using the EIS technique, Presented at the Corrosion/05 conference, Houston, TX., 3-7 April, Paper No.630.

Li, Y., and Ngheim, L.X. 1986. Phase equilibria of oil, gas and water/brine mixtures from a cubic equation of state and Henry's law. Can. J. Chem. Eng. 64: 486– 496.

Li, D., Zhang, L., Ma, W., Lu M., Han D., and Wang, L. 2013a. Effects of Temperature on CO_2 Corrosion of Tubing and Casing Steel, Presented at the Corrosion/13 conference, Orlando, Florida, 17-21 March, Paper No.2426.

Li, C., Desai, S.,Pacheco, J.,Cao, F. and Ling, S. 2013b. Effect of sodium chloride concentration on carbon steel sour corrosion, Presented at the Corrosion/13 conference, Orlando, Florida, 17-21 March, Paper No. 2486.

Li, D., Zhang, L., Yang, J., M. Lu, J. Ding, Liu, M., 2014a. Effect of H_2S concentration on the corrosion behavior of pipeline steel under the coexistence of H_2S and CO_2, Int J Miner Metall Mater, 21, 388–394.

Li, C., Xiong, Y.,Pacheco, J. L.,Cao, F.,S.,Desai, K.,Ling, S. 2014b. Effect of wall shear stress on sour corrosion of carbon steel. Presented at the Corrosion/14 conference, San Antonio, TX., 9-13 March, Paper No.4051.

Liu, X., Zheng, Y. G., Okafor, P. C. 2009. Carbon dioxide corrosion inhibition of N80 carbon steel in single liquid phase and liquid/particle two-phase flow by hydroxyethyl imidazoline derivatives, Mater Corros. 60: 507–513.

Liu, Q., Mao, L., Zhou, S. 2014. Effects of chloride content on CO_2 corrosion of carbon steel in simulated oil and gas well environments, Corr. Sci. 84: 165–171.

Liu, W., Lu, S.L., Zhang, Y., Fang, Z.C., Wang, X.M., and Lu, M.X. 2015. Corrosion performance of 3%Cr steel in CO_2-H_2S environment compared with carbon steel Mater. Corros. Sci. 66 :1232–1244.

Liu, Z., Gao, X., Li, J. et al., andWuhan, J. 2016. Corrosion behavior of low alloy pipeline steel in saline solution saturated with supercritical carbon dioxide Univ. Technol.-Mat. Sci. Edit. 31.

Ma, H., Xiaoliang, C., Guiqiu, L.,Chena, S., Quana, Z., Zhaoa, S., Niua, L. 2000. The Influence of Hydrogen Sulfide on Corrosion of Iron under Different Conditions, Corros. Sci. 42: 1669.

Ma HY., Yang, C., Li, G.Y., Guo, W.J.,Chen, S.H.,Luo J.L. 2003. Influence of nitrate and chloride ions on the corrosion of iron, Corrosion, 59:1112.

Mao, S., and Duan, Z. 2006. A thermodynamic model for calculating nitrogen solubility, gas phase composition and density of the N_2–H_2O–NaCl system, Fluid Phase Equilib. 248:103-114.

Masamura, K., Hashizume, S., Sakai, J. et al. 1987. Polarization Behavior of High-Alloy Octg in CO_2 Environment as Affected by Chlorides and Sulfides, J. corr. Sci.43 (6): 359.

Masamura, K., Hashizume, S., Inohara, Y., Minami, Y.1999. Estimation Models of Corrosion Rate of 13% Cr Alloys in CO_2 Environments, Presented at the Corrosion/99 conference, San Antonio, TX., 25-30 April, Paper No.583.

Meyssami, B., M.O. Balaban, and A.A. Teixeira, 1992. Prediction of pH in model systems pressurized with carbon-dioxide, Biotechnol. Prog., 8:149–154.

Millero, F. J. 1986. The thermodynamics and kinetics of the hydrogen sulfide system in natural waters, Mar. Chem., 18:121-147.

Millero, F., Huang, F.,Graham, T., and Pierrot, D. 2007. The dissociation of carbonic acid in NaCl solutions as a function of concentration and temperature, Geochim. Cosmochim. Acta 71:46–55.

Mishra, B., Olson, D. L., Al-Hassan, S., Salama, M. M. 1992. Physical Characteristics of Iron Carbonate Scale Formation in Line Pipe Steels, Presented at the Corrosion/92 conference Houston, TX, Paper No. 13.

Mohamed, M. F., Mohamed Nor, A.,Suhor, M. F.,Singer, M.,Choi, Y. S., Nesic, S. 2011a. Water chemistry for corrosion prediction in high pressure CO_2 environments, Presented at the Corrosion/11 conference, Houston, TX., 13-17 March, Paper No.11375.

Mohammed Nor, A.,Suhor, M. F.,Mohamed, M. F.,Singer M., and Nesic, S. 2011b. Corrosion of Carbon Steel in High CO_2 Environment: Flow Effect, Presented at theCorrosion/11 conference, Houston, TX., 13-17 March, Paper No. 11245.

Mohammed Nor, A., Suhor, M. F.,Abas, A. Z., Mat, S. 2014. Effect of CO_2/H_2S on corrosion behavior of API 5L 65 carbon steel in high P_{CO2} environments. Presented at the Offshore Technology Conference-Asia 14, Kuala Lumpur, Malaysia, 25-28 March, Paper No. OTC-24962-MS.

Naidu A. 2014. Modeling of CO_2 corrosion for non-scale forming conditions at elevated pressure and temperature, MS thesis, University of Oklahoma, Norman, Oklahoma.

Nazari, M. H., Allahkaram, S.R., and Kermani, M.B. 2010. The Effects of Temperature and pH on the Characteristics of Corrosion Product in CO_2 Corrosion of Grade X70 Steel, J. Materials and design 31: 3559-3563.

Nesic, S., Postlethwaite, J., and Olsen, S. 1995. An electrochemical model for prediction of CO_2 Corrosion, Presented at the Corrosion/95 conference, Houston, TX., Paper No. 131.

Nesic, S., Postlethwaite, J., Olsen, S. 1996a. An electrochemical model for prediction of corrosion of mild steel in aqueous carbon dioxide solutions, Corrosion 52: 280–294.

Nesic, S., Nordsveen, M., Nyborg, R., and Stangeland, A. 2001. A mechanistic model for CO_2corrosion with protective iron carbonate films, Presented at the Corrosion/01, Houston, TX., 11-16 March, Paper No. 040.

Nesic, S., Lee, K.J., and Ruzic V. 2002. The Mechanistic Model of Iron Carbonate Film Growth and the Effect on CO_2 Corrosion of Mild Steel, Presented at the Corrosion/02 conference, Denver, Co., 7-11 April, Paper no.237.

Nesic, S., and Lee, K.-L.J. 2003. A mechanistic model for CO_2 corrosion of mild steel in the presence of protective iron carbonate films - part III: film growth model, Corrosion 59: 616.

Nesic, S., Nordsveen, M., Nyborg, R., and Stangeland, A. 2003. A Mechanistic Model for CO_2 Corrosion of Mild Steel in the Presence of Protective Iron Carbonate Scales – Part II: A Numerical Experiment, Corrosion 59, 489.

Nesic, S. 2007. Key Issues Related to Modeling of Internal Corrosion of Oil and Gas Pipelines – A Review, J. Corros. Sci. 49: 4308-4338.

Nesic, S., Wang, S., Fang, H., Sun, W., and Lee, J. K-L. 2008. A New Updated Model of CO_2/H_2S Corrosion in Multiphase Flow, Presented at the Corrosion/08 conference, New Orleans, LA., 16-20 March, Paper No.535.

Nesic, S., Li, H., Huang, J., and Sormaz, D. 2009. An Open Source Mechanistic Model for CO_2/H_2S Corrosion of Carbon steel, Presented at the NACE Corrosion/09 conference, Atlanta, GA., 22-26 March, Paper No. 572.

Nordsveen M., Anderko M., Nesic, S., Nyborg, R., and Stangeland, A. 2003. A Mechanistic Model for Carbon Dioxide Corrosion of Mild Steel in the Presence of Protective Iron Carbonate Films -Part1: Theory and Verification, Corrosion 59, 443.

Olsen, S., Halvorsen, A.M., Per G. Lunde, and Nyborg, R. 2005. CO_2 corrosion prediction model -basic principles, Presented at the Corrosion/05 conference, Paper No. 551.

Omar, I.H., Gunaltun, Y.M., Kvarekvål, J., and Dugstad, A. 2005. H_2S Corrosion of Carbon Steel under Simulated Kashagan Field Conditions, Presented at the Corrosion/05 conference, Houston, TX., 3-7April, Paper No. 300.

O'Sullivan, T.D., and Smith, N.O. 1970. Solubility and partial molar volume of nitrogen and methane in water and in aqueous sodium chloride from 50 to 125 degrees and 100 to 600 atm. J. Phys. Chem. 74 (7): 1460–1466.

Perdomo, J., Morales, J.L., Viloria, A., and Lusinchi, A.J. 2000. CO_2 and H_2S Corrosion of API 5L-B and 5L-X52 Grade Steels, Presented at the Corrosion/2000 conference, Orlando, Fl., 26-31 March, Paper No. 42.

Pfennig, A., Kranzmann, A. 2012. Effect of CO_2 and pressure on the stability of steels with different amounts of chromium in saline water, Corros. Sci. 65: 441–452.

Pitzer, K.S., Peiper, J.C., and Busey, R.H. 1984. Thermodynamic properties of aqueous sodium chloride solutions, J. Phys. Chem. Ref. Data 13: 1–102.

Plennevauxa, C., Ferrandob, N., Kittelc, J., Frégonèsed, M., Normandd, B., Cassagnea, T., Ropitalc, F., and Bonisa M. 2013. pH prediction in concentrated aqueous solutions under high pressure of acid gases and high temperature, j. Corr. Sci. 73: 143-149.

Price, L.C. 1979. Aqueous solubility of methane at elevated pressures and temperatures, Aapg Bull. 63 (9): 1527–1533.

Pots, B.F.M. 1995. Mechanistic models for the prediction of CO_2 corrosion rates under multiphase flow conditions, Presented at the Corrosion/1995 conference, Houston, TX., 26-31 Mar, Paper No. 137.

Pots, B.F.M., John, R.C., Rippon, I.J., Thomas, M.J.J.S., Kapusta, S.D., Grigs, M.M., and Whitham, T. 2002. Improvements on de Waard-Milliams corrosion prediction and applications to corrosion management, Presented at the Corrosion/02 conference, Denver, Colorado, 7-11 April, Paper No. 235.

Qu Q., Ma J., Wang L., Li L., Bai W., and Ding Z. 2011. Corrosion behaviour of AZ31B magnesium alloy in NaCl solutions saturated with CO_2, J. Corr. Sci. 53:1186–1193.

Rajappa, S., Zhang, R., and Gopal, M. 1998. Modeling the diffusion Effects through the Iron Carbonate Layer in the Carbon Dioxide Corrosion of Carbon Steel, Presented at the Corrosion/98 conference, Houston, TX., 22-27 March, Paper No. 26.

Ranji R.A., and Zakeri, A.H. 2010. Mechanical properties and corrosion resistance of normal strength and high strength steels in chloride solution, J. Nava. Arch. Mar. Eng. 7: 93-100.

Rihan O. R. 2013. Electrochemical Corrosion Behavior of X52 and X60 Steels in Carbon Dioxide Containing Saltwater Solution, Mat. Res. 16(1): 227-236.

Rumpf, B., Nicolaisen, H. Ocal, C., and Maurer, G. 1994. Solubility of carbon dioxide in aqueous solutions of sodium chloride: experimental results and correlation, J. Sol. Chem. 23: 431– 448.

Ruzic, V., Veidt, M. and Nesic, S. 2006. Protective iron carbonate films -Part 2: Chemical removal by dissolution in single-phase aqueous flow, Corrosion 62 (7): 598-611.

Schmitt, G. 1984. Advances in CO_2 Corrosion, NACE Corrosion 1: 1–6.

Schmitt, G. 1991. Effect of elemental sulfur on corrosion in sour gas, Systems J. Corr., 47: 285-308.

Schutt H. U., and Lyle, F. F. 1998. CO_2/H_2S Corrosion under wet gas pipeline conditions in the presence of bicarbonate, chloride, and oxygen, Presented at the Corrosion/98 conference, San Diego, Ca., 22-27 March, Paper No.11.

Schmitt, G., Hörstemeier, M. 2006. Fundamental Aspects of CO_2 Metal Loss Corrosion, Part II: Influence of different Parameters on the CO_2 Corrosion Mechanism, Presented at Corrosion/06 conference, San Diego, California, 12-16 March, Paper No. 112.

Seiersten, M. 2001. Material Selection for Separation, Transportation and Disposal of CO_2, NACE, Houston, TX., 11-16 March, Paper No.01042.

Selleck, F.T., Carmichael, Sage, L.T. B.H., Ind. Eng. Chem. 44 (1952) 2219–2226.

Silva, C.A.R., Liu, X., and Millero, F.J. 2002. Solubility of Siderite in NaCl Solutions. Journal of Solution Chemistry, 31(2): p. 97-108.

Singer, M., Brown, B., Camacho, A. and Nesic, S. 2007. Combined effect of CO_2, H_2S and acetic acid on bottom of the line corrosion, Presented at the Corrosion/07 conference, Nashville, Tennessee, 11-15 March, Paper No.661.

Singer, M., Camacho, A., Brown, B. and Nesic, S. 2010. Sour top of the line corrosion in the presence of acetic acid, Presented at the Corrosion/10 conference, San Antonio, TX., 14-18 March, Paper No.100.

Simmons M. R. 2008. Oil and Gas Rust: An Evil Worse Than Depletion, Offshore Technology Conference (OTC) Presentation, May.

Smith, S.N. 1993. A Proposed Mechanism for Corrosion in Slightly Sour Oil and Gas Production, Presented at the twelfth International Corrosion Congress, Houston, TX., September 19-24, Paper No.385.

Smith, S.N. and Wright, E.J. 1994. Prediction of Minimum H_2S Levels Required for Slightly Sour Corrosion, Houston, TX., Paper No.11.

Smith, S. N., and Pacheco, J. L. 2002. Prediction of corrosion in slightly sour environments, Presented at the Corrosion/02 conference, Denver, Co., 7-11 April, Paper No. 241.

Smith, S. N. and Joosten, M. 2006. Corrosion of Carbon Steel by H_2S in CO_2 Containing Oilfield Environments, Houston, TX., 12-16 March, Paper No. 115.

Sompalli, B. 1996. Prediction of CO_2 corrosion of carbon steel in pipe flow: A mechanistic approach, Master thesis, University of Tulsa, Tulsa, OK.

Solehudin, A., Nurdin, I., Agma, M., Suratno, W. 2010. EIS Study of Temperature and H_2S Concentration Effect on API 5LX65 Carbon Steel Corrosion in Chloride Solution, Presented at the Third International Conference on Mathematics and Natural Sciences.

Spitzer, P., Fisicaro, P., Meinrath, G. et al. 2011. pH buffer assessment and Pitzer's equations, Accred Qual Assur 16: 191.

Srinivasan, S., and Kane, R. D. 1996. Prediction of corrosivity of CO_2/H_2S production environments, Presented at the Corrosion/ 96 conference, Denver, Co., 24-29 March, Paper No.11.

Sridharan, V. 2009. Measurement of Carbon Dioxide Corrosion on Carbon Steel using Electrochemical Frequency Modulation, MS thesis, University of Saskatchewan, Saskatoon (June 2009).

Steiger M., Kiekbusch, J., and Nicolai, A. 2008. An improved model incorporating Pitzer's equations for calculation of thermodynamic properties of pore solutions implemented into an efficient program code, Const. Building Mat. 22 (8): 1841-1850.

Suhor, M. F., Mohamed, M.F., Nor, M. A., Singer. M., and Nesic, S. 2012. Corrosion of Mild Steel in High CO_2 Environment: Effect of the $FeCO_3$ Layer, NACE, Salt Lake City, Utah, 11-15 March, Paper No. C2012-0001434.

Suk Seo, H., Park, J.H., Choi, J. G., and Kim, S. J. 2015. Alloying Effect on Corrosion Property of High Mn Steel in Sour Environment, Presented at the Twenty-fifth International Ocean and Polar Engineering Conference, Kona, Hawaii.

Suleimenov, O.M., Krupp, R.E. 1994. Solubility of hydrogen sulfide in pure water and in NaCl solutions, from 20 to 320°C and at saturation pressures, Geochim. Cosmochim. Acta 58 (11): 2433–2444.

Sun, J. Y. and Jepson, W. P. 1992. Slug Flow Characteristics and Their Effect on Corrosion Rates in Horizontal Oil and Gas Pipelines, J. SPE 24787, Washington, DC.

Sun, R., Hu, W. and Duan Z. 2001. Prediction of Nitrogen Solubility in Pure Water and Aqueous NaCl Solutions up to High Temperature, Pressure, and Ionic Strength, J. Sol. Chem. 30: 561.

Sun, Y., Gorge, K., Nesic, S. 2003. The Effect of Cl^- and Acetic Acid on Localized CO_2 Corrosion in Wet Gas Flow, Presented at the Corrosion/2003 conference, Houston, TX., 16-20 March, Paper no. 327.

Sun, Y., and Nešić, S. 2004. A parametric Study and Modeling on Localized CO_2 Corrosion in Horizontal Wet Gas Flow, Presented at the Corrosion/04, Houston, TX., 28 March-1 April Paper No. 380.

Sun, W., Nesic, S. and Papavinasam, S. 2006. Kinetics of iron sulfide and mixed iron sulfide/carbonate scale precipitation in CO_2/H_2S corrosion. Presented at the Corrosion/06 conference, San Diego, Ca., 12-16 March, Paper No. 644.

Sun, W., and Nešić, S. 2007. A mechanistic model of H_2S corrosion of mild steel, Presented at the Corrosion/07 conference, Nashville, Tennessee, 11-15 March, Paper No. 655.

Sun, W., Nesic, S., Papavinasam, S. 2008a. Kinetics of Corrosion Layer Formation, Part 2 Iron Sulfide and Mixed Iron Sulfide/Carbonate Layers in Carbon Dioxide/Hydrogen Sulfide Corrosion, Corrosion 64, 586.

Sun, W., Nešić, S., Young, D., and Woollam, R. C. 2008b. Equilibrium expressions related to the solubility of the sour corrosion product mackinawite, Ind. & Eng. Chem. Res. 47(5):1738-1742.

Sun, W. and Nesic, S. 2009. A mechanistic model of uniform hydrogen sulfide/carbon dioxide corrosion of mild steel, Corrosion 65: 291-307.

Sun, J.B., Liu, W., Chang, W., Zhang, Z.H., Li, Z.T., Yu, T., and Lu, M.X. 2009a. Characteristics and formation mechanism of corrosion scales on low-chromium X65 steels in CO_2 environment, Acta Metall Sin 45: 84–90.

Sun, W., Nešić, S., and R.C. Woollam, 2009b. The effect of temperature and ionic strength on iron carbonate ($FeCO_3$) solubility limit. Corr. Sci. 51(6): p. 1273-1276.

Sun, J., Sun, C., Lin, X., Cheng, X., Liu, H. 2016. Effect of chromium on corrosion behavior of P110 steels in CO_2-H_2S environment with high pressure and high temperature Mater, 9, 200.

Svenningsen, G., Palencsár, A., and Kvarekvå, J. 2009. Investigation of iron sulfide surface layer growth in aqueous H_2S/CO_2 environments. Presented at the Corrosion/09 conference, Atlanta, GE., 22-26 March, Paper No.359.

Tanaka, N., Tamamushi, R. 1964. Kinetic Parameters of Electrode Reactions, Electrochim. Acta, 9: 963.

Tang, J., Shao, Y., J. Guo, Zhang, T., Meng, G., Wanga, F. 2010. The effect of H_2S concentration on the corrosion behavior of carbon steel at 90 °C, Corros. Sci. 52: 2050–2058.

Takabe, H., Ueda, M. 2001. The formation behavior of corrosion protective films of low Cr bearing steels in CO_2 environments, Corrosion, 01066.

Takenouchi, S., and Kennedy, G.C. 1965. The solubility of carbon dioxide in NaCl solution at high temperature and pressure, Am. J. Sci., 263: 445–454.

Todheide, K., Franck, E.U., 1963. Das Zweiphasengebiet und die kritische Kurve im System Kohlendioxid-Wasser bis zu Druckenvon 3500 bar. Z. Phys. Chem. 37, 387– 401.

Tran, T., Brown, B., Nesic, S. 2015. Corrosion of Mild Steel in an Aqueous CO_2 Environment – Basic Electrochemical Mechanisms Revisited, Presented at the Corrosion/15 conference, Dallas, TX., 15-19 March, Paper No. 5671.

Turgoose, S., Cottis, R.A., Lawson, K. 1992. Modeling of electrode processes and surface chemistry in carbon dioxide containing solutions, in: Computer Modeling in Corrosion. ASTM STP 1154: 67–81.

Uhlig, H.H., and Revie, R.W. 1985. Corrosion and Corrosion Control: An Introduction to Corrosion Science and Engineering, 4th ed. Hoboken, NJ: John Wiley & Sons: 96.

Valdes, A., Case, R., Ramirez, M. and Ruiz, A. 1998. The effect of small amounts of H_2S on CO_2 corrosion of carbon steel, Presented at the Corrosion/98 conference, Corrosion/98, San Diego, Ca., 22-27 March, Paper No.22.

Valtz, A., Chapoy, A., Coquelet, C., Paricaud, P., and Richon D. 2004. Vapor–liquid equilibria in the carbon dioxide–water system, measurement and modeling from 278.2 to 318.2 K, Fluid Phase Equilibr. 226: 333–344.

Videm, K., and Dugstad, A. 1989a. Corrosion of carbon steel in an aqueous carbon dioxide environment. Part 1: film formation. Mater. Perform. (28): 63-67.

Videm, K., and Dugstad, A. 1989b. Corrosion of carbon steel in an aqueous carbon dioxide environment Part 2: Solution effects. Mater. Perform. (28):46.

Videm, K. 1993. Fundamental Studies aimed at Improving Models for Prediction of CO_2 Corrosion, Progress in the Understanding and Prevention of Corrosion, Proceedings from 10th European Corrosion Congress, (1): 513.

Videm, K., and Kvarekval, J. 1995. Corrosion of carbon steel in carbon dioxide-saturated solutions containing small amounts of hydrogen sulfide, J. Corr., 51: 260-269.

Videm, K., Kvarekvaal, J., Perez, T., and Fitzsimons, G. 1996. Surface effects on the electrochemistry of iron and carbon steel electrodes in aqueous CO_2 solutions, Presented at the International Corrosion Conference/1996, Houston, Tx., Paper No.1.

Wang, H., Yong Cai, J., and Paul J. W. 2002. CO_2 Corrosion Mechanistic Modeling and Prediction in Horizontal Slug Flow, Presented at Corrosion/02, Denver, Colorado, 7-11 April, Paper No. 02238.

Wang, S., George, K., and Nesic, S. 2004. High Pressure CO_2 Corrosion Electrochemistry and the Effect of Acetic Acid, Presented at the Corrosion/04 conference, New Orleans, Lo., 28 March-1 April, Paper No. 375.

Wei, L., Pang, X., Gao, K. 2016. Effect of small amount of H_2S on the corrosion behavior of carbon steel in the dynamic supercritical CO_2 environments, Corros. Sci. 103: 132-144.

Wen-fei, L., Yan-jun, Z. U., and Yan, X. 2012. Corrosion Behavior of 110S Tube Steel in Environments of High H_2S and CO_2 Content, journal of iron and steel research, International, 19(12): 59-65.

Winkler, L.W. 1901. Solubility of gas in water. Berichte Der DeutschenChemischenGesellschaft 34: 1408–1422.

Woollam, R., Tummala, K., Vera, J. and Hernandez, S. 2011. Thermodynamic prediction of $FeCO_3$/FeS corrosion product films, Presented at the Corrosion/11 conference, Orlando, Fl., 26-31 March, Paper No. 076.

Xiang, Y., Wang, Z., Li, Z., and Ni, W.D. 2013. Effects of Temperature on Corrosion Behavior of X70 Steel in High Pressure $CO_2/SO_2/O_2/H_2O$ Environments, J. Corros. Eng. Sci. Tech. 48.

Yabuki, A. 2011. Mass Transfer Equation and Hydrodynamic Effects in Erosion-Corrosion, Advanced Topics in Mass Transfer, Mohamed El-Amin (Ed.), ISBN: 978-953-307-333-0, In Tech, University Campus step rislavkakrautzeka83/A 51000 Rijeka, Croatia.

Yan, W., Deng, J., Dong, X., Zhang, C., and Li, W. 2012. Experimental study of 3% Cr tubing steel in CO_2 and CO_2/H_2S corrosion environment, Oil Gas Facilities 10: 43–48.

Yan, W., Deng, J., Zhu, P., and Xing, X. 2015. Investigation of P_{H2S} influence on 3% Cr tubing steel corrosion behaviors in CO_2–H_2S–Cl^- environment, Corr. Eng. Sci. Technol. 50: 525–532.

Yevtushenko, O., Bettge, D., Bohraus, S., Bäßler, R., Pfennig, A., and Kranzmann, A. 2014. Corrosion behavior of steels for CO_2 injection, J. Pro. Saf. Environ. Prot. 92: 108-118.

Yevtushenko, O., Bäßler, R., and Carrillo-Salgado, I. 2013. Corrosion stability of piping steels in a circulating supercritical impure CO_2 Environment, Presented at the Corrosion/13, Orlando, FL., 17-21 March, Paper No. 2372.

Yin, Z.F., Zhao, W.Z., Bai, Z.Q., Feng, Y. R., and Zhou, W.J. 2008. Corrosion Behavior of SM80SS Tube Steel in Stimulant Solution Containing H_2S and CO_2, Electrochemica Acta 53: 3690–3700.

Yin, Z. F., Feng, Y. R., Zhao, W. Z., Bai, Z. Q., and Lin, G. F. 2009. Effect of Temperature on CO_2 Corrosion of Carbon Steel, J. Surf. Interface Anal. 41: 517–523.

Zhang, L., Ding, R. M., J. Yang, W., and Lu, M. X. 2009a. Analysis of corrosion scales on X60 steel under high CO_2/H_2S content environments, J. Univ. Sci. Tech. Beijing, 31:563–567.

Zhang, L., Yang, J., Sun, J., and Lu, M. 2009b. Effect of Pressure on Wet H_2S/CO_2 Corrosion of Pipeline Steel, Presented at the Corrosion/09 conference, Atlanta, GA., 22-26 March, Paper No. 565.

Zhang, L., Zhong, W., Yang, J., Gu, T., Xiao, X., and Lu, M. 2011. Effects of temperature and partial pressure on H_2S/CO_2 corrosion of pipeline steel in sour conditions, Presented at the Corrosion/11 conference, Houston, TX., 13-17 March, Paper No. 79.

Zhang, G.A., Zeng, Y., Guo, X.P., Jiang, F., Shi, D.Y., and Chen, Z.Y. 2012. Electrochemical corrosion behavior of carbon steel under dynamic high pressure H_2S/CO_2 environment, Corr. Sci. 6: 37–47.

Zhang, Y., Gao, K., Schmitt, G., and Hausler, H. 2013a. Modeling Steel Corrosion under Supercritical CO_2 Conditions, J. Mat. Corr. 64: 478–485.

Zhang, X., Zevenbergen, J., and Benedictus, T. 2013b. Corrosion Studies on Casing Steel in CO_2 Storage Environments, J. Energy Procedia .

Zhao, G. X., Yan, M. L., Lu, M, X., and LI, P. 2000. Materials Evaluation in CO_2 Corrosion Environment, J. Corros. Sci. Prot. Tech. 12 (4): 240-242.

Zheng, Y., Brown, B., and Nesic, S. 2013. Electrochemical Study and Modeling of H_2S Corrosion of Mild Steel, Presented at the Corrosion/13 conference, Orlando, Fl., 17-21 March, Paper No. 2406.

Zheng, Y., Ning, J., Brown, B. and Nesic, S. 2014. Electrochemical model of mild steel corrosion in a mixed H_2S/CO_2 aqueous environment, Presented at the Corrosion/14 conference, San Antonio, TX., 9-13 March, Paper No. 3907.

Zirrahi, M., Azin, R., Hassanzadeh, H., and Moshfeghian, M. 2012. Mutual solubility of CH_4, CO_2, H_2S, and their mixtures in brine under subsurface disposal conditions, Fluid Phase Equilib., 324: 80–93.

Zuo, Y., and Guo, T.M. 1991. Extension of the Patel–Teja equation of state to the prediction of the solubility of natural gas in formation water, Chem. Eng. Sci. 46 (12): 3251– 3258.

APPENDIX A

NOMENCLATURE

A exposed area (cm^2)

A_{sp} surface area of the steel, m^2

A_{CO_2} solid –state diffusion kinetic constant for CO_2, $A_{CO_2}=2.0\times10^{-6}$ mol/(m^2s)

A_{H^+} solid –state diffusion kinetic constant for H^+, $A_{H^+}=4.0\times10^{-4}$ mol/(m^2s)

A_{H_2S} solid –state diffusion kinetic constant for H_2S, $A_{H_2S}=2.0\times10^{-5}$ mol/(m^2s)

$c_{b,Fe^{2+}}$ bulk concentration of Fe^{2+} (mol/m^3)

c_{b,H^+} bulk concentration of H^+ (mol/m^3)

c_{b,CO_2} bulk concentration of CO_2 (mol/m^3)

c_{b,H_2CO_3} bulk concentration of H_2CO_3 (mol/m^3)

c_{b,HCO_3^-} bulk concentration of HCO_3^- (mol/m^3)

$c_{b,CO_3^{2-}}$ bulk concentration of CO_3^{2-} (mol/m^3)

c_{b,H_2S} bulk concentration of H_2S (mol/m^3)

c_{b,HS^-} bulk concentration of HS^- (mol/m^3)

$c_{b,S^{2-}}$ bulk concentration of S^{2-} (mol/m^3)

c_{b,OH^-} bulk concentration of OH^- (mol/m^3)

$c_{s,Fe^{2+}}$ surface concentration of Fe^{2+} (mol/m^3)

c_{s,H^+} surface concentration of H^+ (mol/m^3)

c_{s,H_2} surface concentration of H_2 (mol/m^3)

c_{s,H_2CO_3} surface concentration of H_2CO_3 (mol/m^3)

c_{s,HCO_3^-} surface concentration of HCO_3^- (mol/m^3)

$c_{s,CO_3^{2-}}$ surface concentration of CO_3^{2-} (mol/m^3)

c_{s,H_2S} surface concentration of H_2S (mol/m^3)

c_{s,HS^-} surface concentration of HS^- (mol/m^3)

$c_{s,S^{2-}}$ surface concentration of S^{2-} (mol/m^3)

c_{s,OH^-} surface concentration of OH^- (mol/m^3)

CR: corrosion rate (mm/y)

c_{b,CO_2} bulk aqueous concentration of CO_2, mol/m^3

c_{b,H^+} bulk aqueous concentration of H^+, mol/m^3

c_{b,H_2S} bulk aqueous concentration of H_2S, mol/m^3

c_{CO2} bulk aqueous concentration of CO_2 in mol/m^3

c_{H^+} bulk aqueous concentration of H^+ ions, mol/m^3

$c_{H_2CO_3}$ bulk aqueous concentration of H_2CO_3, mol/m^3

c_{H^+} bulk aqueous concentration of H^+, mol/m^3

$c_{HCO_3^-}$ bulk aqueous concentration of bicarbonate, mol/m^3

$c_{CO_3^{2-}}$ bulk aqueous concentration of carbonate ion, mol/m^3

c_{H_2S} bulk aqueous concentration of H_2S, mol/m^3

c_{HS^-} bulk aqueous concentration of H_2S, mol/m^3

c_{S,H_2S} "near-zero" concentration of H_2S on the steel surface set to 1.00×10^{-7}, mol/m^3

c_{S,H^+} "near-zero" concentration of H^+ on the steel surface set to 1.00×10^{-7}, mol/m^3

c_{S,CO_2} concentration of CO_2 on the steel surface, mol/m^3

CR_T total corrosion rate, mm/y

CR_{H_2S} corrosion rate due to H_2S, mm/y

CR_{H^+} corrosion rate due to proton, mm/y

CR_{CO_2} corrosion rate due to CO_2, mm/y

D_{CO_2} diffusion coefficient for dissolved CO_2 in water

$D_{H_2CO_3}$ diffusion coefficient for dissolved H_2CO_3 in water

D_{H^+} diffusion coefficient for dissolved H^+ in the water

D_{H_2S} diffusion coefficient for dissolved H_2S in water

E_{corr} corrosion potential (V)

$E_{Fe^{2+}}$ potential for the iron ions oxidation (V)

E_{H^+} potential for the hydrogen ion reduction (V)

$E_{H_2CO_3}$ potential for the carbonic acid reduction (V)

$E_{HCO_3^-}$ potential for the bicarbonate reduction (V)

E_{H_2S} potential for the aqueous hydrogen sulfide reduction (V)

E_{HS^-} potential for the aqueous HS^- reduction (V)

$E^0_{H^+}$ and $E^0_{Fe^{2+}}$ the standard potentials of hydrogen and iron ions, respectively

EW is the equivalent weight (g)

F Faraday's constant (=96500 C/mol)

$Flux_{H_2S}$ flux of H_2S expressed in mol/(m^2s)

$Flux_{H^+}$ flux of protons expressed in mol/(m^2s)

$Flux_{CO_2}$ flux of CO_2 expressed, mol/(m^2s)

i_a anodic current density (A/m^2)

i_c cathodic current density (A/m^2)

$i_{Fe^{2+}}$ current density for iron ions (A/m^2)

i_{H^+} current density for hydrogen ions (A/m^2)

$i_{H_2CO_3}$ current density for carbonic acid (A/m^2)

$i_{HCO_3^-}$ current density for bicarbonate (A/m^2)

i_{H_2S} current density for hydrogen sulfide (A/m^2)

i_{HS^-} current density for HS^- (A/m^2)

i_{corr} corrosion current density (A/m^2)

$K_{e,Fe^{2+}}$ electrochemical reaction rate constant for the iron ions (m/s)

K_{e,H^+} electrochemical reaction rate constant for the hydrogen ions (m/s)

K_{e,H_2CO_3} electrochemical reaction rate constant for the carbonic acid (m/s)

K_{e,HCO_3^-} electrochemical reaction rate constant for the bicarbonate (m/s)

$K_{e,CO_3^{2-}}$ electrochemical reaction rate constant for the carbonate ions (m/s)

K_{e,H_2S} electrochemical reaction rate constant for the hydrogen sulfide (m/s)

K_{e,HS^-} electrochemical reaction rate constant for the HS^- (m/s)

$K_{mt,Fe^{2+}}$ mass transfer coefficient of iron ions (m/s)

K_{mt,H^+} mass transfer coefficient of hydrogen ions (m/s)

K_{mt,H_2CO_3} mass transfer coefficient of carbonic acid (m/s)

K_{mt,HCO_3^-} mass transfer coefficient of bicarbonate ions (m/s)

$K_{mt,CO_3^{2-}}$ mass transfer coefficient of carbonate ions(m/s)

K_{mt,H_2S} mass transfer coefficient of hydrogen sulfide(m/s)

K_{mt,HS^-} mass transfer coefficient of HS^- (m/s)

K_{mt,S^-} mass transfer coefficient of S^- (m/s)

K_{sol,CO_2} Henry's constant for CO_2 dissolution (mol/m^3.bar)

K_{sol,H_2S} Henry's constant for H_2S dissolution (mol/m^3.bar)

K_{1,CO_2} first dissociation constant of carbonic acid

K_{2,CO_2} second dissociation constant of carbonic acid

K_{1,H_2S} first dissociation constant of H_2S

K_{2,H_2S} second dissociation constant of H_2S

K_W: water dissociation constant

K_{hyd}^f forward reaction rate for the CO_2 hydration reaction, 1/s

K_{hyd} equilibrium hydration/dehydration constant CO_2, $K_{hyd} = 2.58\times10^{-3}$

K_{CO2} equilibrium solubility constant of CO_2, mol/L

$K_{CO_2,1}$ first dissociation constant of CO_2, mol/L

$K_{CO_2,2}$ second dissociation constant of CO_2, mol/L

K_{H_2S} equilibrium solubility constant of H_2S, mol/L

$K_{H_2S,1}$ first dissociation constant of H_2S, mol/L

$K_{H_2S,2}$ second dissociation constant of H_2S, mol/L

$K_{overall}$ overall dissociation constants of dissolved CO_2, mol/L

K_{m,H_2S} mass-transfer coefficient for H_2S in the hydrodynamic boundary

K_{m,H^+} mass-transfer coefficient for H^+ in the hydrodynamic boundary

K_{m,CO_2} mass-transfer coefficient for CO_2 in the hydrodynamic boundary

M_{Fe} iron molecular weight (=55.85 kg/kmol)

m_i molality of component i or salts in the liquid phase

M_{FeS} molar mass of iron sulfide, kg/mol

n: number of moles of electrons involved in the electrochemical reaction

$P_{H_2O}^S$ saturation water pressure, bar

P total pressure, bar

P_{CO_2} CO_2 partial pressure (bar)

P_{H_2S} CO_2 partial pressure (bar)

R universal gas constant (=8.314 J/mol.K)

T	temperature (K)
pH	solution pH
R	universal gas constant,
SRR	sulfide retention rate
SFR	sulfide formation rate
SDR	sulfide damage rate
T	temperature, K
x_{H_2O}	mole fraction of water in the liquid phase, dimensionless
y_{H_2O}	mole fraction of water in the gas phase, dimensionless

Subscripts

a	anion
c	cation
i	refers to acidic components of the gas phase (CO_2 and H_2S)

Greek letters

Δm_{os}	mass of the mackinawite layer, kg
Δt	time interval, second
φ_{H2O}	fugacity coefficient of water in the gas phase
φ_i	fugacity coefficient of component i in the gas phase
$\mu_i^{l(0)}$	chemical potential of component i
$\upsilon_{H2O}^{'}$	molar volume of water in liquid phase
γ_i	activity coefficient of component i
λ_{i-ion}	interaction parameter
$\xi_{i-cation-anion}$	interaction parameter
$\delta_{0.5}$	thickness of the mackinawite layer, m
ε	outer mackinawite layer porosity
ψ	outer mackinawite layer tortuosity factor
β	transfer coefficient (mV/decade)
ρ_{Fe}	iron mass density (=7800 kg/m^3)
ρ_{st}	Density of steel

ΔT Average specimen thickness loss due to corrosion

Symbols

A Exposed area

t Exposure time

w Specimen width

W_1 Initial weight of specimen

W_2 Final weight of specimen

Acronyms

CHR CO_2/H_2S ratio

HPHT High-pressure high temperature

LCC Load carrying capacity

LCC_{uncorr} Load carrying capacity of un-corroded specimen

LCC_{corr} Load carrying capacity of corroded specimen

UTS Ultimate tensile strength

ΔLCC_T Total reduction in carrying capacity

ΔLCC_{uc} Reduction in load carrying capacity due to uniform corrosion

APPENDIX B

TENSILE STRENGTH TEST MEASUREMENTS

B.1. Effect of CO_2 partial pressure on the mechanical properties of carbon steels

B.1.1. Q125 Carbon Steel

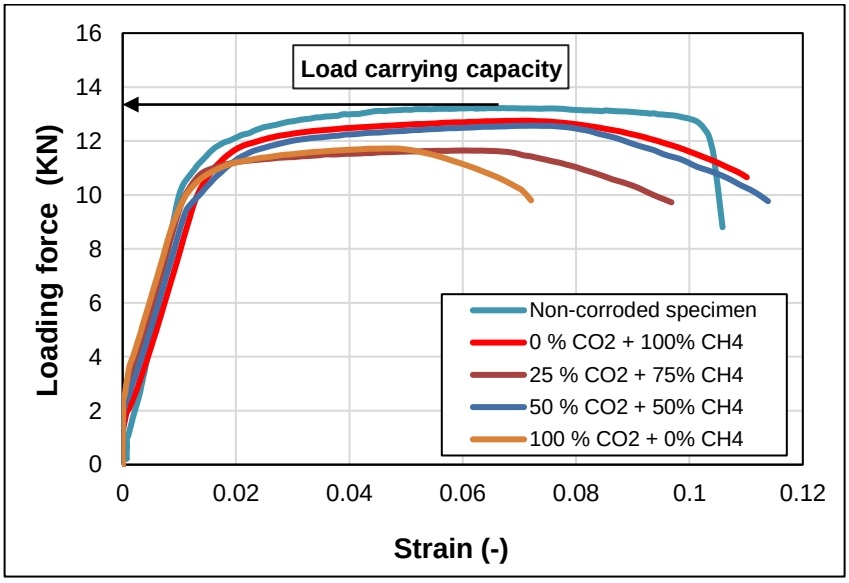

Fig. B.1 Applied instantaneous load versus elongation for Q125 carbon steel exposed to pure CO_2-saturated brine at various CO_2 partial pressure

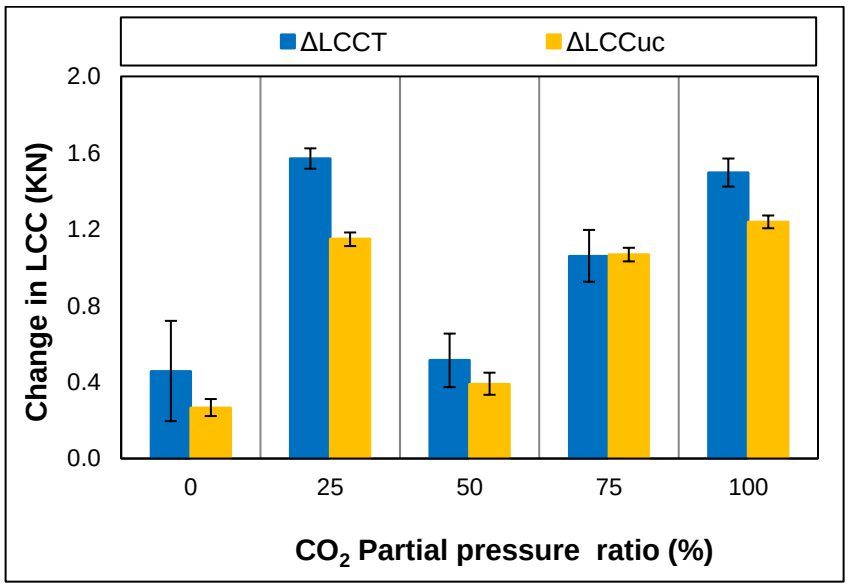

Fig. B.2 ΔLCCT and ΔLCCuc of Q125 carbon steel as a function of CO_2 partial pressure ratio (PPR) at 40.37 MPa and 38°C

B.1.1. T95Carbon Steel

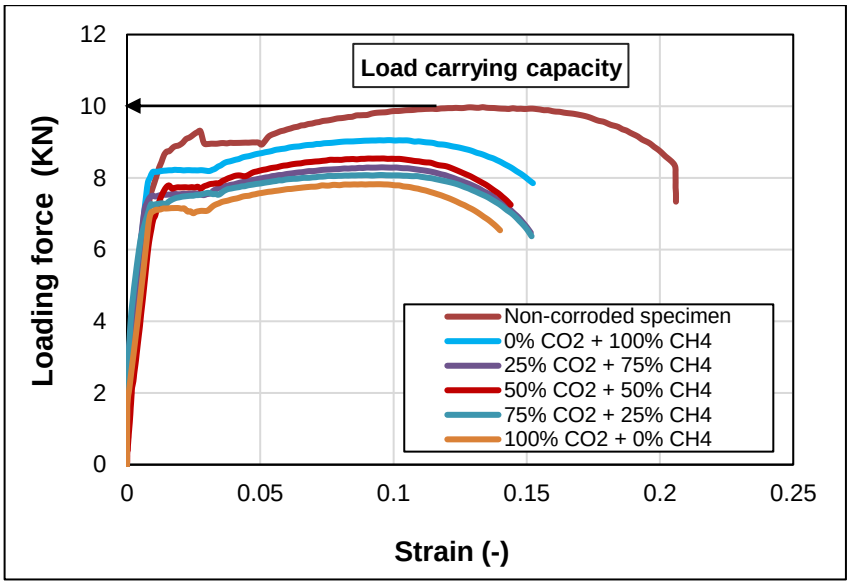

Fig. B.3 Applied instantaneous load versus elongation for T95 carbon steel exposed to pure CO_2-saturated brine at various CO_2 partial pressure

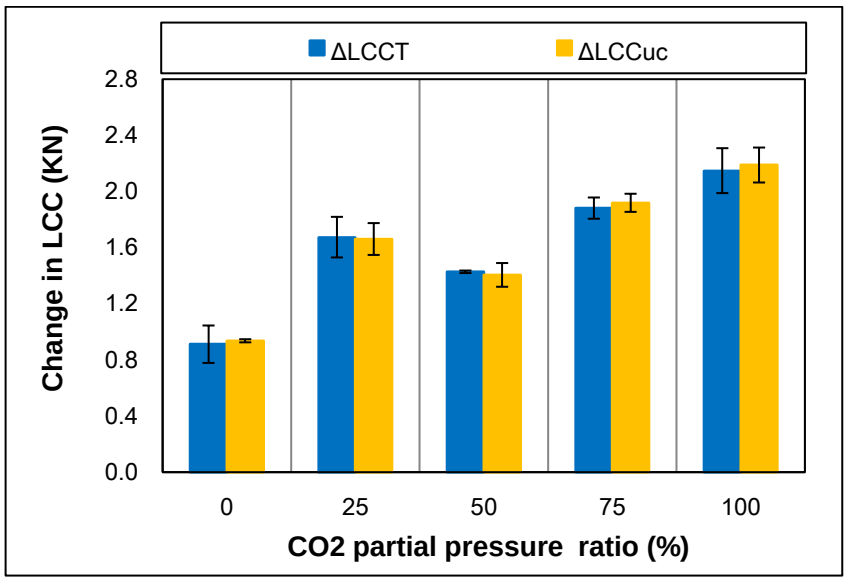

Fig. B.4 ΔLCCT and ΔLCCuc of T95 carbon steel as a function of CO_2 partial pressure ratio (PPR) at 40.37 MPa and 38°C

B.2. Effect of total pressure on the mechanical properties of carbon steels

B.2.1. C110 carbon steel

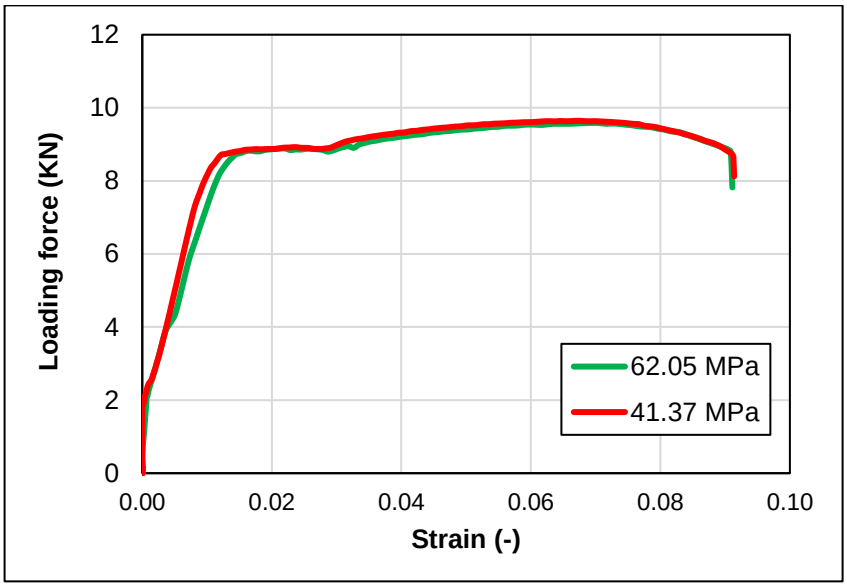

Fig. B.5 Applied instantaneous load versus elongation for C110 carbon steel exposed to 50% CO_2-saturated brine at various total pressures

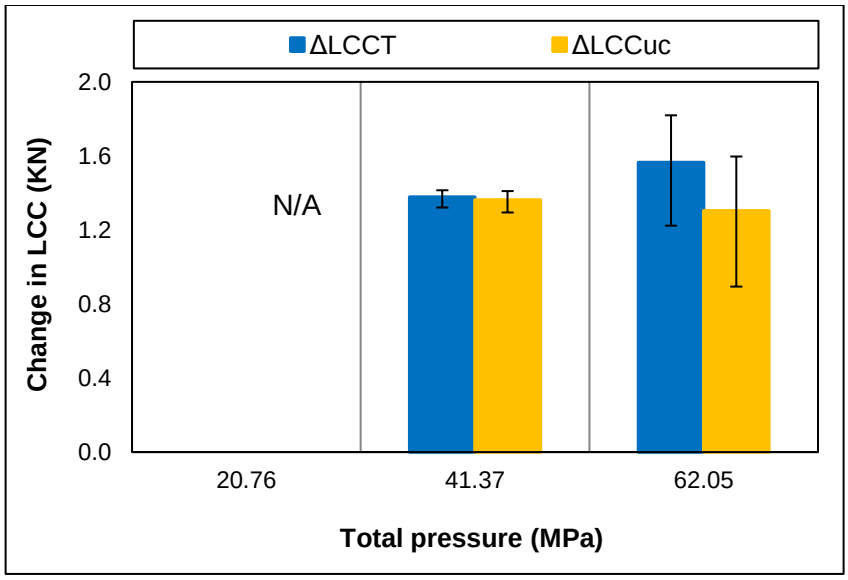

Fig. B.6 ΔLCCT and ΔLCCuc of C110 carbon steel exposed to 50% CO_2-saturated brine at various total pressures, and 38°C

B.2.2. T95 carbon steel

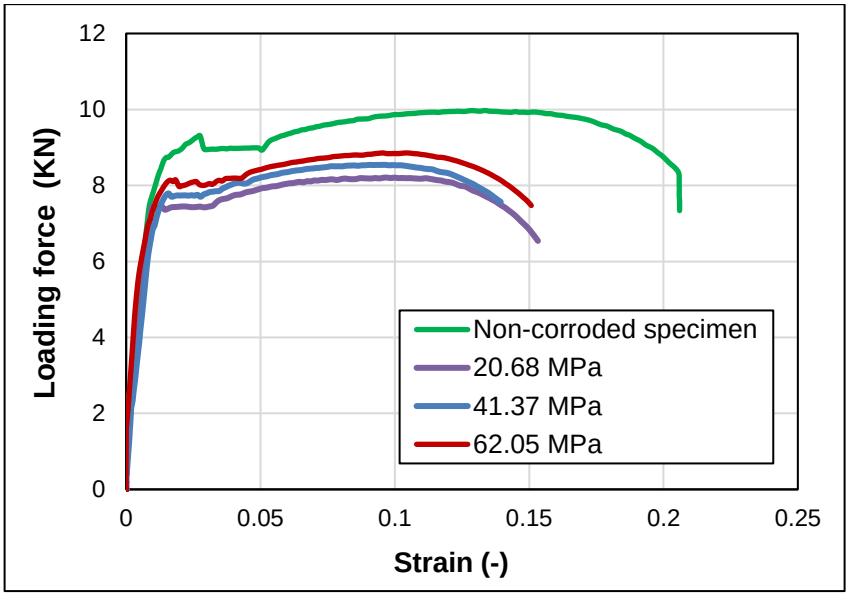

Fig. B.7 Applied instantaneous load versus elongation for T95 carbon steel exposed to 50% CO_2-saturated brine at various total pressures

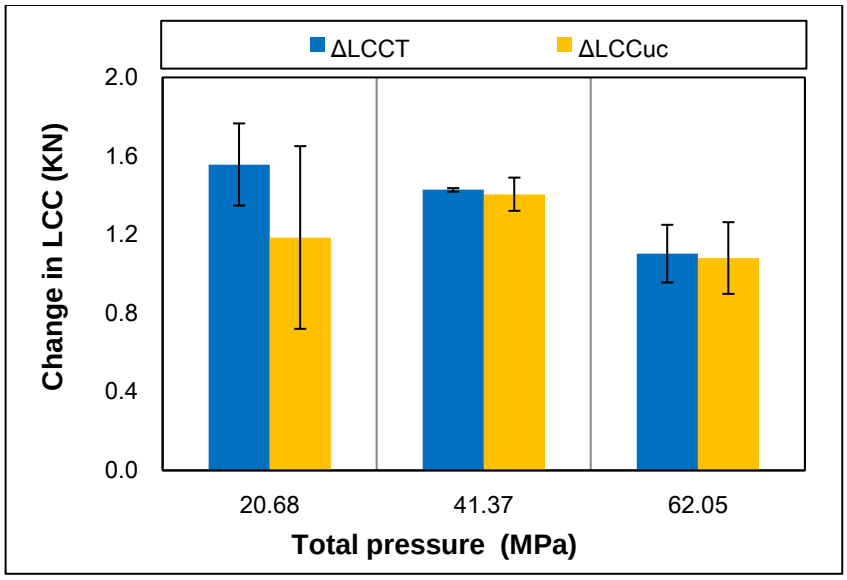

Fig. B.8 ΔLCCT and ΔLCCuc of T95 carbon steel exposed to 50% CO_2-saturated brine at various total pressures, and 38°C

B.2.2. Q125 carbon steel

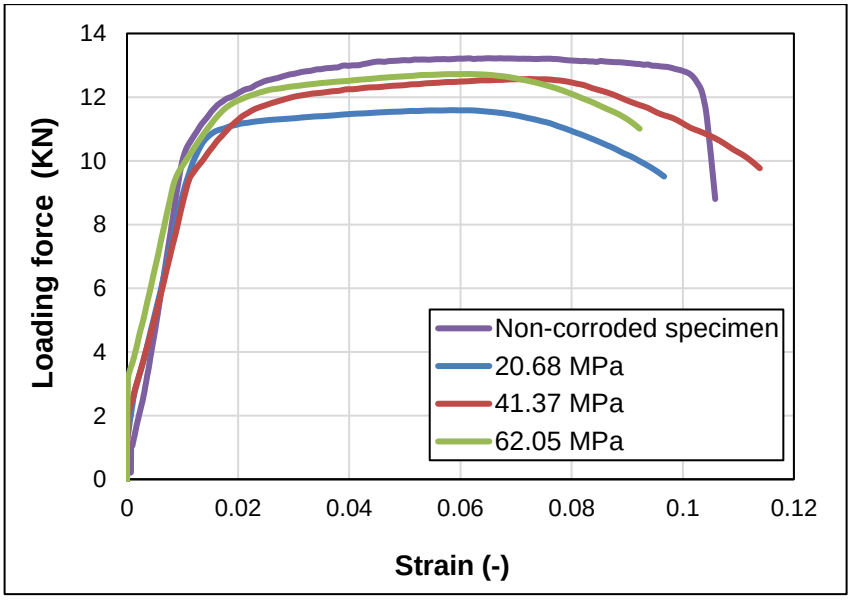

Fig. B.9 Applied instantaneous load versus elongation for Q125 carbon steel exposed to 50% CO_2-saturated brine at various total pressures

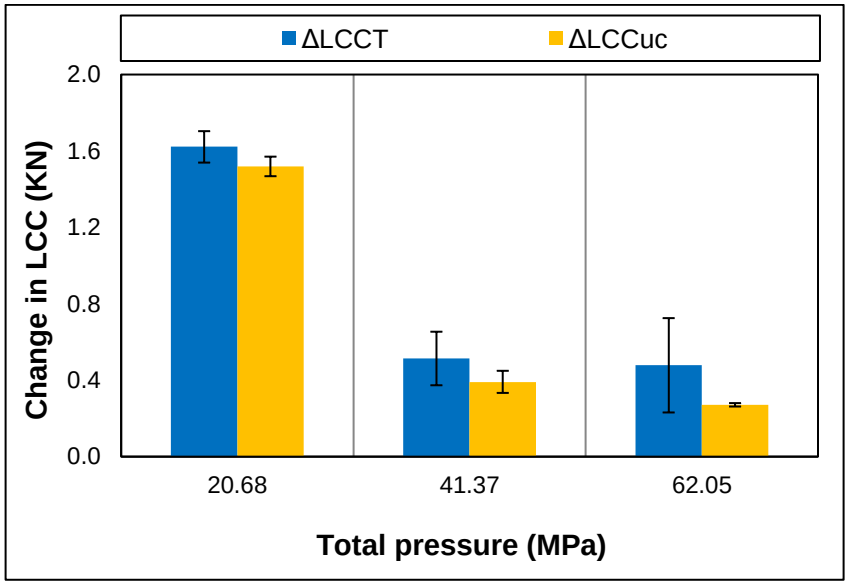

Fig. B.10 ΔLCCT and ΔLCCuc of Q125 carbon steel exposed to 50% CO_2-saturated brine at various total pressures, and 38°C